Stellar Streams as Probes of the Large-Scale Distribution of Matter around Galaxies

A Thesis presented to

Observatoire Astronomique de Strasbourg,

Université de Strasbourg

In Partial Fulfillment of the Requirements for the Degree

Doctor of Philosophy

by

Anjali Doney Varghese

Dr. Rodrigo Ibata, Thesis Supervisor

October 2011

Members of the Jury

Dr. Pierre-Alain Duc

Dr. Mathias Schultheis

Prof. Christian Boily

Dr. Hervé Wozniak (Examiner)

To Appa, Amma and Akkuttan,

for their unconditional love and great sense of humour

Acknowledgements

Some say that you have to jump off cliffs and grow wings on the way down. Though I feel like I may have developed a couple of stubs of wings over the last few years, it's my supervisor, Rodrigo Ibata, who has always been there like a parachute, keeping me from crash landing. For this, I cannot thank him enough. I am grateful to him for his constant guidance and unshakeable kindness.

I extend my sincere thanks to everyone at l'Observatoire for making me feel welcome and at home here, but I would like to especially thank: George, my doctoral comrade; Ivan, Caroline, Pierre, and Ada, who always know how to cheer someone up; Morgan and Florent, my office-mates and Unix go-to guys; Maxime, for helping me settle in; Hervé, whose firm requests helped greatly in the materialization of this thesis; and also Ariane, Mark, Christian, Laurence, Thomas (Boch et Keller), Sandrine, Francois-Xavier, Benoit, Arnaud, Sebastien, Musthafa, Dominique, Emmanuelle, Olivier and Mireille.

Special thank yous go out to HongSheng Zhao and Geraint Lewis, for all their timely (and crucial) help and discussions. Besides them, others who have helped shaped the work gone into this thesis are Walter Dehnen, Jorge Peñarrubia, Benoit Famaey, Musthafa Mouhcine, Peter Teuben and several members of the PAndAS survey, all of whom I am indebted to for their contributions and feedback.

I would also like to thank a few dear friends of mine who have made the years in Strasbourg wonderful and helped me stay sane in less wonderful times: Katia, Xavier, Sila, Octo, Atul, Goetz.

The warmth and support of true friends stretch across oceans and continents. The list is long but here goes: Nimmi, Manka, Abhilash, Harish, Bijith, Geetha, Ran-

Summary

Over the last century, numerous studies in Astronomy and Cosmology have led to the conclusion that about seventy-five percent of the matter content and about twenty-three percent of the energy density of the Universe comes from a mysterious form of matter termed dark matter. We have not yet directly detected or produced it in the laboratory and its properties are not well understood, although there are certain criteria that it should fulfil to account for the observations. For example, it does not seem to interact with light or matter in any way other than gravitationally, or perhaps via weak interactions. However, there are several open questions about the nature of this strange component of the Universe that may yet be constrained with observations. The shapes of dark matter halos around galaxies, for instance, hold important clues to the underlying nature of its constituent particles and have been an active subject of research for a few decades. Although various approaches and techniques have been employed in order to arrive at consistent estimates of the profiles of dark matter halos around galaxies, and especially that of our own Milky Way, it has proven to be difficult to do so, partly due to observational limitations and partly due to systematic differences in the methodologies themselves.

In recent years, thanks to increasingly sensitive instruments and improved data reduction methods, it has been possible to discern interesting stellar features in the dark halos of galaxies. These structures are thought to be the remnants of galaxy mergers and have emerged as a useful tool to study dark halos at galactic scales. Prominent among these are thin, long features known aptly as stellar streams, or tidal streams as they are formed due to the tidal disruption of small satellite galaxies by the gravitational field of their large host galaxies. Since a tidal stream closely

follows the orbit of its progenitor, it can be used effectively as a tracer of the halo density profile, probing it along the equatorial as well as vertical axes. Earlier work based on tidal streams has been mostly confined to the Milky Way, using the streams observed in our Galactic halo such as the Sagittarius, Monoceros, GD1 and Palomar 5 streams. Based on characteristics of the Sagittarius stream alone, the halo of the Milky Way was at first thought to be spherical (Ibata et al. 2001b; Majewski et al. 2003) or not necessarily constrainable (Mayer et al. 2002, Helmi 2004, Martínez-Delgado et al 2002) and most recently Law & Majewski (2010) have found that a mildly triaxial halo works best.

In this thesis, I extend the modelling efforts with a significant improvement in methodology. In all of the previous work, the approach has been either to treat the streams as exact orbits and find a best fitting orbit for the stream or to run simulations that reproduce the observed stream to a certain degree. Both of these approaches pose problems in that the former is slightly erroneous in its assumption, as stellar streams, in fact, deviate from exact orbits, and the latter is computationally costly, making it impossible to conduct a thorough parameter search. One of the novel aspects of the work included in this thesis is the combination of the best of the two methods. We have developed a simple way to calculate the deviations of the stream from the orbit of the progenitor so that the stream can be obtained quickly without any N-body integrations, which makes it feasible to sample millions of possible progenitor orbits or streams within a reasonable time frame. These trial streams are used to fit the observed stream, and the fitting routine is based on Bayesian sampling, another differing aspect of our approach. Using these modifications in methodology, we examine how effectively the dark matter distribution of galaxies can be constrained, the quality and quantity of information needed to do so and specifically, whether it is at all possible to estimate the profiles of dark halos of external galaxies with only the projected coordinates of their stellar streams. The initial chapters of the thesis are dedicated to a brief review of studies of dark matter and a detailed description of the formation of tidal streams.

The main goal of the fitting algorithm developed is to be able to sample a multi-

dimensional parameter space with minimum computational time and find the values of the parameters of a halo model that yield the maximum likelihood for a given (pseudo) data set. The precise algorithm that is used is known as Parallel Tempering, wherein a few Markov Chain Monte Carlo (MCMC) chains are used simultaneously to sample the parameter space and find the global maximum of the likelihood surface. Initial tests done with pure orbits in a simple logarithmic halo model show that parameters can be easily constrained using the code. The fitting algorithm is also tested with orbits integrated in a more realistic galactic potential (with a bulge, disk components, and a spheroidal halo), the accelerations from the density distributions being calculated using multipole expansion as in Dehnen & Binney (1998). These tests demonstrate that with an orbit of sufficient length (with two or more turning points), it is possible to constrain the flattening of the halo even with only the 2-dimensional projected positions of the orbit.

In order to do a similar kind of sampling for stellar streams instead of exact orbits, a mechanism is required to convert the orbit of the progenitor to the tidal stream that it would yield in a given potential, without resorting to N-body simulations. We found that for progenitor masses less than $10^9 \, \mathrm{M_\odot}$, for which dynamical friction can be ignored, it can be achieved fairly easily. The correction mechanism is based on the fact that the stars which make up the leading and trailing arms of the stream escaped from the outskirts of the progenitor at earlier times and followed slightly different orbits in the potential. The correction mechanism has been found to work consistently well for all the streams we have tested. With this mechanism in place, we show by fitting pseudo test streams, the different parameters that can be estimated for the various kinds of data available. As expected, it is not possible to constrain the circular velocity or mass of a galactic model without kinematic data (radial velocities), but for several nearby systems, the rotational velocity curves are available or readily measurable. The encouraging result we obtain is that for sufficiently long streams, as seen in the case of pure orbits, we are able to estimate the flattening of the dark matter halo with only the positions of the stream on the sky. This enables us to constrain the profiles of external galaxies for which kinematic data are not obtained. It is to be

noted that we assumed the galaxies to be viewed edge-on, but small inclinations can be corrected for in the fitting procedure and do not affect the quality of estimation.

Recent observations by Martínez-Delgado et al. (2008) reveal long, multiply-wrapped stellar structures around the edge-on, spiral galaxy NGC 5907 which provide an excellent system to apply the above method on. The data used for fitting are the rotation curve (for up to 30 kpc) of the galaxy, and the geometry of the stream on the sky. The position of the progenitor is unknown and the exact path of the stream is unclear as there are a few crossing arcs. Assuming the progenitor to be completely disrupted and the age of the stream to be a free parameter, we find the best fitting stream with the technique developed. In order to ensure convergence, we also fit the streams with a modified algorithm known as affine sampling, which uses many groups of parallel MCMCs. The preliminary tests show that the stream can be fit well in a highly prolate halo as well as a triaxial halo. The conclusive parameter values and their errors are yet to be estimated. The prospects for further development of the technique and its application to other data are discussed.

Résumé

Au cours du siècle dernier, des études en astronomie et en cosmologie ont conduit à la conclusion qu'environ 75% de la matière et environ 23% de la densité d'énergie de l'Univers vient d'une forme mystérieuse de matière appelée matière noire. Nous ne l'avons pas encore directement détectée ou produit et ses propriétés ne sont pas bien comprises, mais il y a certains critères qu'elle doit remplir pour être compatible avec les observations. Par exemple, elle ne semble pas interagir avec la lumière ou la matière de toute autre manière que gravitationnellement, ou eventuellement via des interactions faibles. Il y a plusieurs questions ouvertes sur la nature de cette composante étrange de l'Univers qui peuvent être contraintes par des observations. La forme des halos de matière noire autour des galaxies, par exemple, contiennent d'importants indices sur la nature profonde de ses particules et sont un sujet de recherche actif depuis quelques dizaines d'années. De nombreuses approches et techniques ont été employées afin d'aboutir à des estimations cohérentes des profiles de halos de matière noire autour des galaxies et en particulier celui de la Voie Lactée. Cependant, c'est une tâche difficile en partie du fait des limitations observationnelles et en partie à cause des différences systématiques entre les méthodes utililsées.

Ces dernières années, grâce à des instruments plus sensibles et à l'amélioration des méthodes de réduction de données, il a été possible de discerner des structures stellaires à basse brillance de surface dans le halo des galaxies. On pense que ces structures sont le reste de fusions de galaxies et sont ainsi un outil utile pour étudier les halos à des échelles galactiques. Parmi celles-ci, il existe de longues et minces structures connues sous le nom de courant stellaire, ou de courant de marée. Elles sont formées lors de la perturbation de marée de petites galaxies satellites par le

champ gravitationnel de leur galaxie hôte. Puisque le courant de marée suit de près l'orbite de son progéniteur, on peut l'utiliser efficacement comme traceur du profil de densité du halo, et le sonder le long des axes équatiorial et vertical. Les travaux antérieurs basés sur les courants de marée ont été principalement confinés à la Voie Lactée. Ils utilisaient les courants observés dans notre halo Galactique comme celui de la galaxie naine du Sagittaire, celui du Monoceros, GD1 et de l'amas globulaire Palomar 5. A partir des caractéristiques du courant du Sagittaire uniquement, le halo de la Voie Lactée était d'abord considéré sphérique (Ibata et al. 2001b; Majewski et al. 2003) et n'était pas bien contraint (Mayer et al 2002, Helmi 2004, Martínez-Delgado et al 2002). Récemment Law & Majewski (2010) ont trouvé que un halo légèrement triaxial est ce qui fonctionne le mieux.

Dans cette thèse, je poursuis les efforts de modélisation avec une amélioration significative de la méthodologie. Dans tous les travaux précédents, l'approche a été soit de considérer les courants comme des orbites exactes et de les ajuster, soit d'effectuer des simulations qui reproduisent approximativement ces courants. Ces deux approches posent des problèmes. La première est baseée sur une hypothèse erronée, car en réalité les courants stellaires s'écartent des orbites exactes. Le deuxième approche est coûteuse en ressources informatiques ce qui rend impossible une recherche exhaustive dans l'espace des paramètres. Un des nouveaux aspects des travaux inclus dans cette thèse est la combinaison du meilleur des deux méthodes. Nous avons développé une méthode simple pour calculer rapidement un courant à partir de l'orbite de son progéniteur sans avoir à faire d'intégration N-corps. On peut donc échantilloner des millions d'orbites progénitrices ou de courants possible dans un laps de temps raisonnable. Une autre particularité de notre approche réside dans le fait que la routine d'ajustement est basée sur une méthode Bayésienne. Grâce à ces modifications dans la méthodologie, nous examinons la qualité des contraintes sur la distribution de matière noire des galaxies, le type et la quantité de données nécessaires pour le faire et, en particulier, si il est possible ou pas d'estimer les profils de halos de galaxies externes avec seulement les coordonnées projetées de leurs courants stellaires.

L'objectif principal de l'algorithme d'ajustement développé est d'être capable

d'échantillonner un espace paramétrique multi-dimensionnel avec des temps de calcul minimum et de trouver les valeurs des paramètres d'un modèle de halo qui rapportent le maximum de vraisemblance pour un ensemble de données. L'algorithme précis qui est utilisé est connu sous le nom de 'Parallel Tempering', qui utilise des chaines de Markov (Markov Chain Monte Carlo, MCMC) simultanément pour échantilloner l'espace des paramètres et trouver le maximum global de la surface de vraisemblance. Les premiers tests faits avec des orbites pures dans un modèle de halo logarithmique simple montrent que les paramètres peuvent être facilement contraints en utilisant le code. L'algorithme d'ajustement est également testé avec des orbites intégrées dans un potentiel galactique plus réaliste (avec un renflement, des composants du disque, et un halo sphéroïdal). Pour ce potentiel, les accélérations sont calculées à partir des distributions de densité en utilisant l'expansion multipolaire de Dehnen & Binney (1998). Ces tests démontrent que, pour une orbite de longueur suffisante (avec deux ou plusieurs points d'inflexion), il est possible de contraindre l'aplatissement du halo, même en connaissant uniquement des positions 2-D de l'orbite prévue.

Afin de faire un échantillonage similaire pour les courants stellaires à la place d'orbites exactes, nous avons besoin d'un mécanisme pour obtenir le courant à partir de l'orbite du progéniteur sans recourir aux simulations N-corps. Nous avons constaté que pour des masses du progéniteur inferieur à $10^9 \, M_\odot$, pour laquelle la friction dynamique peut être ignorée, le conversion est obtenu assez facilement. Le mécanisme de correction est basé sur le fait que les étoiles qui composent les deux bras du courant de marée suivent des orbites différentes dans le potentiel. Nous avons trouvé que le mécanisme de correction fonctionne correctement pour tous les courants que nous avons testés. Avec ce mécanisme en place, en ajustant des pseudo courants de test, nous vérifions les différents paramètres qui peuvent être estimés pour les différents types de données disponibles. Comme prévu, il n'est pas possible de contraindre la vitesse circulaire ou la masse d'un modèle galactique sans données cinématiques (vitesses radiales), mais pour plusieurs systèmes proches, les courbes de rotation sont de toutes façons disponibles ou facilement mesurables. Le résultat encourageant que nous obtenons est que, pour des courants suffisamment longs, nous sommes en mesure

d'estimer l'aplatissement du halo de matière noire avec seulement les positions des courants sur le ciel. Cela nous permet de contraindre les profils des galaxies extérieures pour lesquels des données cinématiques ne sont pas obtenues. Il est à noter que nous avons supposé que les galaxies sont vues par la tranche, mais de petites inclinaisons peuvent être corrigées dans la procédure d'ajustement et n'affectent pas la qualité de l'estimation.

Des observations récentes par Martínez-Delgado et al. (2008) révèlent des structures stellaires multiplement enroulées et longues autour de la galaxie spirale NGC 5907. Ceci fournit un excellent système pour appliquer la méthode ci-dessus. Les données utilisées pour l'ajustement sont la courbe de rotation de la galaxie, et la géométrie du courant sur le ciel. La position du progéniteur est inconnue et le chemin exact du courant n'est pas clair car il ya un peu d'arcs de croisement. En supposant que le progéniteur est complètement détruit et en prenant l'âge du courant comme paramètre libre, on trouve le courant correspondant au meilleur ajustement avec la technique développée. Afin d'assurer la convergence, nous avons également ajusté les courants avec un algorithme modifié connu sous le nom d''échantillonnage affine', qui utilise de nombreux groupes de MCMCs parallèles. Les tests préliminaires montrent que le courant peut être bien ajusté dans un halo très allongé ainsi que dans un halo triaxial. Les valeurs des paramètres concluants et leurs erreurs ne sont pas encore estimés. La méthode présentée ici a donné des résultats préliminaires intéressants sur le galaxy. Son utilisation dans un cadre plus général est en cours et discuté dans la dernière partie de cette thèse.

List of Publications

− *Stellar streams as probes of dark halo mass and morphology: a Bayesian reconstruction*

Vagrhese A., Ibata R., Lewis G.F., 2011, MNRAS, sous presse (arXiv: 1106.1765)

− *The Northern Wraps of the Sagittarius Stream as Traced by Red Clump Stars: Distances, Instrinsic Widths and Stellar Densities*

Correnti M., Bellazzini M., Ibata R. A., Ferraro F.R., Varghese A., 2010, ApJ, 721, 329C

− *Density and Kinematic Cusps in M54 at the Heart of the Sagittarius Dwarf Galaxy: Evidence for a $10^4 M_{sun}$ Black Hole*

Ibata R., Bellazzini M., Chapman S. C., Dalessandro E., Ferraro F., Irwin M., Lanzoni B., Lewis G. F., Mackey A.D., Miocchi P., Varghese A., 2009, ApJ, 699L.1691

Contents

List of Tables

List of Figures

Chapter 1

Introduction

A few centuries since the dawn of scientific thinking, we find ourselves in the midst of an era contemplating questions about the Universe that are beyond our senses and perhaps even our imagination. Equipped with unprecedented technology and knowledge, we seek these challenging answers. One such set of questions concerns an elusive component of the Universe, whose presence has been betrayed by observations of the night sky as well as of the tiniest particles that we are made of. Dark matter, as it has come to be called, is now an integral part of the current understanding of the physical world, even though its exact nature remains a mystery. In this thesis, we develop a method that may be used to answer a particular question about its property: How is dark matter distributed at the galactic scale?

Our tool of investigation is stellar streams, observed in the halos of spiral galaxies, and which are remnants of the accretion process that builds up these halos. In Chapter 2, we present the various aspects of the formation of stellar streams during minor mergers. Chapter 3 contains the backbone of the thesis, the methodology developed to constrain the shape and mass of dark matter halos with these stellar streams. In Chapter 4, some preliminary results obtained by using the method on the stellar stream of NGC 5907 are discussed. We end with general conclusions and several possible extensions of the work in Chapter 5. In this introductory chapter, we present a general overview of dark matter. §1.1 contains a brief discussion on the developments in astronomy, cosmology, and particle physics that has given dark

matter its current status as a crucial component of models of the Universe. We touch upon a popular alternate theory of gravity in §1.2 and discuss some examples of possible dark matter candidates and their detection mechanisms in §1.3. The second half of this Chapter focuses on profiles of galactic halos, theoretical predictions from simulations and some observational estimates of the same.

1.1 Early Evidence of Dark Matter

The beginnings of a paradigm shift in the fundamental idea of the composition of the Universe surfaced about a century ago when astronomers began to notice a stark discrepancy in the amount of luminous matter and dynamically inferred matter in the Universe. Zwicky (1933) measured radial velocities of galaxies in the Coma cluster. Subtracting the mean velocity of the cluster from these, he found that the individual galaxies were orbiting within the system with velocities much greater than were expected given the total mass of the cluster. He hypothesized the presence of unseen matter, which he called *dunkle materie*, to account for the observed speeds. Similar analyses of the radial velocities of galaxies in the Virgo cluster by Smith (1936) and Zwicky (1937) revealed that it too contained a substantial amount of *dunkle materie*. These results spurred on a string of dynamical studies of pairs and groups of galaxies, with new techniques developed along the way, and they all pointed to the presence of some kind of unseen matter. For instance, based on timing arguments of the motion of Andromeda (M31) and the Milky Way, Kahn and Woltjer (1959) concluded that there was a deficit in the luminous mass of about $1.3 \times 10^{12} \, M_\odot$ in the Local Group.

The evidence for unaccounted-for-matter from other areas of astronomy also started to mount. In fact, eleven years prior to Zwicky's study of the Coma cluster, Jeans (1922) and Kapteyn (1922) had found that the observed density of stars near the Galactic plane was insufficient to maintain their high-velocity vertical motions. Another astounding piece of evidence for dark matter came in the form of the rotational curve of M31 in the optical (Babcock, 1939; Rubin and Ford, 1970) and radio bands (van de Hulst et al., 1957; Roberts and Whitehurst, 1975). The spectra these authors

obtained showed that the orbital velocities of stars in the outer parts of the galaxy did not decrease with radius, as was expected in a Keplerian potential. Instead, the orbital velocities stayed more or less constant at radii of $16 - 30$ kpc from the nucleus of M31, which could be explained by assuming that its galactic disk is surrounded by a halo of unseen matter. Rotation curves of other galaxies were also found to show the same trend (Thonnard et al., 1978; Bosma, 1978; Rubin et al., 1980).

Developments in X-ray astronomy provided a powerful direct tracer of mass distribution at large scales. Hot gas was observed to extend far beyond the disks of galaxies, and in between galaxies in clusters. The motion and temperature of the hot gas, which can be inferred from its X-ray emissions, are related to the gravitational potential it resides in (Forman and Jones, 1982; Rosati et al., 2002). Mass determination of the Coma and Virgo clusters from its X-ray emissions yielded values that agreed with the earlier obtained estimates (Bahcall and Sarazin, 1977), and confirmed the missing matter problem.

1.1.1 Cosmological Considerations

There are a few cosmological conundrums which are easily solved by introducing a large dark matter component to the matter content of the Universe. For instance, there is the problem posed by the abundances of light elements, such as deuterium, helium and lithium, created during big bang nucleosynthesis. Nucleosynthesis is the epoch in the early Universe when its temperature dropped low enough so that photons did not have the required energy to break apart nuclei of light elements $(D, {}^3He, {}^4He, {}^7Li)$ that formed by the collision of protons and neutrons. With further expansion and decrease in temperature, the collisions between neutrons and protons become fewer and finally marked the end of nucleosynthesis. The exact amount of light elements formed depends upon the density of baryons during the short nucleosynthesis phase. The estimates of the relic light elements from present day observation, therefore, place tight constraints on the baryon density of the Universe. Based on this approach, the estimated values of the baryon density is about 0.04 times the critical density (Schramm and Turner, 1998; Steigman, 2010), whereas the total mass density
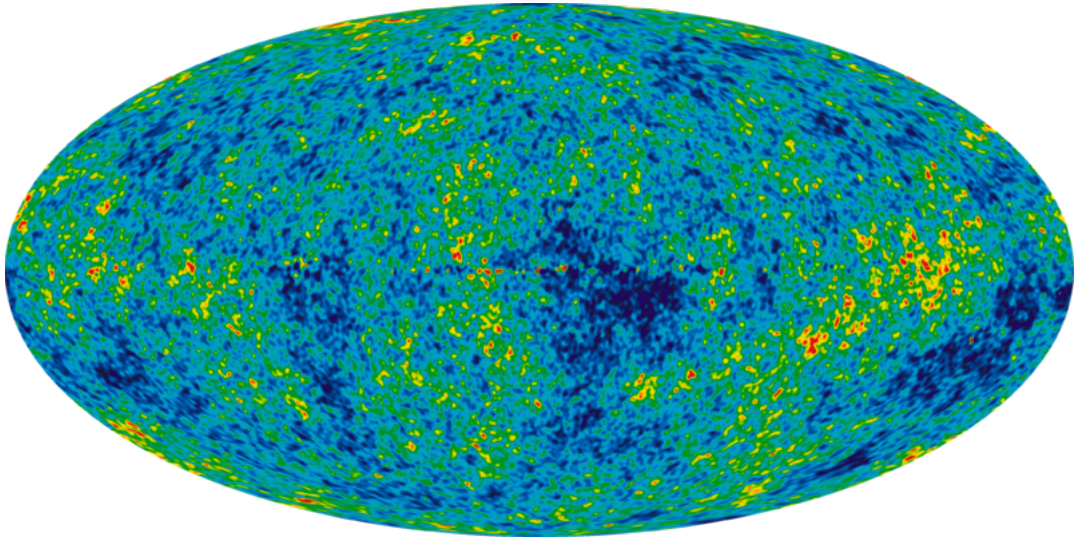
Figure 1.1: WMAP image of the Cosmic Microwave Background. The colours correspond to the fluctuations in temperature, which are in turn related to the initial density fluctuations that grow by gravitational collapse to the present day large-scale structures. Source: NASA/ WMAP Science Team.

of the Universe is at least 0.3 times the critical density. Another significant event in Cosmology was the discovery of the Cosmic Microwave Background (CMB), which maps the last surface of scattering of photons at the time of the transition of the early Universe from an opaque plasma to a transparent neutral gas. The quantum fluctuations in density could then grow and form structures by gravitational collapse. The initial density fluctuations can be calculated from the temperature anisotropies in the CMB (White, 1999); a modern map of these anisotropies is shown in Figure 1.1 as obtained by the Wilkinson Microwave Anisotropy Probe (WMAP). The fluctuation amplitude turns out to be extremely insufficient to trigger structure formation early enough, in order to produce the large-scale structures that are seen today. However, a large dark matter component could provide the required mass needed to set off structure formation at the right time.

1.1.2 Motivations from Particle Physics

In parallel to all these developments in Astronomy and Cosmology, a lot of exciting progress was being made at the other end of the (spatial) scale spectrum. Towards the end of the 19th Century, Becquerel (1896) discovered the curious phenomenon of radioactivity. A particular kind of radioactivity, known as beta-decay, could not be explained by the then known strong and electromagnetic forces. An extremely short-range force, known as the weak force, was proposed to explain the phenomenon. The first model of the weak force was put forward by Fermi in 1933, and by 1970, it was modified and unified with electromagnetism, by Glashow, Salam and Weinberg, as the electroweak theory (Glashow, 1961; Weinberg, 1967; Salam, 1968). Advances in high energy experiments confirmed the predictions of the theory. The neutrino, which only interacts via the weak force and which was postulated by Pauli in 1930 to conserve energy and momentum in the observed beta-decays, was finally detected by Reines and Cowan (1953) using liquid scintillation detectors (Cowan et al., 1953). The W and Z bosons, the carriers of the weak force, were also produced and detected, by Rubbia and van der Meer (Rubbia, 1985; van der Meer, 1981) at the Super Proton Synchrotron. When it became clear that brown dwarfs and other non-luminous baryonic matter was insufficient to account for the missing matter in astronomical problems, these advents in particle physics suggested that dark matter may indeed be particles that interact only via weak interactions and gravitation, much like the neutrino. In fact, an extension of the standard model of particle physics, known as supersymmetry, postulates entire families of as-yet-undetected particles, such as the neutralino, which are excellent dark matter candidates. These are collectively known as Weakly Interacting Massive Particles or WIMPs. Using the production energy and annihilation rates predicted for WIMPs, one may calculate the frozen-in quantity of WIMPs during the earliest epochs of the formation of the Universe. The estimated value turns out to be in the same ballpark as the value inferred from cosmological considerations. This matching up of the estimated values of the WIMP number density using a particle physics as well as a cosmological approach, known as the WIMP coincidence, lends further support to the notion that the deviant dynamical behaviour

(from the expected Newtonian) of stars and galaxies can be attributed to dark matter which consists of these WIMPs.

1.2 Modified Newtonian Dynamics

Despite several compelling pieces of evidence that the rotational curves of galaxies and the peculiar motions of galaxies in clusters can be simply justified with dark matter, there remains a very real possibility that these observations hint at a departure of the underlying gravitational law from the standard Newtonian or Einsteinian, rather than the mere presence of hypothetical, invisible matter. One of the main reasons for investigating this alternative, besides its physical feasibility and elegance, is that no convincing dark matter particle has yet been detected or produced, even after years of experiments to do so. Before we delve into a discussion of dark matter, it would be fitting to discuss one of the more popular of these alternative gravity theories known as MOdified Newtonian Dynamics, or MOND. Most tests and probes of dark matter distribution at the galactic and cluster scales try to verify MONDian predictions as well. Stellar streams that we use in this thesis may also be used to test it at galactic scales, as we demonstrate in Chapter 4.

MOND was originally put forward by Milgrom (1983a,b) to explain the asymptotically flat rotational curves of galaxies, by proposing a modification of Newtonian gravity at very small acceleration regimes. In particular, the usual force law, $F = ma$, is replaced by:

$$F = m\mu \left(\frac{a}{a_0} \right) a \tag{1.1}$$

where a_0 is a constant which determines the acceleration scale at which the modification becomes significant, and μ is a function of the relative acceleration a/a_0, known as the interpolating function. Its exact form depends on the specific flavour of the theory used. In general, $\mu(a/a_0) \sim 1$ when $a \gg a_0$ and reduces to the standard Newtonian law, and $\mu(a/a_0) \sim a/a_0$ when $a \ll a_0$. This ensures that the velocities of stars at larger radii, with increasingly smaller accelerations, are much larger than in the Newtonian case.

A consequence of this modification is that it renders the corresponding Poissonian non-linear:

$$\nabla \cdot \left[\mu \left(\frac{||\nabla \Phi||}{a_0} \right) \nabla \Phi \right] = 4\pi G \rho \tag{1.2}$$

from which a simple expression for the gravitational acceleration in a MONDian regime, $\vec{g}_M$, in terms of the Newtonian gravitational acceleration, $\vec{g}_N$, may be derived as:

$$\vec{g}_M = \vec{g}_N \sqrt{\frac{a_0}{||\vec{g}_N||}}. \tag{1.3}$$

A covariant generalization of MOND known as Tensor-Vector-Scalar (TeVeS) theory was developed by Bekenstein (2004), which allows gravitational lensing predictions for modified gravitational theories.

Despite the success of MOND at galactic scales, it faces difficulties in explaining phenomena at larger scales. One of the observational evidences against MOND that gained a lot of notoriety was the X-ray observations and lensing studies of the Bullet Cluster 1E 0657-558 (Clowe et al., 2004, 2006). It consists of a collision of a small cluster with a larger cluster, during which the gas has been stripped due to ram-pressure. It was shown that the gravitating matter distribution, determined by weak lensing, is well separated from the X-ray gas which makes up most of the baryonic matter. Since the potential in a modified gravity theory should follow the baryonic mass, the distinction of the gravitational and baryonic matter distributions violates the expectations of MOND. Some efforts have been made to resolve this issue, such as by coupling MOND with some form of missing matter such as massive neutrinos (Famaey et al., 2008), or by reproducing lensing signals similar to the one seen in the Bullet Cluster using lensing in a multifield TeVeS framework (Angus et al., 2006). Therefore, despite the challenges to MOND at cluster and super-cluster scales, its validity still remains debated and its important to continue to verify it with gravitational potential tracers.

1.3   Dark Matter Candidates

Assuming that Newtonian gravity holds at non-relativistic speeds and that what causes the anomalies in the dynamics of stars, galaxies and clusters is indeed a form of matter unknown to us, we briefly discuss what this dark matter could be made of, in the light of current research in particle physics. The aim of the section is to highlight the diverse possibilities of exotic matter that may exist, and which makes the hunt for dark matter particles extremely difficult.

The leading DM candidate is the lightest neutralino χ_1 (Ellis et al., 1984), a typical WIMP. It is the lightest of the supersymmetric particles, electrically neutral and stable. They are the superpartners of neutral Higgs and gauge bosons. As explained in §1.1.2, it turns out to have the correct relic density at thermal freeze-out. They may be detected by scattering in sensitive detectors below the Earth's surface. They may also be detected indirectly from $\chi_1\chi_1$ annihilation in the galactic halo which produces positrons (Feng, 2004).

Another possible candidate arises when one considers theories of extra dimensions. In models of universal extra dimensions (UED), there are counterparts to the standard model particles known as Kaluza-Klein particles, the lightest of which is stable due to a type of parity conservation and could be a WIMP (Feng et al., 2003a). There are several such WIMP particles predicted by various flavours of electroweak theories, but they are all similar in nature in that they are cold, collisionless and weakly interacting, and therefore lead to similar cosmological and astronomical observations. However, their differences become important when considering their detection or production in laboratories.

Yet another group of hypothetical particles, known as superWIMPs, could account for all or some dark matter (Feng et al., 2003c,b). They are named so for they interact mainly through gravity, and other interactions, if any, are much weaker than the weak force. They are thought to be formed by the decay of WIMPs after the latter thermally decouples, or by the occasional interactions of standard model particles after reheating. Once produced, their annihilation is difficult due to their extremely weak interactions. The lightest gravitino $\widetilde{G}$ is a prime example of a superWIMP. It

is a stable, spin 3/2 fermion predicted by supersymmetry, as a superpartner of the graviton. Besides the gravitino, there are many possible superWIMP particles such as the axino, the quintessino, none of which can be detected directly due to their poor interaction. SuperWIMPs, unlike WIMPs, may be warm, with large velocities. One direct observable consequence of this is that it wipes out cusps at the center of dark matter halos (see §1.5 below). However, there are other mechanisms suggested for smoothing out cusps, or it may be the consequence of other warm dark matter particles like sterile neutrinos. See Feng (2010) for a discussion of superWIMPs.

A popular cold dark matter candidate is the axion, a hypothetical boson that is created due to the spontaneous breaking of Peccei-Quinn symmetry, invoked to resolve the strong CP problem (Weinberg, 1978; Wilczek, 1978). Axions interact with gluons and fermions. Unlike WIMPs, its relic density need not necessarily match the cosmologically estimated relic density. It can convert to and from a photon in the presence of a strong magnetic field. This conversion process is used in hunting for axions. ADMX (Axion Dark Matter Experiment) looks for axions in the dark matter halo of our galaxy and CAST (CERN Axion Solar Telescope) for solar axions. There are also several ongoing efforts to create and detect axions in laboratories such as BFRT, PVLAS, BMV, LIPSS, GAMMeV, in which laser beams are passed through strong magnetic fields to produce axions, which are then separated from the photons with a filtering wall. Such laboratory experiments have hitherto been unsuccessful, though some exclusion constraints have been made. For instance, ADMX has also ruled out μeV axions (Hertzberg et al. 2008). For detailed reviews of various dark matter candidates, see (Bergström, 2009).

1.4 ΛCDM

There exists a plethora of likely dark matter candidates with different properties as illustrated in the previous section, but from a cosmological perspective, the most widely accepted general form of dark matter is of the non-relativistic variety. Known as cold dark matter, or CDM, it is an integral part of the current standard model of

cosmology, which explains the birth and evolution of the Universe and its structures. According to this model, called ΛCDM or the concordance model, the Universe consists of dark energy ($\sim 73\%$), cold dark matter ($\sim 23\%$) and baryonic matter ($\sim 5\%$). Λ denotes the dark energy, which is the energy of the vacuum that drives the acceleration of galaxies away from each other, against their mutual gravitational pull. The Universe is considered to be isotropic and homogenous at large enough scales and is thought to have been brought into existence by a singularity known as the 'Big Bang'. The model has been successful in explaining the cosmic microwave background (CMB) as well the abundances of light elements.

In the Λ-CDM framework, the early universe, immediately after the big bang, was characterized by rapid expansion and chaotic fluctuations of quantum mechanical origin. The resulting initial density perturbations grew linearly and once they gained enough mass, started to attract each other gravitationally and collapse to form larger structures. The gas that collected in the cores of heavy halos formed by this hierarchical clustering cooled and condensed to form galaxies (Searle and Zinn, 1978; White and Rees, 1978), which continue to cluster, merge and evolve. The comparison of astrophysical observations with theoretical and numerical prediction is the basis for understanding, verifying and improving cosmological models. The simulations use N-body integrations (commonly based on merging treecode among other approaches) to calculate the gravitational clustering of dark matter and also usually include processes such as star formation, radiative cooling, gas dynamics at the relevant scales. One of the successes of ΛCDM over other models is the agreement between the large scale structures seen in the simulations and those observed at the present epoch.

Seminal papers by Eggen et al. (1962) and Searle and Zinn (1978) triggered an explosion of activity in the field of galactic archaeology, which involves using stellar kinematics, metal abundances, age and distribution on the sky as clues for unravelling the formation history of galaxies (see also Freeman and Bland-Hawthorn 2002). For these purposes, the stellar and dark matter halos of a galaxy contain the maximum information as they are the most well-preserved, unlike the disk or bulge (of spiral galaxies) which undergo severe dissipation during their formation, thereby losing

many of the signatures of their early existence. However, the faint halo structures are more difficult to observe and it is only in recent years, with better telescopes and data reduction tools, that the archaeological potential of these structures have started to be tapped into. Improvements in technology also allow increasingly detailed studies of halos of galaxies other than our own. Observations of in-falling satellites, remnants of minor and major mergers such as stellar arcs, shells, streams and tails, provide strong evidence in support of a top-down scenario of structure formation, as predicted by ΛCDM models.

1.5   Profiles of Galactic Halos

The morphology of halos provides hints of their formation process and the underlying nature of dark matter. Rotation curves of galaxies are sensitive to the distribution of dark matter in the equatorial plane, but not to that in the vertical direction. It can be reproduced both in a spherical as well as a flattened density distribution that obeyed an inverse square law. For simplicity, the initial approach was to assume a truncated isothermal sphere. However, high resolution N-body simulations of dark matter halos based on cold dark matter showed that galactic halos are much better described in general by a double-power law (Navarro et al., 1996):

$$\rho(r) = \frac{\rho_0}{(r/a)(1 + r/a)^2},$$ (1.4)

where ρ_0 and a are the central density and scale radius respectively. The above form, known as the NFW profile, has a strongly cuspy center, rather than the observationally preferred core-like center. The 'core-cusp' problem has been met with more measurements of the inner dark matter profiles of galaxies, and proposed mechanisms to smooth out cusps, but it remains largely unresolved (see de Blok 2010 for a discussion). Another interesting aspect of halo profiles is its flattening. It is to be noted that the NFW profile was used to characterize the total mass of the halo at different radii, and did not take into consideration its variation with height from the disk. Since a halo forms by accretion of smaller halos around it, usually from a particular

direction, it is expected to have some angular momentum and non-sphericity. Examination of halo shapes in cosmological simulations showed this to be true, and that it was related to the exact nature of dark matter in the simulation. Earlier work on the subject by Barnes and Efstathiou (1987); Frenk et al. (1988); Warren et al. (1991); Dubinski and Carlberg (1991) found that cold dark matter halos tend to be triaxial, with a preference for prolateness, although a substantial fraction of oblate halos were seen as well. Halo shapes may be conveniently characterized by the axial ratios c/a and b/a of an ellipsoid, where a, b, and c are respectively the long, intermediate and short axes of the ellipsoid. The simulated halos studied by Dubinski and Carlberg (1991) had axial ratios of $c/a = 0.50$ and $b/a = 0.71$, although they were found to be rounder in the outer regions. In contrast, Frenk et al. (1988) found them to be more spherical in the center. Typical values in these studies of the flattening was around 0.5. These studies also concluded that the shapes of galactic halos are supported by anisotropic velocity dispersion, rather than due to rotation.

It was also seen that the morphology of galactic halos are modified by their interactions with baryons, such as accretion of dissipative gas (Dubinski, 1994). More recent studies of CDM simulations, with much higher resolution and inclusion of different baryonic processes, highlight the differences in the features of galactic halos due to baryons (Springel et al., 2004; Kazantzidis et al., 2010; Bailin and Steinmetz, 2005). For instance, baryonic cooling and star formation render the halos more spherical. Halo shapes also depend significantly on their masses, with less massive halos being more spherical (Bullock, 2002). This is likely related to the fact that low mass halos formed much earlier than higher mass halos, thereby rendering them more phase-mixed and isotropic. This may be the same reason why halos in warm dark matter or self-interacting dark matter simulations tend to be more spherical than their CDM counterparts. These recent studies also indicate that halos are not as flat as they were thought to be, with typical values of flattening at around 0.7. It has also been seen that processes such as baryonic cooling also renders their dark halos spherical.

Various techniques have been employed to probe the shape of real galactic halos, but the reach of most techniques are limited to within 30 kpc in the equatorial plane

and less then 10 kpc in the meridional plane. Only a few methods such as those based on merger remnants, satellite galaxies, weak gravitational lensing are capable of studying the matter distribution out to greater distances, especially in the vertical direction. We discuss these below.

1.5.1 Weak Gravitational Lensing

According to general relativity, the path of light behind a massive body is bent by its gravitational field due to the distortion in space-time it causes. This results in the massive body acting as a lens, producing images of the background source or distorting it in some manner. Strong lensing occurs when the observer, lens and source are lined up so that the received light is bent severely. This causes multiple images of the source usually as arcs and in rare cases, as an Einstein ring, depending on the precise geometry of the lens or lens complex. Since strong lensing requires the light from the source to pass close to the center of the lens, it only probes the potential at small scales. In weak lensing, the bending of light only produces a slight distortion, specifically a tangential shear, in the background source and no arcs or images of it are seen. The advantage is that the effects of weak lensing are present at large radii and hence, can be used to trace the potential far from the disk. Since galaxies are elliptical, the small ellipticity due to lensing cannot be measured for an individual source, but given a large number of sources, the lensing distortion due to the foreground mass can be assessed statistically (Bernstein and Jarvis, 2002). In recent years, weak lensing has been used in determining the average properties of the mass distribution of galaxies (Smith et al., 2001; Hoekstra et al., 2004; Mandelbaum et al., 2006). These studies are based on galaxy-galaxy lensing, and use large numbers of both sources and lenses, as made available by galaxy surveys. The azimuthal variation of the lensing signal is an indicator of the shape of the halo of the field galaxy. The major limitation of weak lensing studies is that they are plagued by several systematic sources of error, that have to be corrected for. Errors may arise due to complications such as inaccurate redshift values of the lenses, noise due to cosmic-rays on the CCD plates, or PSF anisotropy, to name a few. Additionally, the method relies on an

extremely large amount of data.

Using this technique, Hoekstra et al. (2004) arrived at an average value of the ellipticity $e \sim 0.33$ and of the corresponding flattening $c/a = 1 - e \sim 0.67$, in agreement with numerical predictions. The authors suggest that since MOND should yield a nearly isotropic signal, their results provide more evidence in favour of CDM over MOND. Mandelbaum et al. (2006) reported estimated values of $e \sim -1.4$ and $e \sim 0.6$, respectively for the spirals and ellipticals in their sample. The inconsistency with the estimates of the previous authors may be due to differences in the galaxy samples.

1.5.2   X-Ray Studies of Elliptical Galaxies

The continuous development of satellite telescopes, such as the ROSAT, XMM-Newton and Chandra satellites, dedicated to observing the Universe in X-ray, plays a huge role in studying the mass distribution traced by the hot X-ray emitting gases in clusters and galaxies. As discussed earlier in the chapter, it helped determine the masses of clusters, and separating the gaseous and stellar components of the Bullet cluster. At the galactic scale, they have primarily been used to constrain the profiles of the dark matter halos of isolated elliptical galaxies. These studies are based on the fact that the gas, which makes up most of the baryonic mass of the galaxies, follows the dark matter distribution and therefore, the measurement of flattening of the X-ray isophotes gives the flattening of the dark matter. The details of the inferred dark matter distribution depends on the temperature profiles of the diffuse gas, although geometric tests which show the difference in the gravitating mass and stellar component distributions to demonstrate the presence of dark matter in these galaxies can be performed independently of the gas temperature analysis (Buote and Canizares, 1998a). The main difficulties in the method are the uncertainties in the gas temperature profile and an efficient removal of point sources.

Earlier work found that the ellipticity of the dark matter halos of studied galaxies (NGC 720, NGC 1332, NGC 3923) lie in the range $e \sim 0.4-0.6$ (Buote and Canizares, 1997, 1998b). More recently, Buote et al. (2002) show that NGC 720 has a flattened,

triaxial halo of ellipticity $e \sim 0.35 - 0.4$, which supports the predictions of cold dark matter simulations. Humphrey et al. (2006) and Humphrey and Buote (2010) undertook the mass profiling of many more massive early type galaxies, which were found to fit reasonably the NFW profile as well as an adiabatically compressed NFW profile. The virial masses are found to lie in the range of $0.5 - 1.0 \times 10^{13} \, \mathrm{M_\odot}$. The center of the dark matter distribution cannot be constrained effectively with the method due to degeneracies caused by the stellar component, but they find that the less cuspy models result in larger estimated stellar mass-to-light ratios.

1.5.3 Merger Remnants

The collisions and interactions of galaxies produce distinct tails of stars and other tidal features which may be used to investigate the mass profiles of their halos (Dubinski et al., 1996; Springel and White, 1999; Dubinski et al., 1999). By numerically simulating encounters between galaxies and tuning the model parameters of the galaxies involved to produce structures similar to those observed, it is possible to get rough estimates of the halo parameters. For instance, by simulating the tidal tails of the Antennae (NGC 4038/39) and NGC 7252, Dubinski et al. (1996) find that the ratio of the halo mass to the mass of the bulge and disk are less than 10:1. Recent studies based on tidal features focus more on stellar streams formed in minor mergers of small satellite galaxies and large disk galaxies, which prove to be great tracers of the gravitational potential of the host. These low mass tidal streams are the subject of this thesis, and in the following chapters, we discuss the details of their formation, as well as a unique approach to using these streams, based on a maximum likelihood analysis, to constrain the properties of the host galaxy halo.

Chapter 2

Formation of Stellar Streams

2.1   Introduction

We as a species seem to be fascinated with objects smashing into each other, be it tiny atoms or massive galaxies. Besides the wonderful visual treats these collisions produce, they provide an opportunity to study the forces and phenomena that come into play at the scales involved. Minor mergers, in which a relatively small galaxy, such as a globular cluster or a dwarf spheroidal, falls into a much larger galaxy, usually leave behind coherent structures such as shells, arcs and long streams of stars that are now observed around several galaxies. Such kinematically cold, thin and long structures are the centerpiece of this thesis and in this chapter, the physics behind their formation is reviewed in order to understand how to use them effectively to study gravity and mass profiles at galactic scales. The two forces which influence the evolution of a satellite galaxy are the tidal forces and dynamical friction, both of which are discussed here.

2.2   Tides

Tides are the second-order effect of a gravitational field, the first being gravitational acceleration. It is essentially the difference in the gravitational pull across an extended body as a result of the difference in distance of the various points of the body from the
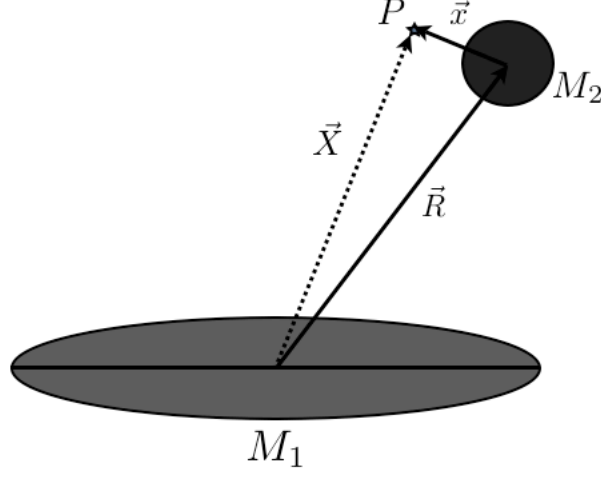
Figure 2.1: M_1 and M_2 are the host and satellite galaxies. P is a test particle or a star of the satellite, at whose position the tidal field is investigated.

center of the gravitational field. Consequently, tides are a powerful means of sensing and measuring a gravitational field from within it. At the heart of the tidal streams formation scenario is the classical restricted three body problem (Szebehely, 1967), in which the motion of a test particle (of negligible mass) under the gravitational influence of two massive bodies is studied. Consider the system shown in Figure 2.1, in which the potential at the test particle or star P due to the host galaxy M_1 and the satellite M_2 can be expanded in Taylor series as:

$$\phi(\vec{X}) = \phi(\vec{R}) + \vec{x} \cdot \left[\nabla_{\vec{R'}} \phi(\vec{R'}) \right] \Big|_{\vec{R'}=\vec{R}} + \frac{1}{2} \vec{x} \cdot \left[\vec{x} \cdot \nabla_{\vec{R'}} (\nabla_{\vec{R'}} \phi(\vec{R'})) \right] \Big|_{\vec{R'}=\vec{R}} \qquad (2.1)$$
$$+ \frac{1}{6} \vec{x} \cdot \left[\vec{x} \cdot \left[\vec{x} \cdot \nabla_{\vec{R'}} (\nabla_{\vec{R'}} (\nabla_{\vec{R'}} \phi(\vec{R'}))) \right] \right] \Big|_{\vec{R'}=\vec{R}} + \dots$$

When the force due to the potential is now calculated from this expansion as $-\nabla \phi(\vec{X})$, the first term which is a constant vanishes. The second term contributes to the gravitational acceleration. The third term is the matrix of the second order partial derivatives of the potential, also known as its Hessian. This third term gives rise to

the tidal force, that is, the variation of the gravitational acceleration, at the point of interest. For a Keplerian case, where $\phi(X) = \frac{1}{|\vec{X}|}$, the second RHS term in equation 2.1 becomes:

$$\vec{x} \cdot \left[\nabla_{\vec{R}'} \phi(\vec{R}') \right] \Big|_{\vec{R}'=\vec{R}} = \frac{\vec{x} \cdot \vec{R}}{|\vec{R}|^3} \tag{2.2}$$

and the third term becomes:

$$\frac{1}{2}\vec{x} \cdot \left[\vec{x} \cdot \nabla_{\vec{R}'}(\nabla_{\vec{R}'} \phi(\vec{R}')) \right] \Big|_{\vec{R}'=\vec{R}} = -\frac{1}{2}\frac{|\vec{x}|^2}{|\vec{R}|^3} + \frac{3}{2}\frac{(\vec{x} \cdot \vec{R})^3}{|\vec{R}|^5} \tag{2.3}$$

Adding the above two terms, we get the acceleration in a Keplerian potential:

$$g(\vec{X}) = -\frac{\hat{R}}{|\vec{R}|^2} - \left(\frac{\vec{x}}{|\vec{R}|^3} - 3\frac{(\vec{x} \cdot \hat{R})\hat{R}}{|\vec{R}|^3} \right). \tag{2.4}$$

The tidal force, given by the bracketed term, reduces to $\frac{2|\vec{x}|}{|\vec{R}|^3}$ when $\vec{x}$ is parallel to $\vec{R}$ and to $\frac{-\vec{x}}{|\vec{R}|^3}$ when $\vec{x}$ is perpendicular to $\vec{R}$. Consequently, the satellite M_2 gets tidally stretched in the radial direction and compressed in the tangential direction, with respect to the point source M_1. The amount of compression and stretching depends upon the potential form of the host galaxy M_1. The tidal field affects a satellite on a trajectory in the potential in two distinct ways. The first is by limiting the plausible size of a satellite in the potential, pruning away stars for which the gravitational acceleration towards the satellite is weaker than the tidal pull of the host. This is known as *tidal pruning* and occurs even at large distances, where the tidal field is stationary. The second and the more disruptive of the effects is *tidal shocking*, which takes place when the in-falling satellite has high speed and is close enough to the center of the galaxy where the changes in the tidal field are quite large. These conditions are usually satisfied during pericenter passages, which is when tidal forces wreak the most havoc, ejecting stars from the satellite, sometimes leading to complete disruption of the satellite. Both these effects are discussed in further detail in the following sections.
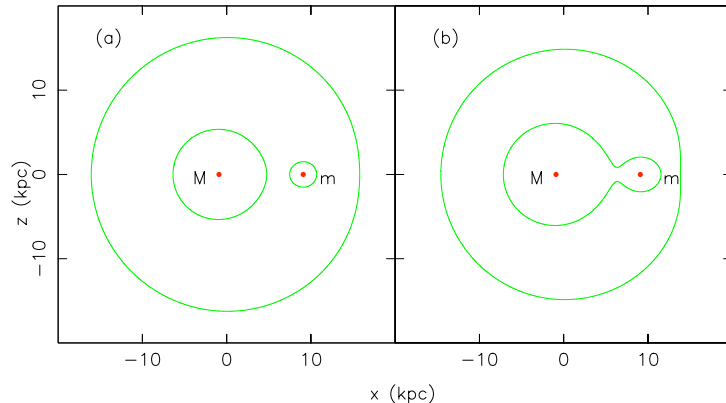
Figure 2.2: Zero velocity curves corresponding to two values of the Jacobi integral E_J. $E_j = 0.07363178$in (a) and $E_j = 0.07175149$ in (b). In (a), the zero velocity curves isolate the masses from each other and therefore, stars around m with this energy cannot escape it. In contrast, the zero velocity curve in (b) surrounds both the masses and it is therefore possible for a star orbiting m to escape through the gap to orbit M.

2.2.1   Tidal Pruning

In order to understand the motion of the stars in the outer regions of the satellite galaxy due to the tidal field, let us consider the simple case of a satellite on a circular orbit of radius $\vec{R}$ around the host galaxy. We further assume that the host and satellite are both point masses and that they rotate about their common center of mass with an angular velocity:

$$\Omega = \sqrt{\frac{G(M_1 + M_2)}{R^3}}. \tag{2.5}$$

In a reference frame centered at the center of mass of the system and rotating with the system at the same angular speed, the gravitational field Φ is stationary. If the position and velocity of a star of the satellite in this rotating frame are given by $\vec{x}$ and $\dot{\vec{x}}$, its Lagrangian is given by

$$\mathcal{L} = \frac{1}{2}|\dot{\vec{x}} + \Omega \times \vec{x}|^2 - \Phi(\vec{x}), \tag{2.6}$$
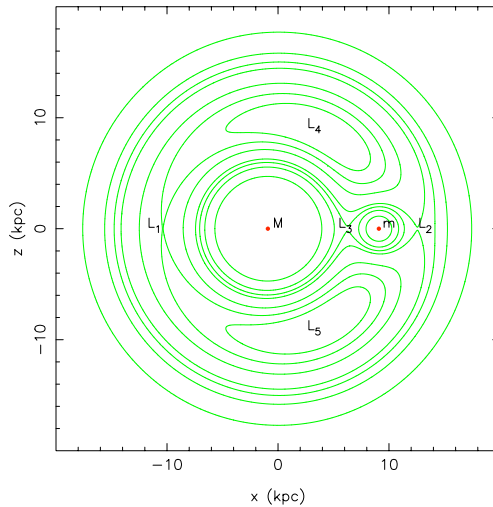
Figure 2.3: A contour plot of constant effective potential. The host M is ten times as massive as the satellite m, which is in a circular orbit around M. The Lagrange points are L_1, L_2, L_3, L_4, and L_5. The ones of particular interest to us are L_3 and L_2, through which stars of the satellite may escape.

and its momentum by

$$\vec{p} = \frac{\partial \mathcal{L}}{\partial \dot{\vec{x}}} = \dot{\vec{x}} + \Omega \times \vec{x}. \tag{2.7}$$

Therefore, the Hamiltonian of the star in the rotating frame is (Binney and Tremaine 2008 §3.3.2):

$$\begin{aligned} H_J &= \vec{p} \cdot \dot{\vec{x}} - \mathcal{L} \\ &= \frac{1}{2} p^2 + \Phi - \Omega \cdot (\vec{x} \times \vec{p}). \end{aligned} \tag{2.8}$$

The time derivative of the Hamiltonian vanishes in the rotating frame because Φ remains constant with time, which implies that it is an integral of the motion. Substituting for $\vec{p}$ from equation 2.7, we get an expression for the integral of the orbit of a star in such a system, known as the Jacobi integral:

$$E_J = \frac{1}{2} v^2 + \Phi_{eff}(\vec{x}), \tag{2.9}$$

where Φ_{eff} is the effective potential at $\vec{x}$ given by the sum of the gravitational potential due to the satellite and host and the repulsive centrifugal potential due to the rotation of the system:

$$\Phi_{eff}(\vec{x}) = \Phi(\vec{x}) - \frac{1}{2}|\Omega \times \vec{x}|^2. \tag{2.10}$$

It is to be noted that neither energy nor angular momentum of star P is conserved and E_J is the only integral of motion. Since the equations of motion have only one constant, they cannot be exactly solved. However, the Jacobi integral restricts the parts of phase-space that the stars of the satellite are allowed in. Rearranging equation 2.9, we see that for the velocity of a star in the system:

$$v^2 = 2\left[E_J - \Phi_{eff}(\vec{x})\right], \tag{2.11}$$

so that for points $\vec{x}$ for which $E_J = \Phi_{eff}(\vec{x})$, the velocity is zero. These points are the stationary points of the system, where the gravitational force is balanced by the centrifugal force and define the zero-velocity surface for stars with Jacobi integral E_J. Since regions with $E_J \leq \Phi_{eff}(\vec{x})$ have negative or zero v^2, they are forbidden to the stars and the zero-velocity surfaces demarcate these forbidden regions. Figure 2.2 shows the zero velocity curves for two different values of E_J. In the left panel, the stars of M_2 within the curve centered on it cannot escape, whereas in the right panel, they can do so and orbit M_1 instead, since the zero velocity curve surrounds both M_1 and M_2. In a series of such curves, as the one in Figure 2.3 of the contours of constant effective potential of a host-satellite system, the last curve that surrounds only the satellite M_2 defines its *Roche limit*. The distance from the center of the satellite to the Roche surface is called its Jacobi radius r_j, almost synonymous with its tidal radius, since the stars that are within the Jacobi radius remain bound to the satellite indefinitely and thus defines the extent of the satellite. The maxima and saddle points of the zero velocity surfaces make up the five Lagrange points of the system, as marked in Figure 2.3. The points that are of interest to us are L_2 and L_3, through which stars, that have sufficient energy to be outside the tidal radius of the satellite, may escape. Under the present assumptions, where M_1 and M_2 are point
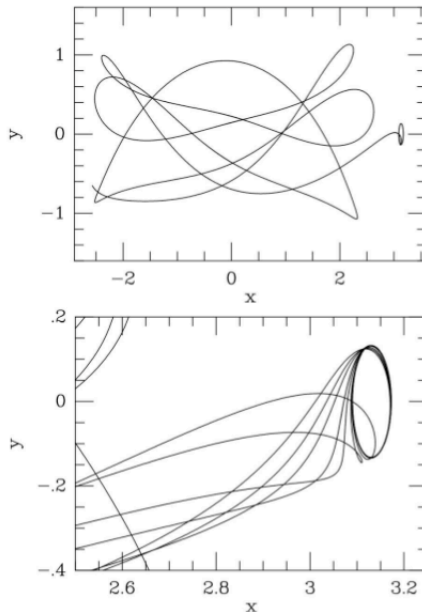
Figure 2.4: (From Fukushige and Heggie (2000)). Top panel: the orbit of a star with energy above the escape energy. The tar attempts to leave the system close to the L_2 point (located at $x \sim 3.1, y = 0$), but "bounces" off it. The bottom panel shows a close-up of this region, with several orbits of similar energy also failing to escape.

masses, with $M_2 \ll M_1$ and in a circular orbit of radius R, the Jacobi radius is given by:

$$r_J = \left(\frac{M_2}{3M_1}\right)^{1/3} R. \tag{2.12}$$

In non-circular orbits such an analytic formula for the Jacobi radius cannot be derived. However, there does exist a tidal extent for the satellite, as well as analogs of the Jacobi integral and the Lagrange points. It is often the case that the tidal radius may be approximated for practical purposes with a modification to the above expression for the Jacobi radius. For instance, if the host is of the form of an isothermal sphere, then multiplying the above formula for r_J by 1.145 yields the radius of the stationary points. We use a similar empirically found multiplicative factor in this thesis, for approximating the formation of streams.

Some of the stars of the satellite gain sufficient kinetic energy due to relaxation processes to be outside the Roche surface and get ripped out of the satellite from
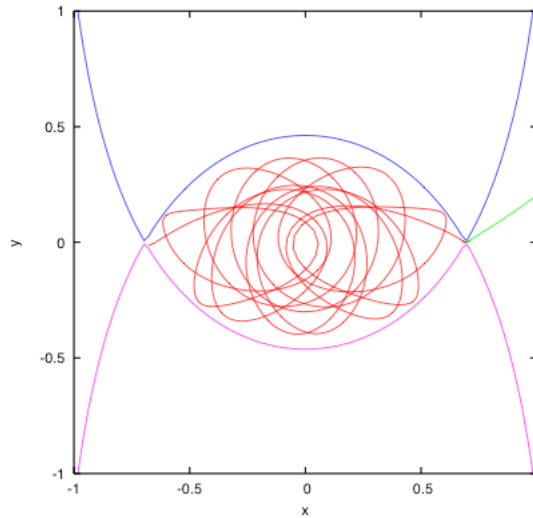
Figure 2.5: The orbit of an escaping star in a restricted three-body system with a point-mass potential for the host. After many revolutions around the satellite, the star manages to escape via the L_2 point. (Credit: Douglas Heggie).

its Lagrange or analagous stationary points. However, if these sufficiently energetic stars miss the narrow Lagrange regions, they cannot escape the system. Figure 2.4 shows orbits of such stars which pass close to the Lagrange point, but fail to escape. Figure 2.5 shows the orbit of a star which does manage to escape via the L_2 point. It has also been found that at times, despite being unbound, certain stars,continue to closely follow the satellite, because they gain the unbinding energy slowly and their orbital parameters remain similar to those of the bound stars (Ross et al., 1997; Johnston et al., 1999; Fukushige and Heggie, 2000). This effect blurs the actual tidal extent of the satellite and makes observational comparisons with simulations difficult. If we rewrite equation 2.12 in terms of the densities of the host and the satellite, it immediately follows that the average density of the satellite cannot be more than three times that of the host. In this way, the host also limits the density of the satellite.

2.2.2 Tidal Shocks

When the satellite approaches the pericenter of its orbit, the rapidly changing tidal field perturbs its stars and increases the velocities of a large number of stars drastically so that they are able to escape the satellite's gravitational field. This disruption of the satellite over the short time-period of the pericenter passage can be understood well by applying the impulse approximation and the distant-tide approximation for encounters together. In the impulse approximation, the positions of the stars are assumed to remain the same during the encounter and only the changes in their velocities are examined. Comparing with numerical simulations, Aguilar and White (1985) show that this approximation is valid even when the encounter time is long. The change in the internal kinetic energy is given by:

$$\Delta E = \frac{1}{2} \sum_{\alpha} m_{\alpha} |\Delta \vec{v}_{\alpha}|^2 \tag{2.13}$$

where m_{α} denotes the masses of the constituent stars and $\Delta \vec{v}_{\alpha}$ is the component of the change in its velocity left over after accounting for the change in the center-of-mass velocity of the satellite. The distant-tide approximation holds when the size of the satellite is much smaller than the impact parameter so that the tidal field across the satellite varies smoothly. Hence, it can be expanded as a Taylor series about the center-of-mass, just as in equation 2.1, with the third and higher order terms being neglected. The first-order term contributes to the increase in the center-of-mass velocity and the second-order terms alone contribute to $\Delta \vec{v}_{\alpha}$ in the above equation.

2.3 Dynamical Friction

Besides tidal acceleration and disruption, an important factor that affects the trajectory of a satellite galaxy is the frictional drag it experiences as it moves through the field of the host galaxy. However, as we show at the end of the section, the effect is can be neglected for the range of satellite masses in our study. Nevertheless, it

is an important ingredient in the formation of stellar streams and is essential to be included in the extensions of the method for higher mass satellites.

A physical explanation of it is as follows: consider a field of stars or point masses each of mass m_a through which a satellite galaxy of mass M moves. As it does so, the satellite attracts the field stars to itself, increasing the local density. By the time the field stars or point masses gather, the satellite moves further ahead and the increase in density behind it acts as a wake. The mass of the wake pulls the satellite backwards, decreasing its velocity, which causes the orbit of the satellite to decay over time. Energy is conserved during the process as the kinetic energy lost by the satellite is the sum total of the kinetic energy gained by the stars in the wake.

In order to characterize the strength of the frictional force, we treat the redistribution of energy and momentum between the satellite and the field stars as a diffusive process. The fluctuation in the phase-space density $f(\vec{x}, \vec{v}, t)$ of the field stars due to their encounter with the satellite, also known as the encounter operator $\Gamma[f]$, can be calculated as the difference of the influx probability and outflux probability. If $\Psi(\vec{w}, \Delta\vec{w})d^6(\Delta\vec{w})\Delta t$ is the probability of a star with phase-space coordinate $\vec{w}$ to be scattered into the volume of phase-space density $d^6(\Delta\vec{w})$ around $\vec{w} + \Delta\vec{w}$ during a time interval Δt, this gives us the net increase in phase-space density around the star to be

$$
\begin{aligned}
\frac{\partial f}{\partial t} &= \Gamma[f] \\
&= \int d^6(\Delta\vec{w})[\Psi(\vec{w} - \Delta\vec{w}, \Delta\vec{w})f(\vec{w} - \Delta\vec{w}) - \Psi(\vec{w}, \Delta\vec{w})f(\vec{w})]. \quad (2.14)
\end{aligned}
$$

The above equation is similar to the diffusion equation. For weak encounters, the change in velocity of a star is much smaller than its velocity, that is $\Delta\vec{w}$ is small and one may expand the first term of the integral as a Taylor series. Truncating it at the second-order terms and using it in equation 2.14, we arrive at the Fokker-Planck approximation

$$
\Gamma[f] = -\sum_{i=1}^{6} \frac{\partial}{\partial w_i}\{D[\Delta w_i]f(\vec{w})\} + \frac{1}{2}\sum_{i,j=1}^{6} \frac{\partial^2}{\partial w_i \partial w_j}\{D[\Delta w_i \Delta w_j]f(\vec{w})\}, \quad (2.15)
$$

where $D[\Delta w_i]$ is the first-order diffusion coefficient and quantizes the net drift of the satellite through phase-space due to the frictional force. $D[\Delta w_i \Delta w_j]$ is the second order diffusion coefficient which represents the random walk of the satellite due to the field stars. As the satellite is much more massive than the field stars, this second-order effect is negligible. Moreover, since the encounters between the satellite and field stars are local, they affect only the velocity components. Therefore, the phase-space coordinates w_i and w_j in equation 2.15 may be replaced by the corresponding velocities v_i and v_j. The first-order diffusion coefficient, which is the only contributing factor for the present scenario, reduces to the average value of the changes in velocities $D[\Delta v_i]$. If the distribution function of the field stars is isotropic, then the average velocity changes in the directions perpendicular to the motion of the satellite cancel out and the net change in velocity is solely along the direction of its motion. This decelerating force acting opposite to the direction of motion is known as dynamical friction and under the present assumptions, is given by the Chandrasekhar's dynamical friction formula (Chandrasekhar, 1943):

$$\frac{d\vec{v}_M}{dt} = -16\pi^2 G^2 M m_a \ln \Lambda \left[\int_0^{v_M} dv_a v_a^2 f\left(v_a\right) \right] \frac{\vec{v}_M}{v_M^2} \tag{2.16}$$

where $\ln \Lambda$ is the Coulomb logarithm, which for a satellite of half-radius r_h is given by

$$\ln \Lambda = \ln \left(\frac{b_{\max}}{\max(r_h, GM/v_{typ}^2)} \right) \tag{2.17}$$

and $b_{\max}$ is the maximum impact parameter. For very large velocities, equation 2.16 reduces to

$$\frac{d\vec{v}_M}{dt} = -4\pi^2 G^2 M m_a n \ln \Lambda \frac{\vec{v}_M}{v_M^3} \,. \tag{2.18}$$

This implies that at large velocities the frictional force is inversely proportional to the square of the velocity, large velocities giving less time for the wake to gather. It is to be noted, however, that at low velocities equation 2.16 reduces to the form of Stoke's law and the deceleration is proportional to the satellite velocity. For a Maxwellian
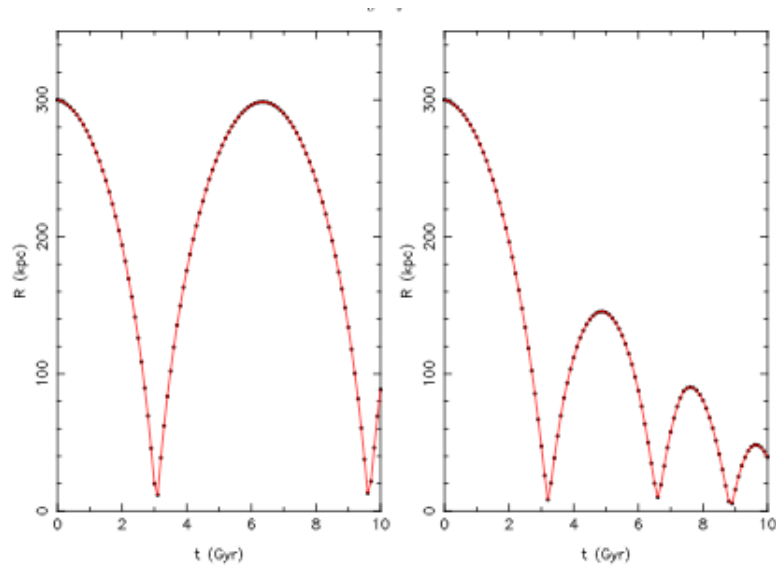
Figure 2.6: The decay of the orbit of point mass satellites. The decrease in the radius over time of satellites of mass $10^9\,\mathrm{M_\odot}$ (left hand panel) and $10^{10}\,\mathrm{M_\odot}$ (right hand panel) in a Milky Way potential are shown. The effect of dynamical friction is negligible for the lower mass satellite, but clearly significant with increasing mass.

distribution function with dispersion σ, the Chandrasekhar formula becomes

$$\frac{d\vec{v}_M}{dt} = \frac{-4\pi^2 G^2 M n m \ln \Lambda}{v_m^3} \left[\mathrm{erf}(X) - \frac{2X}{\sqrt{\pi}} e^{-X^2} \right] \vec{v}_M, \qquad (2.19)$$

where $X \equiv v_M/(\sqrt{2}\sigma)$. The above equations show that the deceleration is proportional to the mass of the satellite. The more massive the satellite, the more the bodies gathered in the wake resulting in a larger wake mass, and a proportionally larger decelerating force on the satellite. This is evident in Figure 2.6, which shows a comparison of the orbital decay of point mass satellites of masses $10^9\,\mathrm{M_\odot}$ and $10^{10}\,\mathrm{M_\odot}$, as they evolve in a Milky Way type potential. Similarly, the higher the number density of the host field the more the field stars that are gathered in the wake, increasing the frictional force.

Using the frictional force in the Lagrangian of the satellite enables us to integrate the time it takes to spiral to the center of the host galaxy. For a globular cluster or dwarf spheroidal that gets tidally stripped during the course of its trajectory, the

inspiral time from an initial circular orbit of radius r_i turns out to be (Binney and Tremaine, 2008):

$$t_{fric} = \frac{2.34}{\ln \Lambda} \frac{\sigma_{\mathcal{M}}^2}{\sigma_s^3} r_i, \tag{2.20}$$

where $\sigma_{\mathcal{M}}$ and σ_s are the velocity dispersion of the host and satellite respectively. Typical satellites in our study are globular clusters or dwarf spheroidals with masses in the range of $10^8 \, \mathrm{M_\odot}$ to $10^9 \, \mathrm{M_\odot}$ and the host galaxies are Milky Way type spirals with masses of about $10^{12} \, \mathrm{M_\odot}$. If $\sigma_s \lesssim 0.5\sigma_{\mathcal{M}}$, the Coulomb logarithm from equation 2.17 simplifies into the form $\Lambda = 2^{3/2}\sigma_{\mathcal{M}}/\sigma_s$ (Binney and Tremaine, 2008). Thus, a satellite with a velocity dispersion of $50 \, \mathrm{km \, s^{-1}}$ on an initial circular orbit of radius $30 \, \mathrm{kpc}$ around a host galaxy with velocity dispersion of $200 \, \mathrm{km \, s^{-1}}$, takes approximately $10 \, \mathrm{Gyr}$ to spiral to the center. We limit our study to such values where the effect of dynamical friction is unimportant and does not need to be taken into account to obtain the path of a tidal stream from a given progenitor orbit (see Chapter 3).

2.4   Numerical Aspects of Tidal Streams

The evolution of a satellite galaxy in the potential of a much larger host and the resulting stellar stream of a typical minor merger can be studied in great detail with the help of simulations based on N-body codes. One such simulation is shown in Figure 2.7, of the disruption of a Sagittarius-type dwarf galaxy in a realistic Milky Way potential. In this section, the basic principles behind N-body simulations and other important numerical tools which we use extensively in our study, namely orbit integration and multipole expansion, are discussed.

2.4.1   Orbit Integration

Orbit integration is a crucial component of the work included in this thesis, as it primarily revolves around fitting observed tidal streams with corrections to possible orbits of the in-falling satellite galaxy. An orbit of a particle in a given potential is computed by integrating its equations of motion forward in time, starting from an

initial set of values for of position and velocity. There are several schemes available for numerical integration, such as the Leapfrog integrator, the Runge-Kutta family of integrators, and adaptive step-size integrators. Adaptive step-size integrators and the fourth-order Runge-Kutta (RK4) provide high accuracy, and the most preferred integration scheme is the adaptive step-size for most purposes, as it adjusts the time-step to gain a required level of accuracy. Even though we used the adaptive step-size scheme in the initial phase of the project, we found that using the RK4 integrator saves much time when the sampling algorithm involves other time consuming components such as Poisson solvers, and does not result in any significant loss of accuracy.

The equation of motion $\ddot{r} = -\nabla\Phi$ can be solved by breaking it down into two first order differential equations:

$$\frac{dv}{dt} = -\nabla\Phi$$
$$\frac{dr}{dt} = v \,. \tag{2.21}$$

Putting the above equations in the general form of a first order differential equation

$$\frac{dy}{dt} = f(y, t), \tag{2.22}$$

the value of the variable y after a short time interval h is evaluated from its current value y_t as:

$$y_{t+1} = y_t + \frac{k_1}{6} + \frac{k_2}{3} + \frac{k_3}{3} + \frac{k_4}{6} + O(h^5), \tag{2.23}$$

where k_1, k_2, k_3, k_4 are given by:

$$k_1 = hf(y_t, t)$$
$$k_2 = hf\left(y_t + \frac{k_1}{2}, t + \frac{h}{2}\right)$$
$$k_3 = hf\left(y_t + \frac{k_2}{2}, t + \frac{h}{2}\right)$$
$$k_2 = hf\left(y_t + k_3, t + h\right) \tag{2.24}$$

The above prescription for updating the position and velocity of the body in motion is known as the fourth order Runge-Kutta. A detailed discussion of the scheme and other useful integrators can be found in Press et al. (1992). The equations of motion, which determine the orbit of the body, depend on the gradient of the potential in which the body moves. The potential of a matter distribution may be given directly or can be derived from the density distribution of the field. In this thesis, potential forms of both kinds are used. In order to calculate the potential or resulting acceleration at a point from an analytical density distribution, such as the double spheroidal introduced in Chapter 3, we resort to multipole expansion in spherical coordinates.

2.4.2 N-body Simulation

The stellar stream results from the motion of the satellite galaxy along an orbit in the potential of the host, which may be integrated as described in the previous section, as well as gravitational interactions between the stars of the satellite. N-body codes are concerned with such mutual interactions of a system of particles. The simulation shown in Figure 2.7 and all the others used in this thesis have been performed with "gyrfalcON", an N-body code implemented in "NEMO" (Teuben, 1995), which is similar to but much faster than standard tree-codes.

The goal of an N-body code is to alternatively calculate the acceleration individual particles experience due to the gravity of all the other particles in the system and then advance the particles by the required amount. The straightforward method of directly summing up all the forces on a given particle due to each of the other particles is time-consuming when the number of particles is of the order of 10^5 or more, but is useful in certain situations in which the number of particles is small. In the classic tree-code (Barnes and Hut, 1986), the forces on a particle due to each nearby particle is summed up directly, but the contribution to the force due to particles that lie farther away is calculated by grouping these as pseudo single particles. This is achieved by sub-dividing an imaginary cube which encloses the whole system, known as the root cube, into eight cubes of equal sides, the cubes of which contain more than one particle are further sub-divided into eight daughter cubes and so on until each cube
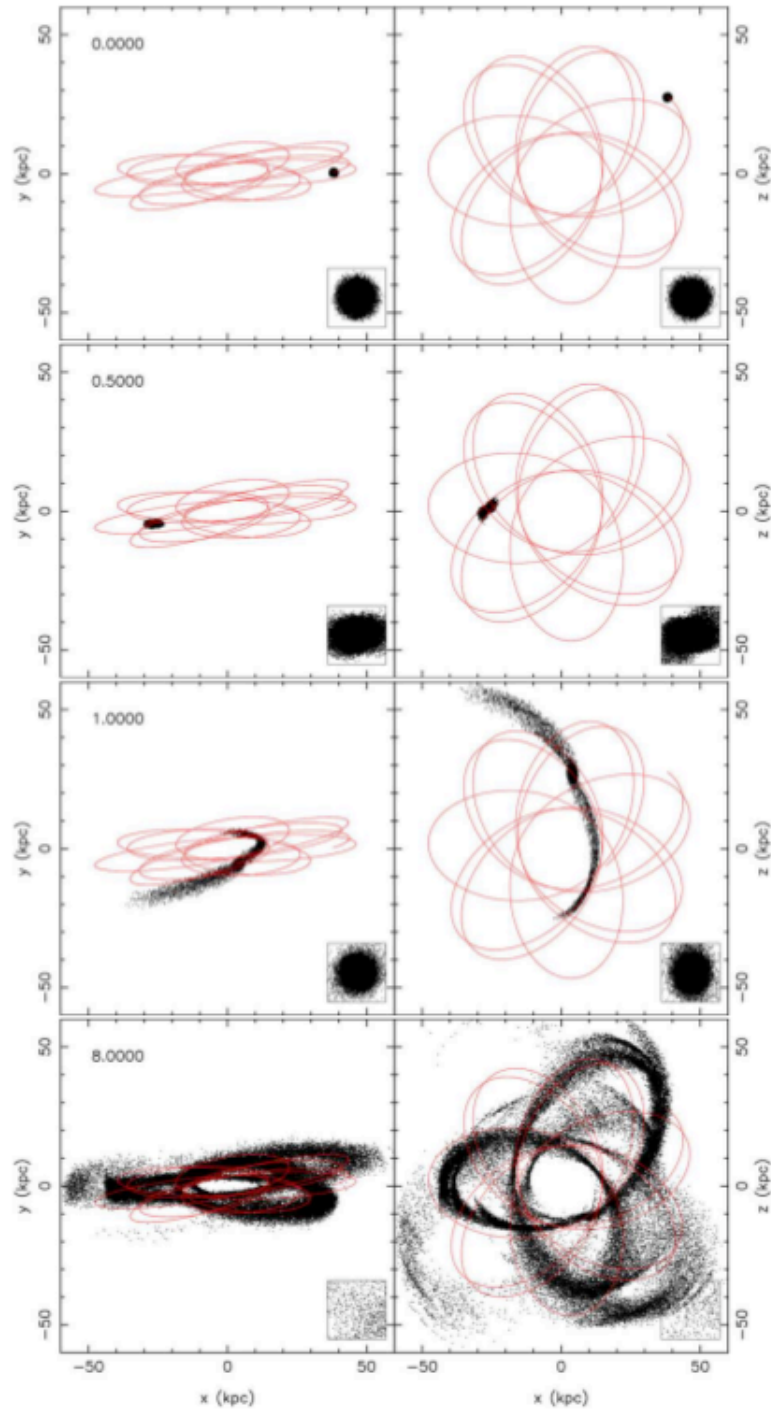
Figure 2.7: N-body simulation of the formation of a stellar stream by the disruption of a dwarf spheroidal in a Milky Way potential. The left panels and right panels show the projections of the particles of the satellites in the XY and XZ planes respectively, at times T = 0, 0.5, 1.0 and 8 Gyr from top to bottom. The insets show the core of the satellite at each stage. The N-body integrations were performed using "gyrfalcON" in NEMO.

is either empty or has only one particle. Once the tree is set up, each cell at each level is assigned its total mass and its center-of-mass, starting from the highest order individual cubes up towards the root cube. When a cube lies farther enough from the particle whose acceleration is to be calculated, it is treated as a particle with the total mass of the cube positioned at its center-of-mass. If the cell is not far enough, it is resolved into its sub-cells, each of which is either treated as a single pseudo-particle or further resolved. Whether a cell lies far enough from the given particle, or whether it needs to be resolved, depends on the ratio of the length of the cell in question (l) to the distance of the center-of-mass of the cell (d). If l/d is less than a certain prescribed value, known as the opening angle parameter θ_0 and usually set to ~ 1, then it is not further resolved and treated as a single pseudo particle. The contributions of the validated particles and pseudo-particles are summed up to yield the total acceleration $\vec{a}_\alpha$ of the particle in question:

$$\vec{a}_\alpha = \sum_{\beta \neq \alpha} GS(|\vec{r}_\beta - \vec{r}_\alpha|) \frac{\vec{r}_\beta - \vec{r}_\alpha}{|\vec{r}_\beta - \vec{r}_\alpha|}, \tag{2.25}$$

where $S(r)$ is a softening kernel introduced to avoid divergences that arise when $\vec{r}_\beta = \vec{r}_\alpha$, which asymptotically reduces the acceleration to that of a Keplerian for distances greater than the softening length ϵ and makes it zero when $\vec{r}_\beta = \vec{r}_\alpha$. The different forms of the softening lengths in practical use and their pros and cons are discussed in Dehnen (2001). Figure 2.8 shows the subdivision and hierarchical grouping of a system of particles as in the classical treecode algorithm.

The algorithm which is used to calculate the accelerations in gyrfalcON is falcON (**F**orce **Al**gorithm with **C**omplexity **O(N)**; Dehnen 2002). It is a combination of the tree-code described above with the fast multipole method (FMM), rendering it faster by a factor of ten. In falcON, the stellar system is grouped hierarchically as in the standard tree-code, but mutual interactions between between pairs of particles or pseudo-particles are calculated simultaneously, saving computational time.

From the simulation shown in Figure 2.7, we can see that during the evolution of the satellite in the potential of the host, its stars have escaped from the equivalent of
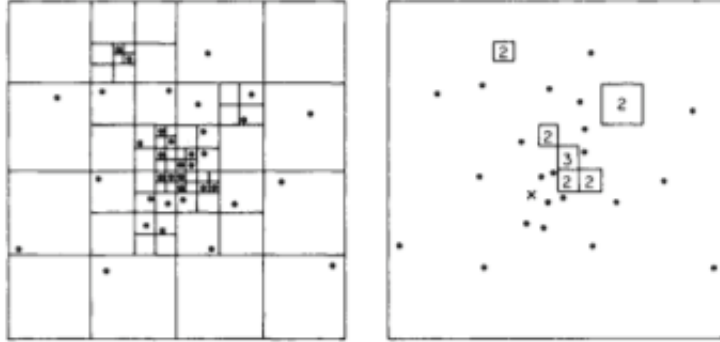
Figure 2.8: Taken from Barnes and Hut (1986): A two-dimensional representation of the hierarchical grouping of particles for force calculation in the tree code. The left panel shows the subdivided cells such that each cell has only one particle. The right panel shows the system in relation to the particle x, using the opening angle critierion. The squares show the particles that are grouped together as a pseudo-particle in the force calculation for x.

the Lagrange points L_1 and L_2. The disruptions take place during pericenter passages. The escaped stars follow the orbit of the satellite closely, but are clearly on different orbits. The stars from the two escaped regions form two streams, an inner one which is on a faster orbit and called the leading arm, and an outer one which lags behind the satellite and is called the trailing arm. Towards the end of the simulation, more features become discernible such as tiny bifurcations in the arms. The insets show the evolution of the progenitor, which gets completely disrupted, although it need not always be the case. It is found that these streams remain coherent for a long period of time (Johnston et al. 1996) since they are far from the dense inner regions, and do not phase-mix quickly. However, they are difficult to detect, especially in external galaxies, since the low mass accretions we are considering here naturally give rise to very faint structures. Another difficulty is the ability to distinguish between streams from multiple accretions, particularly when the progenitors are completely disrupted or obscured. Despite these problems, stellar streams are fast emerging as one of the most powerful potentiometers at the galactic scale.

Chapter 3

Stellar Streams as Probes of Dark Halo Mass and Morphology

This chapter appeared as a publication in the Monthly Notices of the Royal Astronomical Society (Varghese et al., 2011).

Abstract

Tidal streams provide a powerful tool by means of which the matter distribution of the dark matter halos of their host galaxies can be studied. However, the analysis is not straightforward because streams do not delineate orbits, and for most streams, especially those in external galaxies, kinematic information is absent. We present a method wherein streams are fit with simple corrections made to possible orbits of the progenitor, using a Bayesian technique known as Parallel Tempering to efficiently explore the parameter space. We show that it is possible to constrain the shape of the host halo potential or its density distribution using only the projection of tidal streams on the sky, if the host halo is considered to be axisymmetric. By adding kinematic data or the circular velocity curve of the host to the fitting data, we are able to recover other parameters of the matter distribution such as its mass and profile. We test our method on several simulated low mass stellar streams and also explore the cases for which additional data are required.

3.1 Introduction

The global features of the dark matter halos of spiral galaxies such as their mass, shape and extent hold key clues to understanding the nature of dark matter particles as well as galactic evolution and morphology. Simulations of cold dark matter tend to produce halos that are oblate (Dubinski, 1994; Debattista et al., 2008) or triaxial (Frenk et al. 1988; Dubinski and Carlberg 1991; Bett et al. 2007) whereas hot dark matter models yield more spherical halos (Mayer et al., 2002; Bullock, 2002) and baryonic dark matter such as cold molecular gas form disk-like halos (Pfenniger et al., 1994). It is crucial to test these theoretical predictions with observations and to this end, several techniques have been developed to probe the vertical distribution of dark matter around galaxies. These range from methods that are very local, such as measuring the density of dark matter in the Solar neighbourhood which is sensitive to the halo flattening (Kuijken and Gilmore, 1989), to methods based on gravitational lensing (Hoekstra et al., 2004; Mandelbaum et al., 2006). Yet, a conclusive result remains elusive. This is in part due to the small sample of galaxies for which these measurements have been made. The other cause for the disagreement in results may be the systematic differences in the methods themselves. For instance, Olling and Merrifield (2000) measured the flattening of halos based on its effect on the thickness of the H I gas layer in disk galaxies and find that their method tends to yield flatter halos as opposed to other techniques such as those based on warped gas disks. A recent study of halo shapes based on H I flaring can be found in O'Brien et al. (2010a,b,c,d). See Sackett (1999) for a review of earlier work on the subject, and Merrifield (2004) for measurements of the shape of the Milky Way halo. Allgood et al. (2006) contains a more recent comparative study of different methods to determine halo shapes.

Orbits in a potential are simple, yet powerful tracers of the matter distribution. Polar rings in early-type galaxies are a good example of these (Sackett et al., 1994b; Iodice et al., 2003; Combes, 2006). In this paper, we use a similar tracer, namely the stellar streams that are formed by the tidal disruption of globular clusters or dwarf spheroidal galaxies as they fall into the halos of larger spiral galaxies. The stars that make up the stream are ejected from the in-falling satellite due to tidal disruption

and shocks during pericenter passages. The stream stars occupy (approximately) two different orbits that are slightly offset from that of the progenitor, one that is ahead of it and one lagging behind, making up the leading and trailing arms of the stream respectively. The positions of the stream stars can be calculated fairly easily from the orbit of the progenitor (see §3.5). As the geometry of the stream depends on the orbit of the progenitor, which in turn depends on the potential of the host galaxy, it can be used to constrain the parameters of the halo potential or its density distribution. Tidal streams in the halo have the added advantage of being far enough from the bright galactic components that the fitting is unaffected by small errors in the disk and bulge models. Tidal tails formed by interacting disk galaxies in major mergers can also be used to probe the parent halos (Dubinski et al., 1999; Springel and White, 1999), but in this study, we focus solely on stellar streams formed in minor mergers.

Several stellar streams have been observed in the Milky Way; these include the Sagittarius (Ibata et al., 2001b; Majewski et al., 2003), the Orphan (Belokurov et al., 2007; Grillmair, 2006) and the Monoceros tidal streams (Newberg et al., 2002; Conn et al., 2005, 2007, 2008). Stream-like structures have also been observed around many nearby galaxies, for example M31 (Ibata et al., 2001a, 2004), NGC 5907 (Martínez-Delgado et al., 2008), NGC 891 (Mouhcine et al., 2010) and others; refer Martínez-Delgado et al. (2010) for a recent systematic survey of streams in nearby spiral galaxies. Many more remain to be uncovered by future surveys that are increasingly sensitive to low surface brightness objects, enabling an extensive application of techniques based on them. These could provide a large sample of measurements of halo shapes and profiles, which is required if we are going to be able to uncover the generic properties of dark halos and study the possible correlations with their formation histories.

There has been an ongoing effort in recent years to glean information from these streams about their host halo distribution. For example, the fact that the stars of the Sagittarius tidal stream lie on a narrow great circle on the sky (implying little precession) and that the stream has not been dispersed, initially led to the conclusion that the Milky Way has a spherical halo (Ibata et al., 2001b; Majewski et al., 2003). Mayer et al. (2002), Helmi (2004) and Martínez-Delgado et al. (2002) suggested that

this need not necessarily be the case as the debris is dynamically young and may not be sensitive to the shape of the halo. Law et al. (2009) have shown that the Sagittarius tidal stream is best reproduced in a triaxial halo and more recently, a more mildly triaxial halo (Law and Majewski, 2010). Attempts have also been made to constrain the Galactic potential by fitting thin, cold streams found in the Milky Way halo, GD1 (Grillmair and Dionatos, 2006) and Palomar 5 (Odenkirchen et al., 2003), with orbits integrated in a triaxial potential, but the data were found to be insufficient to discriminate between possible solutions, although triaxial models seem to be favored over spherical ones (Lux, 2010). However, by fitting the GD-1 stream with orbits in a logarithmic, axisymmetric potential, Koposov et al. (2010) have estimated the flattening of the Milky Way potential at galactocentric radii near $R \sim 15 \, \text{kpc}$ at 0.9 and a lower limit for the flattening of its halo potential at 0.89.

In general, there are two main challenges that have so far hindered the successful application of tidal streams in constraining halo shapes. One is that tidal streams do not exactly delineate individual orbits in the galactic potential (Eyre and Binney 2009a,b) and treating them as such may result in incorrect estimates. We overcome this hurdle by fitting a given stream with corrected sets of points computed from the progenitor orbit. The other limitation is that in most systems, only projected coordinates of the stream on the sky are available. In closer systems such as the Andromeda galaxy (M31), line of sight velocities are also available and distances to globular clusters or dwarf galaxies that may be the stream progenitors are measurable using the tip of the Red Giant Branch (TRGB method - see McConnachie et al. 2004. In previous studies using tidal streams, the approach has been to try to reproduce the observed streams using a few N-body simulations (typically less than 10). It has been found that the phase space information is insufficient in reasonably constraining the halo parameters using this approach. The N-body technique is severely handicapped by the fact that it is only possible to explore a tiny fraction of the full parameter space with such simulations. We redress this shortcoming by adopting a statistical approach sampling the parameter space of possible progenitor orbits and halo parameters using a Markov chain Monte Carlo routine. The sampling yields distributions of the halo

structural parameters that peak at their most likely values. We find in our tests on simulated streams that it is possible to estimate halo shapes using this method even with limited phase space information. We also find that it is possible to recover line of sight distances along streams in cases where they are not available. In this paper, we explore how much and what information is required to uniquely estimate the orbital and potential parameters using this statistical approach and how the estimates improve with additional data. Later contributions in this series will use the technique developed here to actual observed systems.

3.2 Methodology

Consider a galaxy whose disk lies in the XY plane. We assume that the mid-plane of its bulge and halo coincide with this plane. We also assume that the halos we study are static and have an axisymmetric density profile, even though the density profile of the dark halo is generally considered to be a triaxial ellipsoid (Dubinski and Carlberg 1991; Jing and Suto 2002; Bailin and Steinmetz 2005). The flatness of the distribution is given by the ratio of the polar to the equatorial axis (c/a) and the ovalness by the equatorial axis ratio (b/a). In the most general models, which involve a superposition of ellipsoids, c/a and b/a vary with radius.

However, for the present contribution, we make the simplifying assumption that the equatorial axes are equal ($b/a = 1$), and that the halo has a flattening of $q = c/a$ (we discuss both flattening in the potential and density distribution). Studies have shown that this is a reasonable assumption for the halos of spiral galaxies, especially far from the galactic disk where it becomes spheroidal (Debattista et al. 2008; Kazantzidis et al. 2010).

Throughout the paper, we analyse the specific case of a host galaxy that is viewed edge-on, although the method can be very simply adapted to systems that do not have that geometry. What we have access to are the projected coordinates (x,z) of a tidal stream in its potential, and the width of the stream providing an uncertainty of σ on these coordinate values. The tidal stream has two tails: the leading and the

trailing tails. In reality, each tail consists of several different yet very similar orbits, the stars along these having similar values of energy and angular momentum. The slight difference in these orbits show up in places in the form of bifurcations and small protrusions from the main stellar feature. In this paper, we neglect these tiny features and only consider the longest, contiguous structures that we observe. The method is only applicable in its current simple form to streams of low mass satellites ($\lesssim 10^8 \, \mathrm{M_\odot}$), for which the self-gravity of the stream is negligible. This allows us to ignore dynamical friction which would have to be taken into consideration for more massive and heavily disrupted systems.

The method for fitting the streams is briefly as follows. Different values of the halo potential parameters and the orbital parameters of the progenitor are tested, each set of values corresponding to a point in the multidimensional parameter space. For each set of parameters considered, an orbit is integrated and a set of points is calculated that represents the stream that would be formed by a satellite on the orbit (see §3.5); we refer to this as the trial stream corresponding to the point in parameter space under consideration. Comparing the trial stream to the observed stream (or the N-body generated test stream in the present work), we measure how likely the parameters are to be the ones that generated the observed stream. We sample different values of the parameters using a Markov chain Monte Carlo (MCMC) algorithm, in order to deduce the distribution of parameter values that are consistent with the data. For the galactic halo potential, we use two models: a purely logarithmic halo for its simplicity and a more realistic multiple-slope power-law model.

In §3.4, we explore how the quality of the estimate depends on the quantity and type of information available. We discuss cases for which the streams are shorter or have fewer turning points. We also consider the different kinds of data that may be available and their effect on the accuracy of the estimate. For instance, line of sight velocities and/or distances at some points along the stream or the rotational velocity curve are available for nearby systems. The method is tested on these various cases with pseudo-data generated by N-body simulations.

3.3 The Fitting Routine

In this section, we first briefly discuss the general principles of maximum likelihood estimation and parallel tempering, and then describe how we apply it to fitting tidal streams.

Maximum likelihood parameter estimation is a robust method of determining the parameters of a model that maximize the likelihood of a data set. The likelihood of a set of parameters is the probability of obtaining the given data for those parameter values. Suppose the data set consists of N independent observations of a random variable x which has a probability distribution function $f(x; \Theta)$ that depends on a set of k parameters Θ which are to be estimated, then the likelihood is calculated by the product of the values of the distribution function for each data point (Gregory, 2005):

$$\mathcal{L}(x_1, x_2, ..., x_N | \Theta_1, \Theta_2, ..., \Theta_k) = \prod_{i=1}^{N} f(x_i; \Theta_1, \Theta_2, ..., \Theta_k). \tag{3.1}$$

The estimated values of the parameters Θ are the ones for which this likelihood is maximum. A basic and simple algorithm to find this set of parameters is known as the Metropolis Algorithm, which probes the parameter space in an efficient way to locate the parameters for which the likelihoods are high. The sampling is done by a chain that walks through the parameter space.

For a single chain, the walk through the parameter space basically involves choosing a random point that we consider to move to, and then moving to it or staying put based on a likelihood criterion. Such a chain is known as a Markov chain Monte Carlo (MCMC). A chain is set off at an initial random point $\Theta_{t=0}$ in the parameter space (t being the time step of the MCMC), and we calculate the likelihood at this point, say $\mathcal{L}(\Theta_t)$. Then we consider another point Θ' (the trial point) in the parameter space, from a proposal distribution and calculate its likelihood $\mathcal{L}(\Theta')$. In our algorithm, the proposal distribution is a normal distribution centered on the current point. If the trial point falls beyond the plausible range of the parameters, then we set its likelihood to be arbitrarily low. We calculate the Metropolis ratio, $r = \mathcal{L}(\Theta_t)/\mathcal{L}(\Theta')$. If this is greater than 1, then we take the trial point as the next point in the chain. If

$r < 1$, then we pick a uniform random number U between 0 and 1. If $U \leq r$, then we take the trial point as the next point ($\Theta_{t+1} = \Theta'$), else we stay at the same point ($\Theta_{t+1} = \Theta_t$). Proceeding in a similar fashion, we explore the full parameter space.

Parallel Tempering

In many cases, especially in multidimensional parameter space, there are usually many local likelihood maxima, whereas we seek the global maximum. Using only a single chain, the algorithm often becomes stuck in a local maximum. To avoid this, multiple chains of different "temperatures" are used to step through the parameter space. Effectively, this means that for a chain of temperature T, its likelihood is raised to the power of the inverse of its temperature, i.e.:

$$\mathcal{L}_{\beta_i} = (\mathcal{L}_1)^{\beta_i} , \tag{3.2}$$

where $\mathcal{L}_1$ corresponds to the likelihood at a temperature of 1 (given by equation 3.1 in general, which reduces to equation 3.4 for the present study) and $\beta_i = 1/T_i$. T_i is the temperature of the ith chain. As T ranges from 1 to infinity, β takes values from 1 to 0. The higher temperature chains are less sensitive to the likelihood, and take larger strides through the parameter space. Suppose we use n parallel chains and swap their states after every n_s steps on average. The higher temperature chains pull out the colder chains from local maxima they may be stuck in. The algorithm for the swapping of chains is as follows:

1. At each step, choose a uniform random number U_1 between 0 and 1. A swap is proposed if $U_1 \leq 1/n_s$.

2. If a swap is proposed, we consider swapping the states of chain i and $i + 1$, where i is a random integer between 1 and $n - 1$.

3. Calculate the swapping probability,

$$r = \frac{\mathcal{L}_{\beta_i}(\Theta_{t,i+1})\mathcal{L}_{\beta_{i+1}}(\Theta_{t,i})}{\mathcal{L}_{\beta_i}(\Theta_{t,i})\mathcal{L}_{\beta_{i+1}}(\Theta_{t,i+1})} \tag{3.3}$$

where $\Theta_{t,i}$ and $\Theta_{t,i+1}$ are the current points on the ith and $(i+1)^{th}$ chains respectively, and $\mathcal{L}_{\beta_i}(\Theta_{t,i+1})$ is the likelihood of $\Theta_{t,i+1}$ if it were on the ith chain.

4. Choose another uniform random number U_2 between 0 and 1. Accept the swap if $U_2 \leq r$.

5. The maximum corresponding to the coldest chain $T = \beta = 1$ is the global maximum.

The efficiency of the algorithm is sensitive to the size of the proposal distribution. If it is too small, then most of the trial points are accepted and the MCMC is slow to sample the full parameter space. If it is too large, most of the trial points are rejected and though the MCMC may make large jumps in parameter space, it could become stuck at a certain point for long. For the present work, optimal sizes of the proposal distributions for the parameters were found experimentally, by requiring that the acceptance rate lie between 15% and 40%. Note that it is possible, however, to automate the process such that the routine finds an optimal size for the proposal distribution (Gregory, 2005). It is important to check that the MCMC converges on a solution. One way of checking for convergence is to sample the parameter space with chains that start at different initial points and to check if they yield similar solutions. Once convergence has been achieved (i.e. a chain is well-mixed), the distribution is independent of the number of MCMC steps and is said to be stationary. The initial steps of the chain are discarded to forget the starting point. This is known as burn-in and is typically around $10,000$ steps in our test cases. The remaining steps of the chain form a sample distribution of the parameters. The estimated value of a parameter corresponds to the peak of its marginalized distribution. The accuracy of the estimate is equal to the standard deviation of the distribution, if it turns out to approximate a Gaussian distribution. However, the parameter distributions may turn out to be multimodal or otherwise complex. As the specific details of the parameter distributions vary from stream to stream, we defer the discussion of accuracies and convergence tests to when we apply the method to real, observed streams. For a detailed discussion of Parallel Tempering and maximum likelihood estimation, see

Gregory (2005).

3.3.1 Estimation of Halo Parameters

By defining the parameter space and the likelihood calculation for the parameters, we can use the above method to find an orbit that best reproduces a given stream (after the required corrections explained in §3.5), thereby also estimating the model parameters that we wish to determine. A point in the parameter space corresponds to an orbit, which is parametrized by its initial position and velocity components $(x_0, y_0, z_0, v_{x_0}, v_{y_0}, v_{z_0}$ at $t = 0)$, in addition to the potential or density distribution parameters. Depending on the information available, few of these initial phase space coordinates are known. The remaining orbital parameters are set to be free parameters with physically reasonable ranges. The best fit orbit corresponds to the one with the highest likelihood. The main processes involved in the algorithm are: (1) Stepping through the parameter space, (2) Integrating orbits corresponding to the points in the parameter space, (3) Generating a corrected set of points (trial stream) corresponding to an orbit and (4) Calculating the likelihood of these trial streams.

As the several MCMC chains step through the parameter space, we integrate orbits at each step with a fourth-order Runge-Kutta integrator starting from an initial point defined by the parameters. For fitting the streams, we calculate a set of n points $\{S(n)\}$ via a correction mechanism (detailed in §3.5) from the integrated orbit. Assuming a Gaussian distribution for the parameters, the likelihood of a trial orbit is calculated as:

$$\mathcal{L} = \prod_{i=1}^{N} \frac{1}{\sigma_i \sqrt{2\pi}} e^{-\frac{D_i^2}{2\sigma_i^2}}, \tag{3.4}$$

where N is the number of data points and σ_i is the uncertainty in each data point, which includes both the width of the stream as well as measurement errors. D_i is the distance of each data point on the observed stream from the corrected set of points, i.e. the distance of a data point to its closest point on the trial stream. As not all of the phase space information is available, the distance D_i only includes the distances along the coordinates for which data are available. For instance, if the projected

positions x_i, z_i and line of sight (l.o.s) velocities v_{y_i} are observed, then the exponent in equation 3.4 reduces to:

$$\frac{D_i^2}{2\sigma_i^2} = \sum_i \frac{(x_i - x_c)^2 + (z_i - z_c)^2}{2\sigma_{xz_i}^2} + \frac{(v_{y_i} - v_{y_c})^2}{2\sigma_{v_i}^2} \,, \tag{3.5}$$

where x_c, z_c, v_{y_c} are the closest points on the trial stream to the data point x_i, z_i, v_{y_i} and $\sigma_{xz_i}, \sigma_{v_i}$ are the uncertainties in position and velocity. The σ_i in the normalizing coefficient of the exponent in equation 3.4 is the product of the uncertainties in the different phase space coordinates, which in this example reduces to $\sigma_{xz_i}\sigma_{v_i}$.

In our tests, we used four parallel chains to search the parameter space, the inverse of the temperature of the ith chain being $\beta_i = 1/i^2$. The states of the chains are considered for swapping after every thirty steps on average. At the beginning of the parallel tempering, all the chains are initialized by setting the free parameters to physically plausible random values. We checked that the results were insensitive to these starting values. Given the stream data, the likelihood of the orbit corresponding to the initial point is calculated with equation 3.4. This is the likelihood of the starting point for the coldest chain, $i = 1$. The likelihoods for the same point on the hotter chains are calculated using equation 3.2.

Having calculated the likelihoods for the initial point, the next point on each MCMC has to be chosen. For this, a trial point is chosen for each chain. This can be done in many ways. In our case, if Θ_t is the current value of the parameter Θ, then the next point for consideration Θ' is drawn randomly from a normal distribution centered on Θ_t. The width of the proposal distribution, *i.e.* the size of the step, depends on the expected range of the parameters. It also helps to use different step sizes for the different chains to enable sampling the parameter space at various scales. The algorithm is run until the chains are well mixed, which could take from approximately one hundred thousand to a million steps (depending on the stream and halo model), and the marginalized distributions of the parameters are drawn from the coldest chain.

3.4 Testing with Orbits (not streams)

To get a heuristic idea of the effectiveness of the method, we first investigated how well it constrains potential parameters using ideal orbits in both logarithmic halos and double power law density halos. The primary aim was to explore if and when the projected positions of an orbit are sufficient to estimate the density or potential flattening and how additional information would affect the accuracy of the estimation.

3.4.1 Orbits in a Logarithmic Potential

Consider the set of orbits shown in Figure 3.1. These were integrated in a logarithmic halo given by (Binney and Tremaine, 2008):

$$\Phi_{halo} = \frac{1}{2} V_0^2 \ln \left(R_c^2 + R^2 + \frac{z^2}{q_\phi^2} \right) \tag{3.6}$$

in cylindrical coordinates, where q_ϕ is the potential flattening, V_0 is the circular velocity, and R_c is the core radius. For this initial test, we neglect the contribution of the bulge and the disk to the potential. The orbital and potential parameters of each of these are listed in Table 3.1. A logarithmic halo has the advantage of having only three parameters, thereby minimizing possible degeneracies between the different models. Using only the projected positions of these orbits, we find that the flattening q_ϕ and initial line of sight distance of the orbit from the center of the galaxy y_0 are easily constrained as shown in Figures 3.2 and 3.3, whereas the circular velocity is degenerate and cannot be constrained with only positional information (Figure 3.4). It is to be noted that there may be a sign discrepancy in the distance estimate, as orbits with either value of y_0 will be identical in projection. Therefore, we restrict the fitting routine to positive y_0 space and only the magnitude of the progenitor distance is recovered. The orbits in this set are fairly long and have more than two turning points. However, several observed streams are much shorter. In order to analyze the effect of the length of an orbit and more importantly, the number of turning points of the orbit, on the estimate of the flattening, we fit shorter versions of the orbit
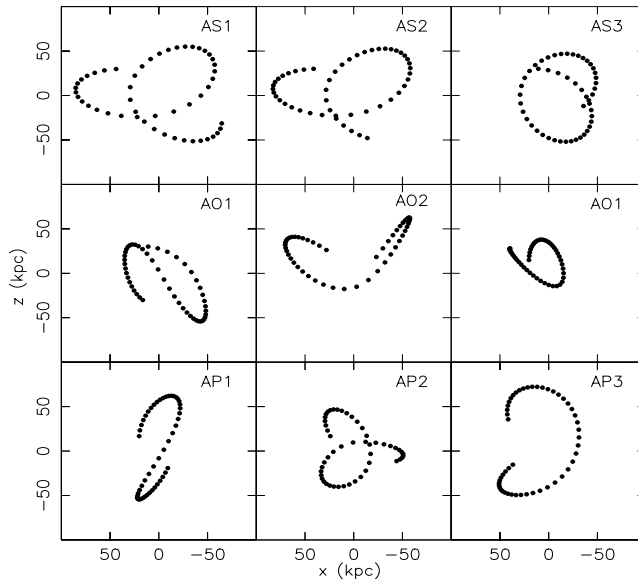
Figure 3.1: Projection in the XZ plane of orbits integrated in a logarithmic potential using a Runge-Kutta scheme. The dots indicate the positions on the orbits that are used as data points in the fitting. The top, middle and bottom panels show orbits in spherical, oblate and prolate potentials respectively. The parameters of each orbit are listed in Table 3.1.

AS1 (Figure 3.5). Not surprisingly, having fewer turning points on an orbit causes a spread in the estimated value of q_ϕ. Adding more information to the fitting (line of sight velocities for BS1 and line of sight velocities and distances y for CS1) results in much more accurate estimations of q_ϕ as shown in the bottom panels of Figure 3.5. As for the distance to the progenitor, y_0, it is strongly constrained (with a sign discrepancy) for BS1 even only with the projected positions and for CS1, if kinematic information is provided (but not with only the projection), making it the most easily constrainable parameter.
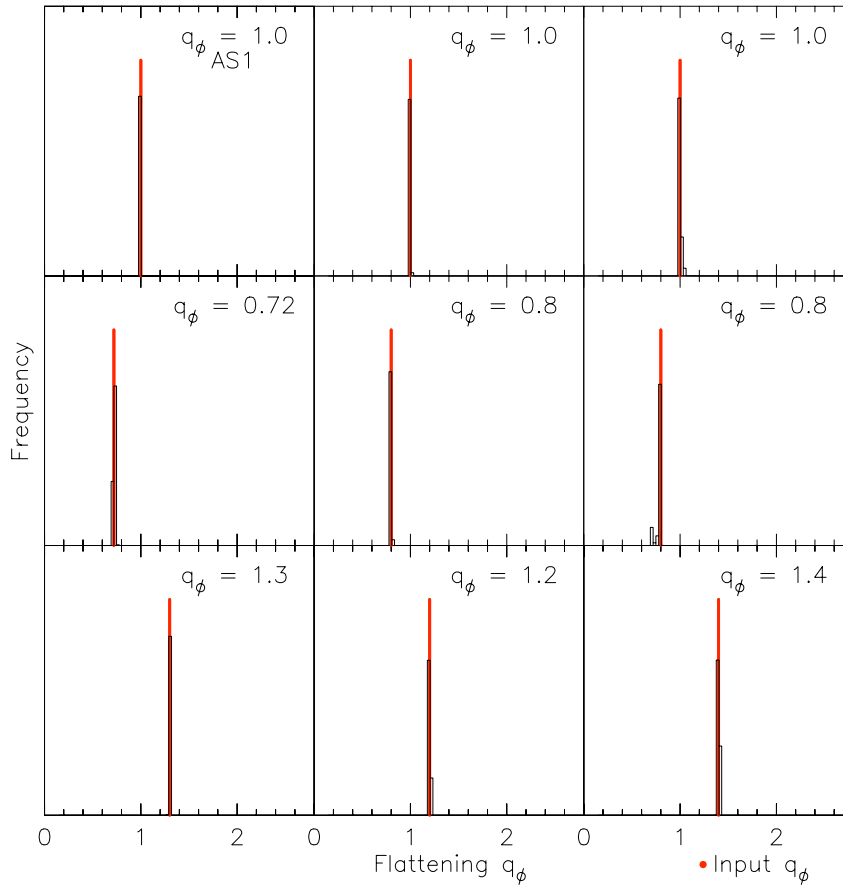
Figure 3.2: Estimation of q_ϕ for the projected orbits shown in Figure 3.1. The input value of q_ϕ in each case is shown. This distribution is drawn from 100,000 steps of the coldest MCMC chain. The excellent correspondence with the input values shows that the shape of a logarithmic potential can be accurately recovered from the spatial projection of some orbits within it.
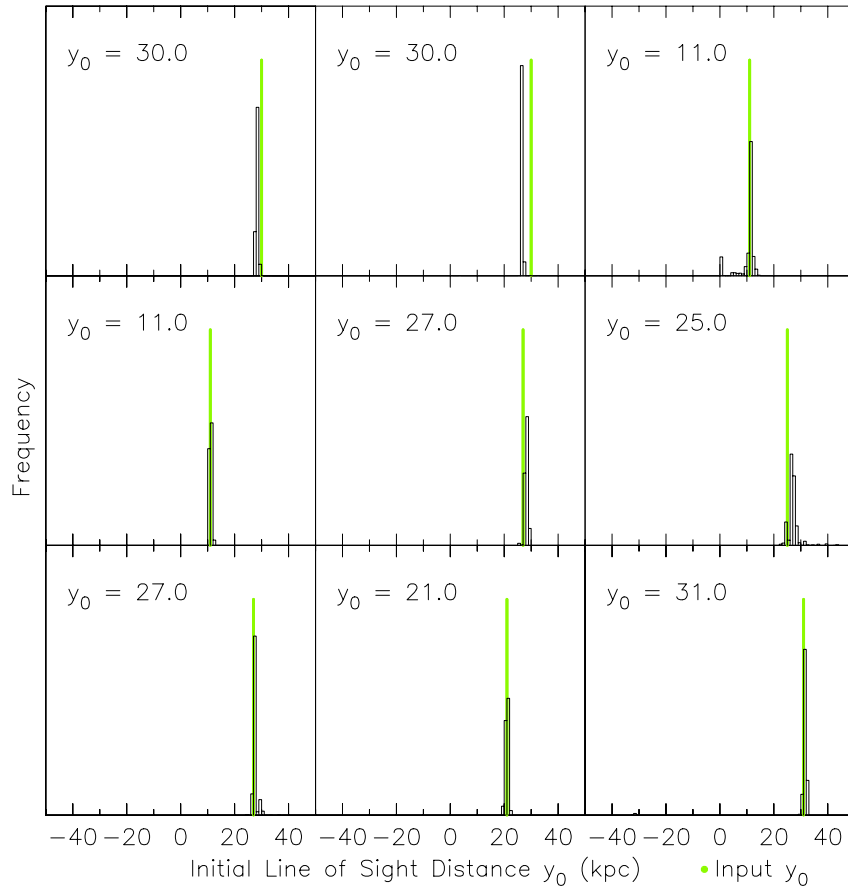
Figure 3.3: Estimation of y_0 for the projected orbits shown in Figure 3.1. The input value of y_0 in each case is shown. This distribution is drawn from 100,000 steps of the coldest MCMC chain, and clearly peaks near the input value. The fitting routine only considers positive values for y_0 as orbits that are symmetrical about the XZ plane will have identical positions (so there may be a sign discrepancy in the estimated value of y_0).
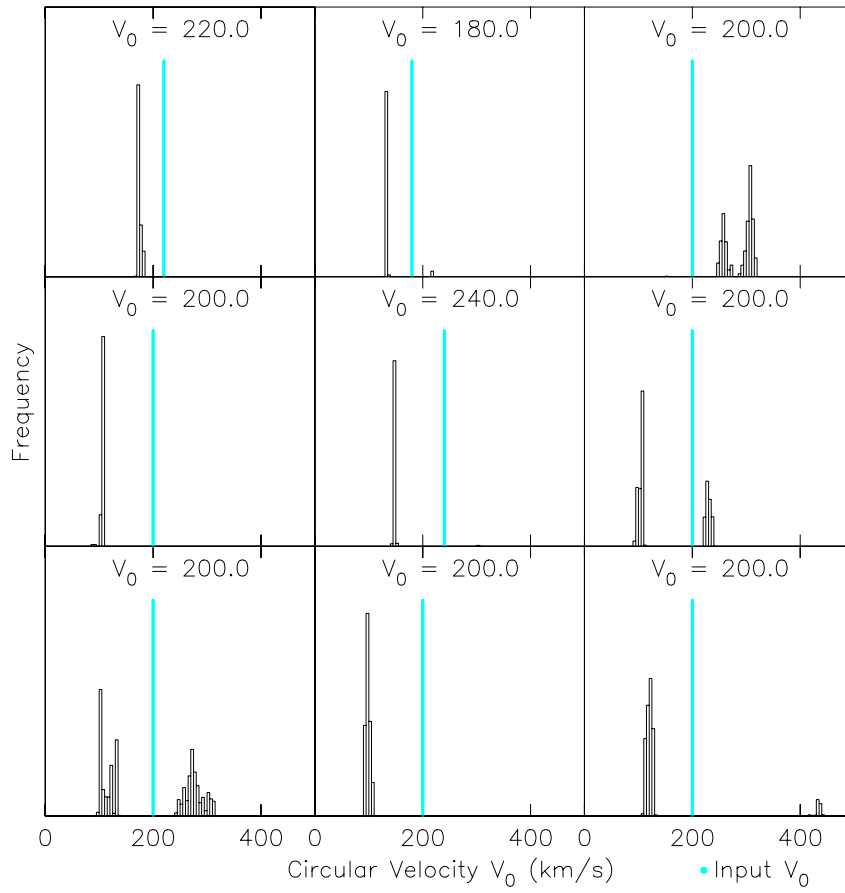
Figure 3.4: Estimation of V_0 for the orbits shown in Figure 3.1. The input value of V_0 in each case is shown. This distribution is drawn from 100,000 steps of the coldest MCMC chain. We see that the peaks of the distribution vary greatly from the input value, which implies that the orbits are not uniquely dependent on the circular velocity.
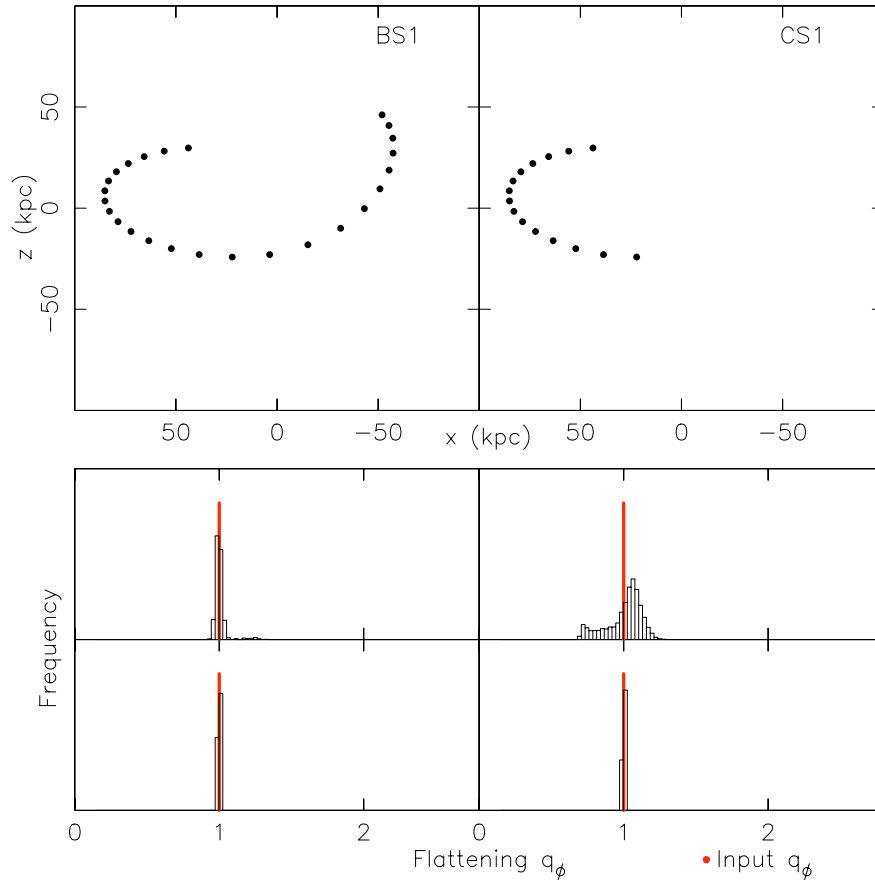
Figure 3.5: Fitting shorter versions of the orbit AS1 ($q_\phi = 1$). BS1 has two turning points and CS1 only one. The middle panels show the q_ϕ distributions obtained by fitting only the projected positions of these orbits. The spread in the distribution increases with decreasing turning points. The bottom panels show the q_ϕ distribution obtained by adding more information to the fitting: the line of sight velocities v_y for BS1, the distances y and line of sight velocities v_y for CS1.
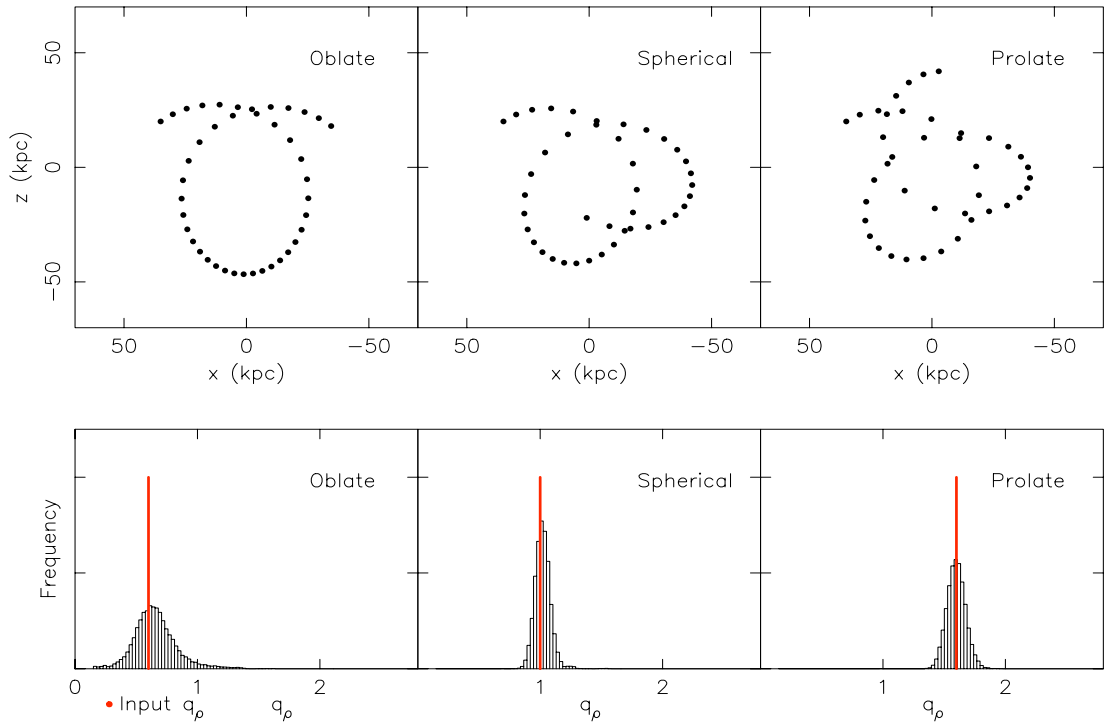
Figure 3.6: Estimation of q_ρ for the orbits shown in the top panel. The host galaxy models in these examples are a one-component ellipsoidal halo (Equation 3.7). The input value of q_ρ in each case is marked in red. These distributions are drawn from 2,000,000 steps of the coldest MCMC chain.

Table 3.1: Series of Logarithmic Orbits: The following are the potential and orbital parameters of the orbits shown in Figure 3.1. q_ϕ, R_c and V_0 are the potential flattening, core radius and circular velocity respectively. x_0, y_0, z_0 are the initial positions and $v_{x_0}, v_{y_0}, v_{z_0}$ the initial velocities used.

Name	q_ϕ	R_c (kpc)	V_0 ($\mathrm{km\,s^{-1}}$)	x_0 (kpc)	y_0 (kpc)	z_0 (kpc)	v_{x_0} ($\mathrm{km\,s^{-1}}$)	v_{y_0} ($\mathrm{km\,s^{-1}}$)	v_{z_0} ($\mathrm{km\,s^{-1}}$)
AS1	1.0	2.0	220	30.0	30.0	30.0	250.0	10.0	10.8
AS2	1.0	3.0	180	30.0	30.0	30.0	200.0	10.0	10.8
AS3	1.0	5.0	200	20.0	10.0	30.0	-230.0	40.0	20.0
AO1	0.72	5.0	200	20.0	10.0	30.0	-230.0	40.0	20.0
AO2	0.8	1.0	240	20.0	20.0	20.0	220.0	200.0	180.0
AO3	0.8	3.0	200	20.0	20.0	10.0	20.0	200.0	180.0
AP1	1.3	3.0	200	20.0	20.0	10.0	20.0	200.0	180.0
AP2	1.2	3.0	200	20.0	20.0	10.0	120.0	50.0	180.0
AP3	1.4	3.0	200	40.0	30.0	30.0	50.0	50.0	150.0
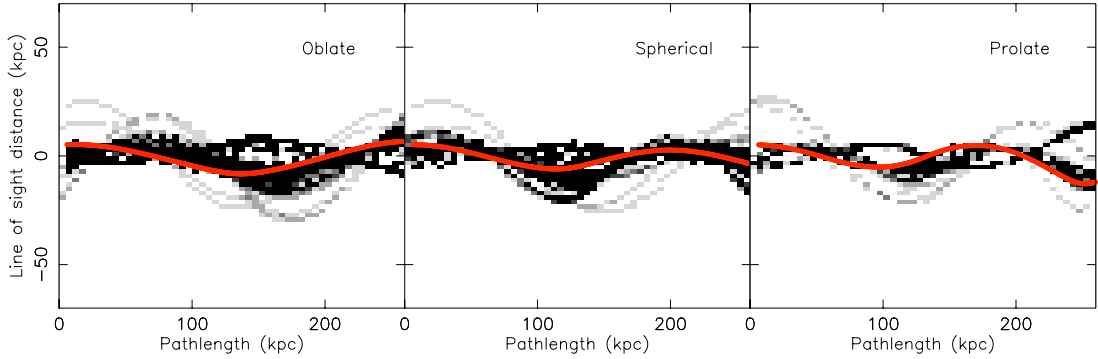
Figure 3.7: Recovery of the three dimensional structure of orbits with only their projections on the XZ plane. The grayscale image shows the density of the line of sight distances along the trial orbits considered in the coldest MCMC chain used in the fitting of the orbits shown in Figure 3.6. The red line marks the actual distance along the input orbits. This figure shows that coarse estimates of the distances along the orbit can be obtained.

3.4.2   Orbits in a Spheroidal Halo

A more general halo is described by a double power law density distribution (Dehnen and Binney, 1998)

$$\rho_s = \rho_0 \left(\frac{s}{r_0}\right)^{-\gamma} \left(1 + \frac{s}{r_0}\right)^{\gamma - \beta} e^{-s^2/r_t^2} , \tag{3.7}$$

where s is the ellipsoidal coordinate

$$s \equiv \left(R^2 + z^2/q_\rho^2\right)^{1/2} . \tag{3.8}$$

The model parameters that are unknown are the central density ρ_0, the inner and outer slopes γ, β, the scale radius r_0 and the flattening in density q_ρ. We calculate the potential due to this distribution by multipole expansion using an algorithm similar to 'GalPot' (Dehnen and Binney, 1998; Binney and Tremaine, 2008). The truncation radius r_t is fixed at $1000\,\text{kpc}$, but its precise value does not affect orbits at the radial distances under consideration. We find that the inner slope γ cannot be constrained by orbits that are far away from the center of the galaxy and that small variations in γ do not affect the fits. Hence, we adopt a fixed value of $\gamma = 1$, equivalent to the central power-law slope of a NFW profile (Navarro et al. 1996), for the orbital fitting and set the remaining parameters to be free. Figure 3.6 shows the distributions in the flattening q_ρ obtained by fitting the projections of three orbits in this power-law spheroidal halo. Even though the distributions peak at the right values of q_ρ, they are much more spread out than the previous distributions in q_ϕ. This is to be expected, as orbits respond directly to the potential, and these are rounder than their corresponding mass distributions. For a logarithmic potential, at distances much larger than the core radius, the relation between q_ϕ and q_ρ can be approximated as (Binney and Tremaine, 2008):

$$1 - q_\phi \approx \frac{1}{3} \left(1 - q_\rho\right) . \tag{3.9}$$

The fitting mechanism also turns out to be extremely useful in approximating the line of sight distances along the orbit as revealed by a grayscale plot of the distances
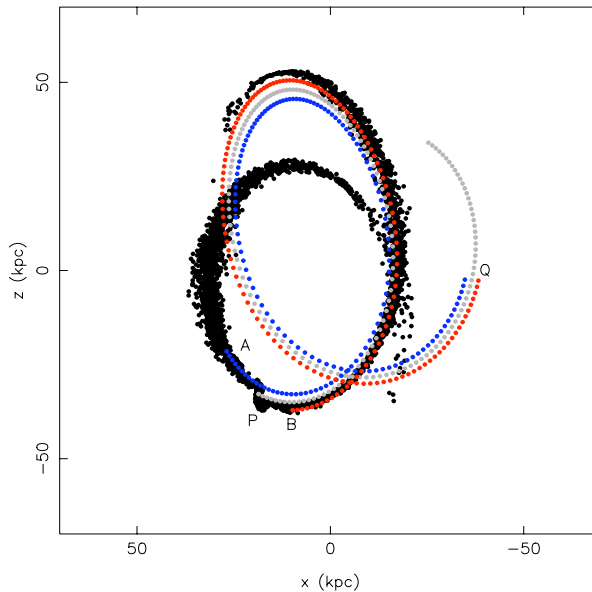
Figure 3.8: Correction Mechanism: Calculating a pair of corrected points on the leading and trailing tails corresponding to a point on the past orbit of the progenitor. The black dots are particles from an N-body simulation of the stream. The grey dotted curve shows the backward integrated orbit of the progenitor, starting from its current position at P. Q is an arbitrary point on this orbit. The blue and red dotted curves are the orbits of stars which escape the progenitor system at Q from the inner and outer escape points respectively. The end points of these orbits lie on the leading and trailing arms of the stream, marked as A and B. The velocity components at Q of the blue and red orbits are the same as that of the grey orbit (with the opposite sign). This process is repeated for several points along the grey curve to obtain a set of corrected points like A and B that demarcate the stream path (see Figure 3.9).

along the various trial orbits on the coldest MCMC chain (Figure 3.7).

3.5 Testing with streams in a spheroidal potential

Having demonstrated the power of the technique in constraining the parameters of a density distribution by fitting only the projected positions of orbits, we test its ability to robustly estimate the same by fitting streams which, as mentioned in §3.1, do not delineate the orbit of the progenitor or any other exact orbit in the potential. A consistent and fast mechanism is required to derive the positions of stream stars
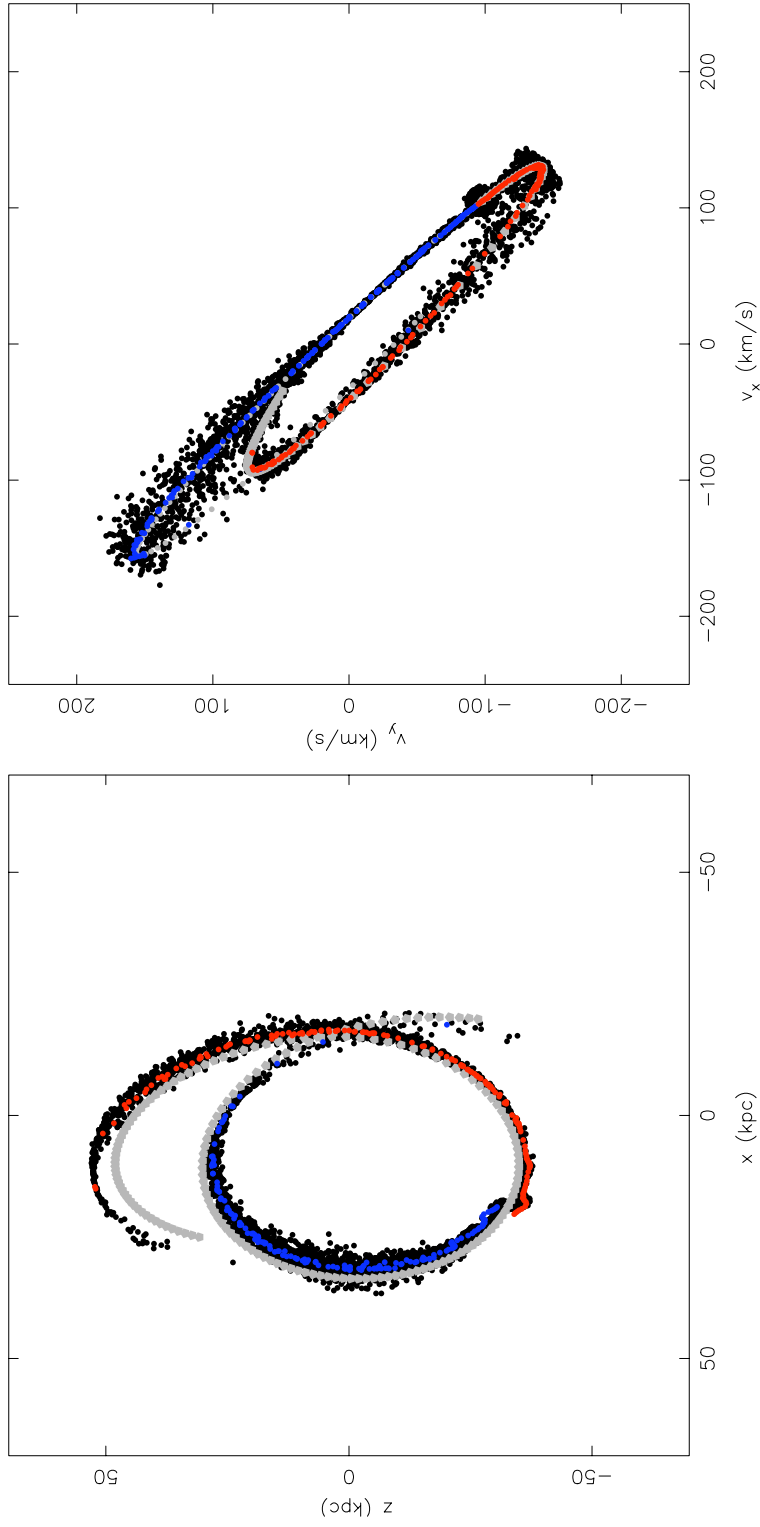
Figure 3.9: Correcting for tidal tails: The left and right panels show stream B in the XZ and V_xV_z planes, respectively. The black dots are particles from an N-body simulation of the stream. The grey dotted curve is the orbit of the progenitor, the remnant of which is the concentrated sphere. The blue and red dots are the corrected points for the leading and trailing arms, respectively. The very close correspondence between the computationally-expensive N-body simulation and the locus of the "corrected stream" points is evident.
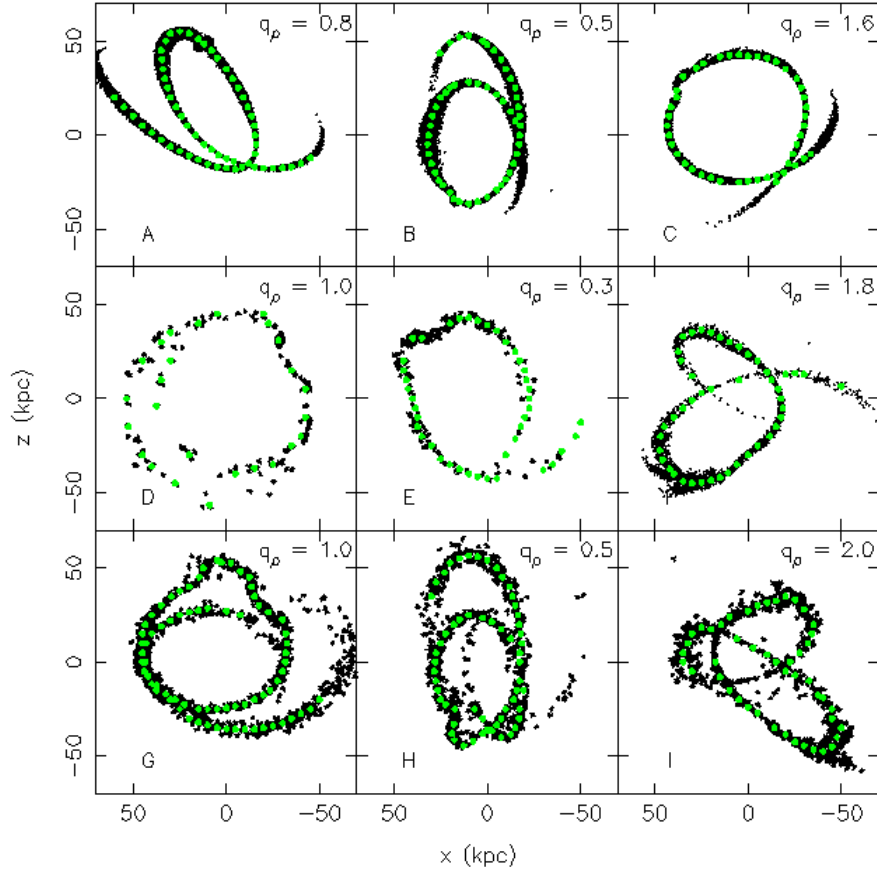
Figure 3.10: The projection of test streams generated by N-body integrations using *gyrfalc(ON)* in a realistic multi-component galaxy model with bulge, disk, thick disk, ISM and halo components. The q_ρ value indicated on each panel is the flattening of the halo used in each simulation. The streams in the top, middle and bottom panels were generated from satellites with initial masses of $5.0 \times 10^6 \, M_\odot$, $5.0 \times 10^7 \, M_\odot$, and $1.0 \times 10^8 \, M_\odot$ respectively. The green dots are the points taken along the streams to fit trial streams to.
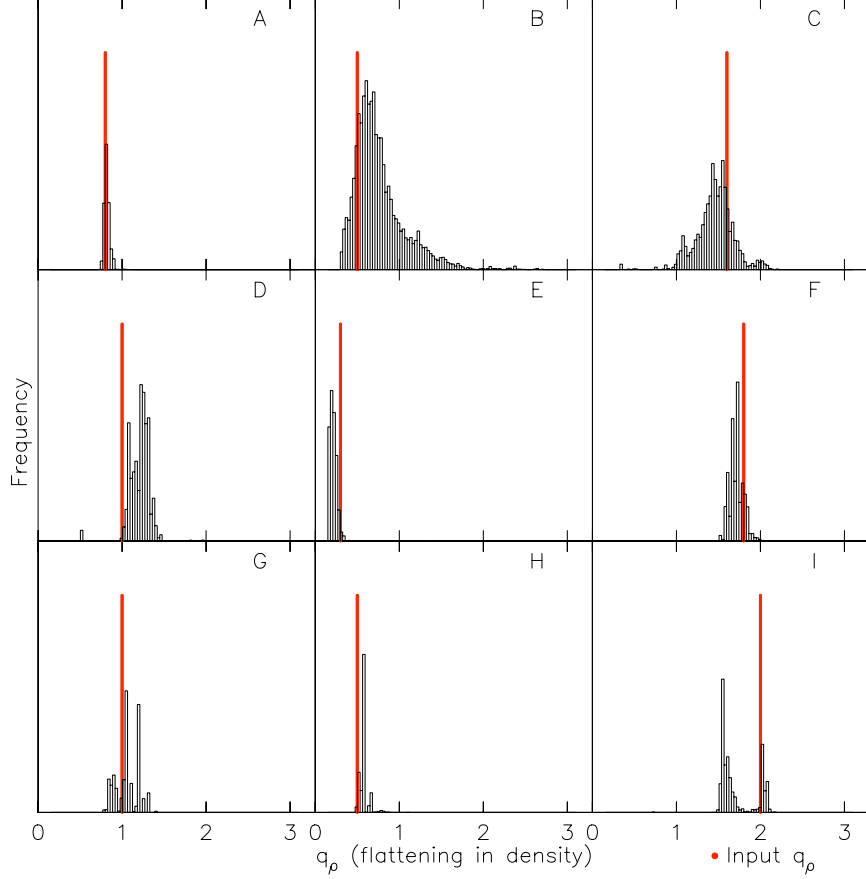
Figure 3.11: Estimation of the density flattening q_ρ with only projections of streams. Shown here are the distributions of q_ρ obtained by fitting the projection of streams shown in Figure 3.10. The number of progenitor orbits attempted vary from $500,000$ to $1,000,000$ from stream to stream. The red lines indicate the input q_ρ for each. We find that the accuracy of estimation varies from stream to stream. In all the cases, the distributions indicate the right shape of the halo (oblate, spherical or prolate). For fitting streams B and E, the inner power slope γ was kept fixed at 1.0 though its true value is 1.28. This does not introduce any significant error on the estimate of the density flattening. For fitting stream H, we set γ to be a free parameter and this does not affect the estimate on q_ρ either. For stream I, there are two peaks in the distribution, the actual value of q_ρ being at the smaller peak. However, the streams generated at the smaller peak resemble the test stream in finer details, such as its bifurcations, which were not included in the fitting data.
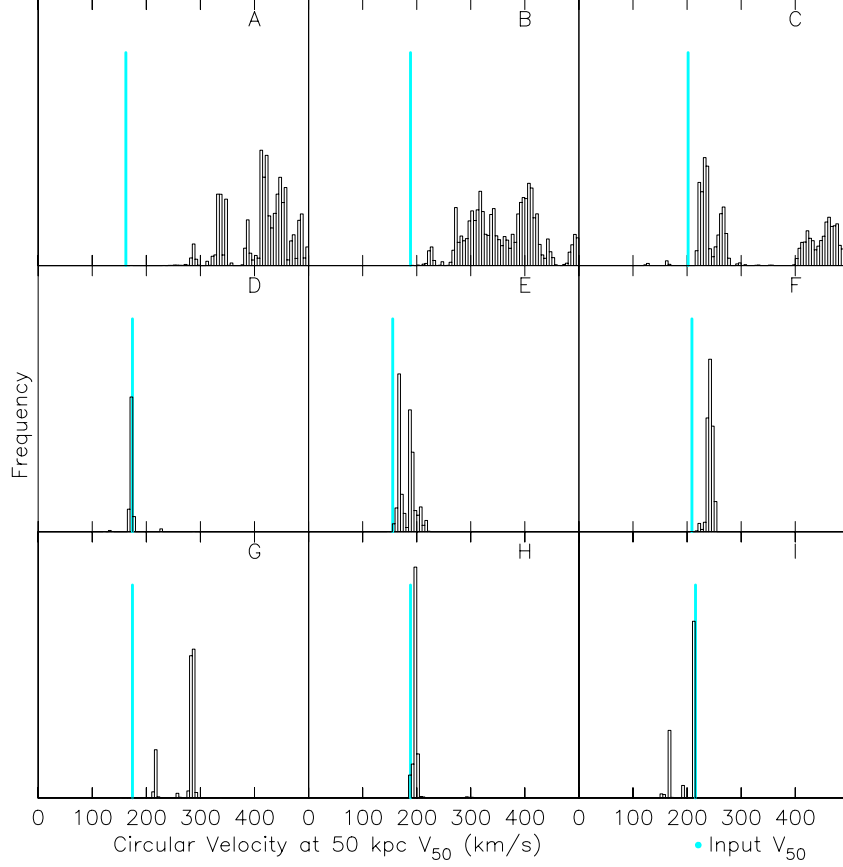
Figure 3.12: Estimating the mass of the halo with only projections of streams. We use the circular velocity at 50 kpc, V_{50}, as an indirect mass parameter. The value of V_{50} is calculated using the potential parameters at each step of the coldest MCMC for the fitting of the streams shown in Figure 3.10. These are the distributions in V_{50} thus obtained for these streams. The cyan lines indicate the input V_{50} for each. It is seen that it is impossible to estimate V_{50} and the mass of the halo with only positional information. The algorithm finds highly likely solutions at different values of mass of the halo. This is because several streams (like orbits) exist that are identical in projection, but different in velocity space, for different values of the halo mass. As a result, the algorithm, in many cases, does not even reach the correct input V_{50} value.
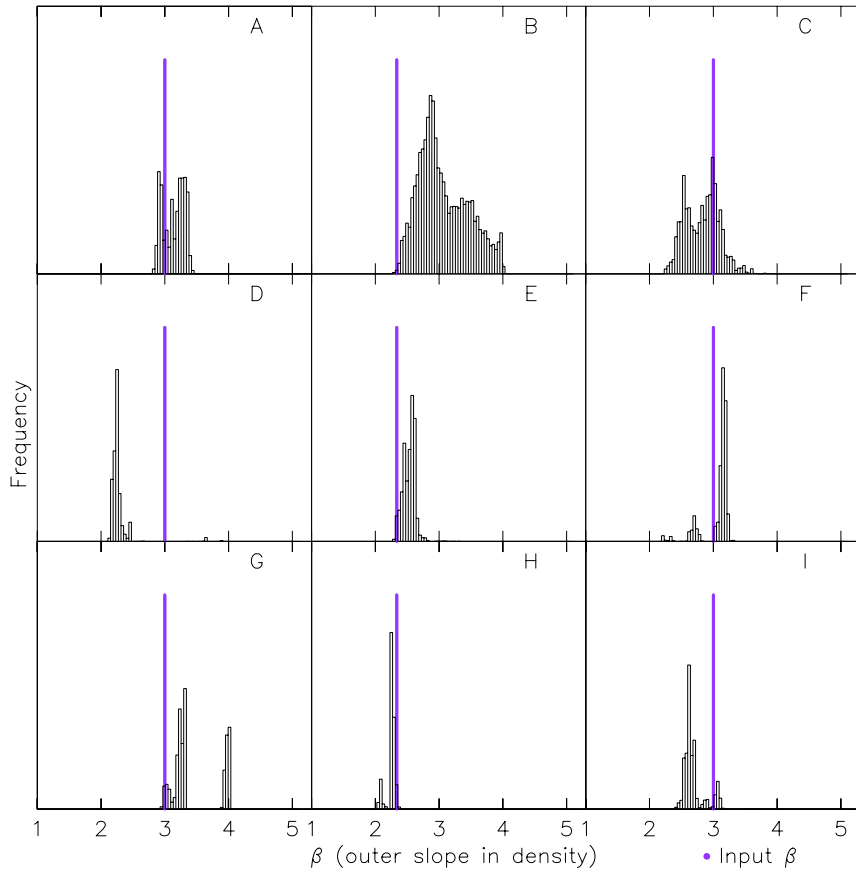
Figure 3.13: Estimating the outer power law β with only projections of streams. Shown here are the distributions of β obtained by fitting the projection of streams shown in Figure 3.10. The violet lines indicate the input β for each. This shows that β cannot be constrained by the 2-dimensional positional information alone.
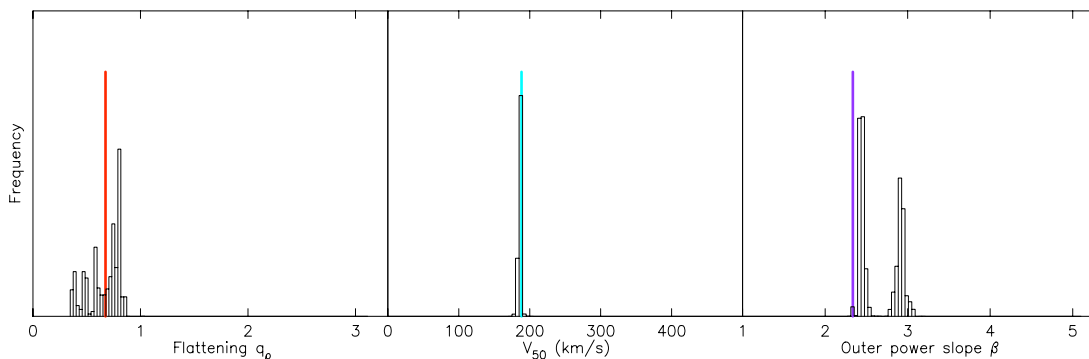
Figure 3.14: Effect on the estimates of parameters of adding the rotational velocity curve of the host galaxy to the projection of a stream. The panels from left to right show the distributions in the density flattening q_ρ, circular velocity at $50\,\mathrm{kpc}$ V_{50}, and outer power law β respectively, for stream B, when the inner circular velocity curve (which extends up to $30\,\mathrm{kpc}$ for this case) is also provided in addition to the projected positions. The true values of each of these are marked in red, cyan and violet respectively. It is seen that the provision of the rotational velocity curve accurately constrains the V_{50} value as expected. This, in turn, helps constrain other parameters of the model, such as β.

from the progenitor's orbit, without using N-body integration. The stars which make up the stream are those which were tidally ripped from the satellite during pericenter passages. Based on this, it is possible to formulate a simple correction mechanism that maps a given progenitor orbit to the coordinates of its tidal tails.

Consider the stream shown in Figure 3.8, whose projection in the $V_x V_z$ plane is shown in the right panel of Figure 3.9 (it is the same as stream B in Figure 3.10, which was integrated in an oblate halo). The grey dotted curve is the orbit of the progenitor, the remnant of which is the concentrated sphere. The progenitor's orbit corresponds to a set of orbital parameters (the progenitor's current position and velocity components) and potential parameters. The stars that lie on the tidal tails escaped the progenitor at earlier times, from two regions of the satellite: one that is closest to the center of the host galaxy and one that is farthest from it. We refer to these points as the inner and outer escape points respectively, which approximate the inner and outer Lagrange points in a restricted three-body problem. Therefore,
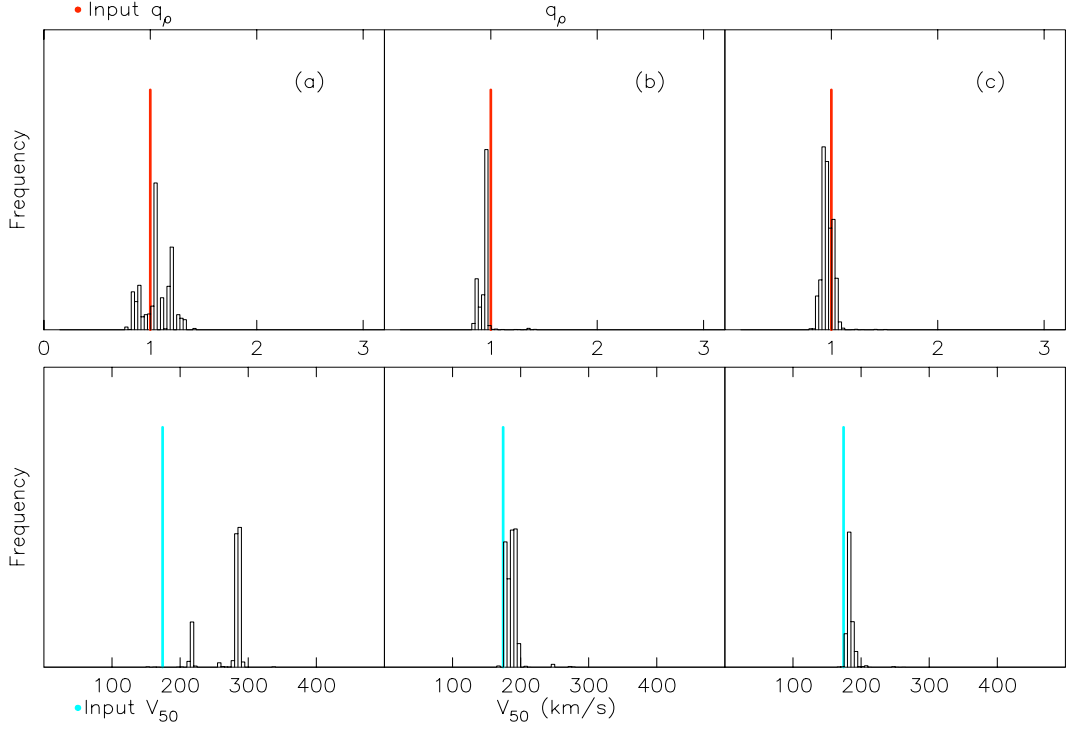
Figure 3.15: Effects on the estimates of q_ρ and V_{50} when l.o.s velocities are added to the projection of the stream. The top panels show the distributions in q_ρ and the bottom panels the corresponding distributions in V_{50} for stream G, that was generated in a perfectly spherical potential. The true values of q_ρ and V_{50} of the model are marked in red and cyan respectively. In (a) only the projection of the stream on the sky is used, and a reasonably good estimate of the flattening obtained, whereas the estimate of V_{50} is poor. Adding the line of sight velocity v_{y_0} of the progenitor to the projection of the stream (but no rotational curve) greatly improves the estimates of V_{50} as well as q_ρ (b). Adding to this five l.o.s velocity data points for each tail further improves the estimation of these parameters (c).
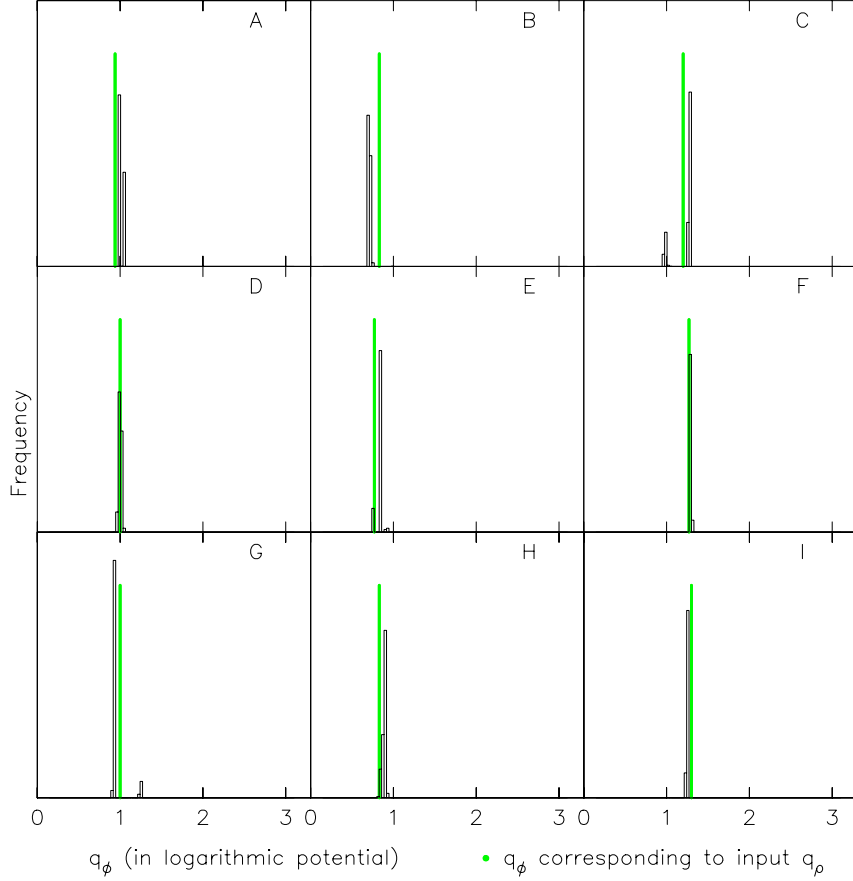
Figure 3.16: Distributions of q_ϕ obtained when the test streams (generated in a multicomponent host potential with a double spheroidal halo) are fit in a logarithmic potential, without any stellar components. The green lines indicate the flattening in potential q_ϕ corresponding to the input flattening in density q_ρ of the host halo calculated using equation 3.9. It is seen that by using a logarithmic halo to fit streams that were generated in a double power law density model, the flattening in the potential can still be recovered.
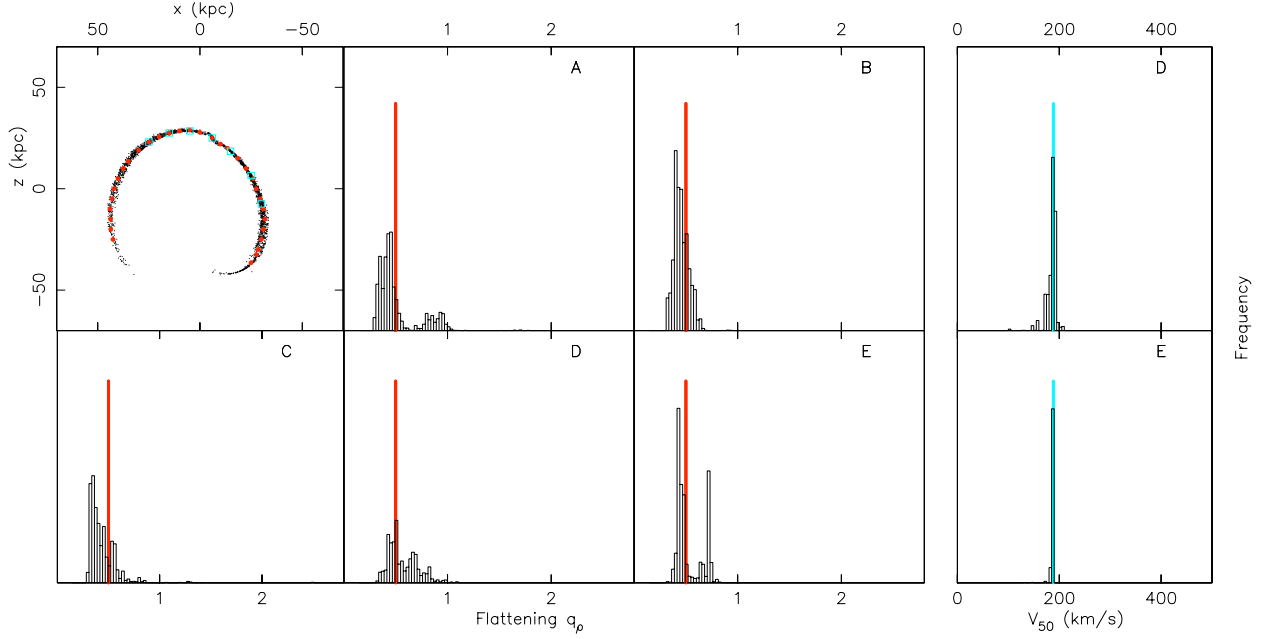
Figure 3.17: Estimation of q_ρ and V_{50} for a short stream with only one prominent turning point. The red line shows the input value of q_ρ. The distributions are drawn from 500,000 steps of the coldest MCMC chain. Case A: only projected positions, red dots show the points used in the fitting. Case B: projected positions and l.o.s velocities at cyan squares. Case C: projected positions and distance to the progenitor. Case D: projected positions, distance to the progenitor and l.o.s velocities at cyan squares. Case E: Same as Case D but with the rotational velocity curve given. The rightmost panels show the estimation of the circular velocity at 50 kpc for case D and E, the cyan lines indicating its true value. It is not possible to constrain V_{50} without any velocity information, but if l.o.s velocities are provided (case D), it can be estimated even with a short stream like the one above. It is not surprising that V_{50} is very well constrained in case E as the circular velocities up to 30 kpc are given.
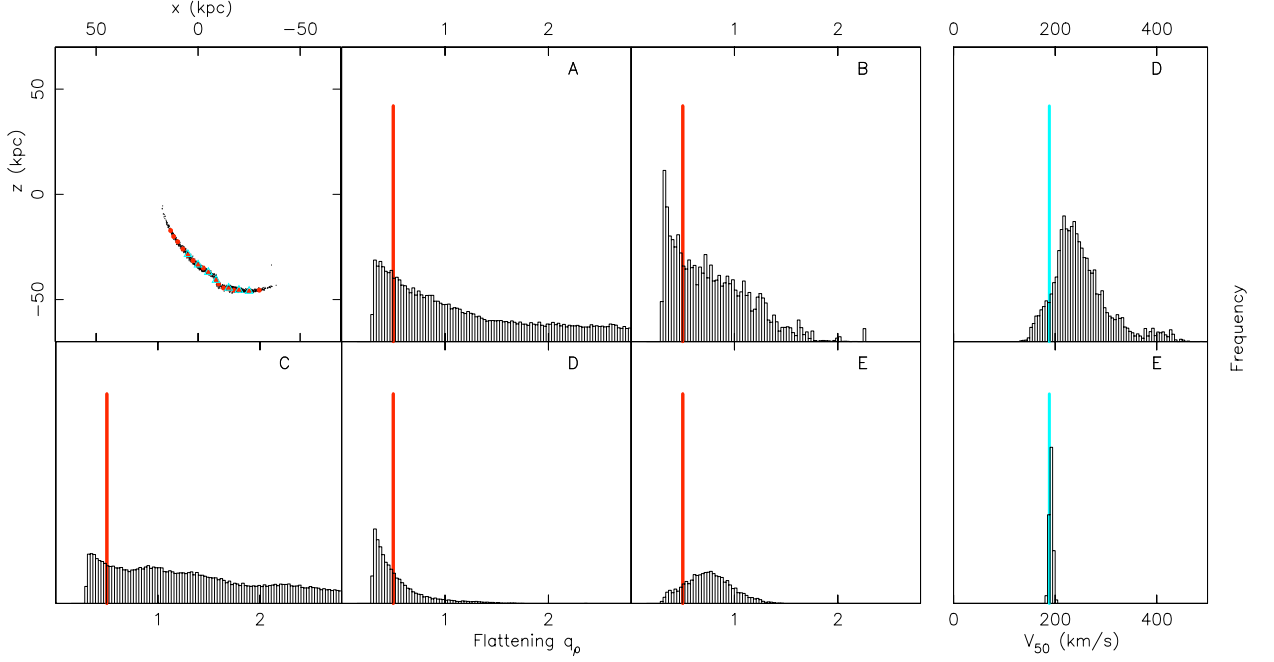
Figure 3.18: As Fig. 3.17, but for a Palomar 5-like stream with no turning point.

the trajectory of a stream star can be integrated with its initial position offset from a certain point in the progenitor's past orbit by a certain distance r_{cutoff}, offset outwards for trailing tail stars and inwards for leading tail stars. This is shown diagrammatically in Figure 3.8. Starting at the current position and velocity of the progenitor P, its orbit is integrated backwards in time, marked by the grey dots. For any point on its backward orbit, Q, at time t_Q, the inner and outer escape points are approximated as $r_Q - r_{cutoff}$ and $r_Q + r_{cutoff}$, indicated respectively by the blue and red dots at Q. These provide the initial positions for the orbits of stars that escape the satellite at Q. For their initial velocity components, we use the velocity of the progenitor orbit at Q. With these initial phase space coordinates, we integrate forward for the same amount of time t_Q. These orbits are indicated by the blue and red dotted curves, with their final points on the leading and trailing tails at A and B respectively. Repeating this process for several points on the backward integrated orbit (say, for every 50 Myr) yields a set of points which lie closely on the tidal tails of the stream (red and blue dots in Figure 3.9), which we shall refer to as the corrected

points for a given set of parameters.

We find empirically that the offset radius for a point Q at a radial distance r can be calculated approximately as 2.88 times the theoretical Jacobi radius:

$$r_{cutoff} = 2.88 \times \left(\frac{m_{sat}}{3\widetilde{M}(r)} \right)^{1/3} r \,, \tag{3.10}$$

where m_{sat} is the mass of the satellite and $\widetilde{M}(r)$ is calculated from the circular velocity V_c of the host galaxy at r as $\widetilde{M}(r) = rV_c^2(r)/G$, where G is the gravitational constant. For a perfectly spherical potential, $\widetilde{M}(r)$ is equivalent to the mass contained within radius r. For non-spherical potentials, it is only a crude approximation to the total mass inside r, but as we show below, the correction we obtain using r_{cutoff} calculated in this manner is sufficiently accurate for our purposes.

We find that by fitting the stream data with these corrected points it is indeed possible to recover the parameters of the potential as well as the orbit. It is interesting to note that through this correction mechanism, one has more information on the progenitor's past orbit than one would have with only the local orbit of the progenitor (i.e. the red and blue dotted curves in Figure 3.9 contain more information than the grey curve does). In this sense, the tidal stream retains some memory of its infall. It is important to note that although we do not correct for velocities at the escape points, the velocities of the corrected points also lie along the velocities of the tidal tails as seen in Figure 3.9, i.e. the correction is valid in all of phase space. This is true of all the streams we tested, possibly because we use low mass satellites. If a similar correction mechanism is used for extending the present technique to more massive streams, we expect that a corresponding correction in velocity space would be required.

The backward integration time depends on the age of the stream and is usually unknown. It is also assumed in the present discussion that the progenitor is identifiable and its position on the sky is known, but more often than not, the satellite is completely disrupted or obscured and it is impossible to identify the progenitor (for example, the NGC 5907 and the Monoceros streams). The time for backward

integration can be found empirically, running different fitting routines with different backward integration times for the correction (it only need be accurate to around 1 Gyr). Similarly, several fitting routines can be tried assuming the unidentified progenitor to be at different positions along the stream. However, in all the tests described in this paper, the progenitor, its initial mass and backward integration time, were taken to be known quantities.

Figure 3.10 shows nine streams on which this stream-fitting method was tested (note that we are now fitting streams, not orbits as in §3.4). These were generated with *gyrfalc(ON)*, an N-body integrator based on a fast and momentum conserving tree-code (Dehnen 2000, 2002), as implemented in the stellar dynamics toolbox NEMO (Teuben, 1995). For the host galaxy, realistic models were used that comprised a spheroidal halo, a spheroidal bulge, and exponential disks (thick disk, thin disk and ISM) similar to the ones described in Dehnen and Binney (1998) for the Milky Way. Except for the flattening of the halo, the model of the host galaxy for each case is one of the two models described in Table 3.2. The halo flattening and the initial conditions of the orbits of the satellites for each stream along with its integration time are listed in Table 3.3. Spherical King models of 100,000 particles were used for the N-body satellite simulations. See Table 3.3 for the masses, tidal radii and central potentials of these. We have limited the present study to satellite masses in the range of 5.0×10^6 to $1.0 \times 10^8 \, M_\odot$, as they seemed to be ideal candidates for this technique rather than more massive and heavily disrupted satellites, for which dynamical friction plays a significant role. For the integration with *gyrfalc(ON)*, a Plummer softening kernel, along with a softening length of $0.03 \, \text{kpc}$, and an opening angle tolerance parameter of 0.6 (the default) were used.

We make extensive use of the work of Dehnen and Binney (1998) for the calculation of the potential, especially for the bulge and disk components. We assume that these baryonic components of the system are well understood and their contribution to the potential is kept fixed, so that the only parameters to be estimated are those of the dark halo. As the streams are distant, the precise details of the inner mass distribution are not critical and the estimates are not affected by small variations in

the baryonic component. The potential due to the trial density distribution of the halo is calculated using multipole expansion. The calculated halo potential and its first derivatives (w.r.t $\ln r$ and $|z/r|$) are stored on a grid in $\ln r$ and $|z/r|$. Adding to these, the potential and accelerations due to the bulge and the disk using GalPot, we have the total potential and acceleration at each of the grid points. The acceleration at any point is obtained by interpolating with a 2-dimensional, fifth-order spline.

In the following sections, we describe the results of fitting the streams with different kinds of information.

3.5.1 With projected positions alone

In this section, we discuss how well the various parameters of the halo are constrained by fitting only the projection of streams on the sky, as this is the only information that is usually available for very distant systems. Figure 3.11 shows the distributions of the density flattening q_ρ obtained by fitting the pseudo-streams with corrections to trial orbits described in the previous section. The number of attempted orbits in the fitting routines are in the range of $500,000$ to $1,000,000$, running the fitting algorithm until the chains are well mixed and reasonable fits of the test streams are found. As can be seen, the estimates fall within reasonable ranges of the true values of q_ρ (indicated by the red lines), but the accuracy of the estimates vary from case to case. The differences in the accuracies arise from the differences in the streams themselves, as some configurations are more degenerate, in that many parameter choices can reproduce the same observations. However, even in the poor cases, the estimated q_ρ still provides a useful indicator of the shape of the halo. For example, for stream I, made in a prolate halo of $q_\rho = 2.0$, there are two peaks in the distribution, the true value of q_ρ being at the smaller peak. The trial streams that are generated at both the peak values of q_ρ resemble the given stream, but streams generated at the smaller peak (with $q_\rho = 2.0$) show extra features such as small bifurcations that are similar to the ones seen in stream I, whereas streams generated at the larger peak (with $q_\rho \approx 1.6$) do not show these. Thus, the streams at $q_\rho = 2.0$ resemble the test stream in its finer details. These smaller features were not included in the fitting as we

deemed them difficult to observe, especially in distant systems, but if observed, they could be used to obtain better estimates or distinguish between multiple solutions. Nonetheless, the distribution in q_ρ for stream I is limited to the prolate region and the corresponding distribution in the potential flattening q_ϕ is narrower (approximately, $q_\rho = 1.6 \equiv q_\phi = 1.2$ and $q_\rho = 2.0 \equiv q_\phi = 1.33$, using equation 3.9). It should be noted that for streams B and E, the true value of the inner slope γ of the halo is approximately 1.28, but they were fitted in a model with a fixed $\gamma = 1.0$. This was primarily undertaken to check if the difference in the inner slope affects the estimation of q_ρ, and it does not, confirming our assumption that these streams are insensitive to the finer details of the inner matter distribution. On the other hand, for fitting stream H, we set the inner power slope γ to be a free parameter, with lower and upper bounds at -1 and 2.0. This does not seem to deteriorate the estimate of q_ρ as was initially expected, so γ can be set to be a free parameter in the application of the technique to real stellar streams. However, γ itself is not found to be constrained by fitting the projections of these streams.

Another significant parameter of the halo is its mass, which determines the circular velocities at large radii. In order to see how well our technique estimates this quantity, we plot the distribution of the circular velocity at $50\,\mathrm{kpc}$, V_{50}, shown in Figure 3.12, calculated from the potential parameters at each step of the coldest MCMC chain. As seen in the case for logarithmic orbits, these distributions are degenerate and it is not possible to constrain the halo mass with only positional information of a stream. We find that the remaining parameters of the halo, i.e. the outer slope β, the central density ρ_0 and the scale radius r_0 can have different values for the same value of the flattening q_ρ to produce streams that look identical in projection. The distributions of these parameters are degenerate (as shown in Figure 3.13 for β) and the projection of a stream alone cannot constrain them. The combination of these parameters result in different circular velocities, making the distribution of V_{50} degenerate.

As for the orbital parameters, the line of sight distance y_0 of the progenitor from the center of the galaxy is well-constrained (although there may be a sign discrepancy, as was seen in the case of pure orbits), whereas the line of sight velocity or the

tangential velocity components of the progenitor cannot be recovered.

3.5.2 Adding circular velocities

For many spiral galaxies, inner rotational velocities are available (for instance from H I kinematics) or are feasible to measure with current instrumentation, which provides information on the inner mass profile of the galaxy. Figure 3.14 shows the effects of adding the rotational velocities (here assumed to extend up to $30\,\mathrm{kpc}$) to the projected positions for stream B (to take a particular example). Comparing the corresponding distributions for the stream in Figures 3.12 and 3.13, we see that there is a marked improvement in the estimate of the outer power slope β. This is, as explained in the previous section, due to the correlation of β and the circular velocity parameter V_{50}, the latter being estimated accurately with the provision of the inner circular velocities. The peaks of the distributions in q_ρ in Figure 3.14 and Figure 3.11 are at similar positions, but the former is less smooth as a different proposal step size was used to fit the stream in this case. Though not shown here, the degeneracies in the scale radius r_0 and the central density ρ_0 are also removed and we obtain accurate estimates of these parameters. Moreover, distance to the progenitor and its velocities can also be constrained when the rotational curve is added to the fitting data. As seen in the distance parameter, there may be a sign discrepancy in the estimate of the line of sight velocity v_{y_0} of the progenitor, but not in the estimates of its tangential velocity components.

3.5.3 Adding line of sight velocities

Using stream G as an example, we illustrate the effects of adding kinematic data to the projected geometry of the stream (but without circular velocities) on the estimates of q_ρ and V_{50}. Figure 3.15 shows the q_ρ distributions in each case in the top panels and the V_{50} distributions in the bottom panels. In (a), only the projected positions of stream G on the XZ plane are used in the fitting routine. In addition to these, the line of sight velocity of the progenitor is provided to obtain the distributions for (b).

To make the distributions in (c), we added more line of sight velocities (at five points along each tail, within $20\,\mathrm{kpc}$ from the progenitor). This shows that by providing velocity information it is possible to estimate V_{50} or the mass of the halo. The added information also improves the estimate on q_ρ. As in the case where we provided the rotation curve, the progenitor's velocity components and its line of sight distance are well constrained.

3.5.4 Fitting in a logarithmic potential

We also investigated how well the test streams in Figure 3.10 (simulated within a full multi-component galaxy model) can be fit with a simple axisymmetric logarithmic halo with no stellar components. Figure 3.16 shows the distribution in q_ϕ thus obtained. The green lines indicate the potential flattening q_ϕ that correspond to the input density flattening q_ρ values. We find that the estimates are remarkably accurate. This exercise suggests that a logarithmic halo can be used as a good approximation to the more complex input axisymmetric model, at least in order to constrain the flattening of the halo.

3.5.5 Shorter streams

We have seen in §3.4.1 that the estimation of parameters is sensitive to the number of turning points of the orbit. To explore this aspect of the problem for streams, we consider stream B at much earlier stages of its infall, where its tidal tails are substantially shorter. In Figure 3.17, it is at 5 Gyr into its infall and the tidal arms form a parabolic curve, much like the structure observed to the north west of M31 (Carlberg et al., 2011). In Figure 3.18, it is at 2 Gyr in its evolution and resembles the Palomar 5 stream (Odenkirchen et al. 2001). For both these cases, we consider five possible scenarios of available information. Case A is where we only have the projected positions of the streams on the sky. We see that the distributions of q_ρ are much more spread out than for stream B, the degeneracy being much more for the Palomar 5-like stream. For Case B, the line of sight velocities at certain points (red squares) are also

provided for the fit. In Case C, we assume that no kinematic data is available, but the distance to the progenitor is known. It is possible to measure this quantity for many nearby systems as well as in our own galaxy with the TRGB method. In Case D, the distance to the progenitor and line of sight (l.o.s) velocities are provided in addition to the projected positions. Case E has the maximum information, where the rotational velocity curve is also available along with all the information of Case D. This case has been included primarily to study the effect of circular velocity information on the estimation of q_ρ. The distributions shown have been drawn from 500,000 steps of the coldest Markov chain.

Here, only the estimates of q_ρ and V_{50} are presented. For the stream in Figure 3.17 with only one prominent turning point, the distributions of q_ρ are limited to the oblate region and peak at approximately the true value of q_ρ (red lines). This particular example of this class of streams suggests that the estimates of the flattening are much more accurate when kinematic data are available as in cases B, D and E, although the estimate is good even with only the projection of the stream. The rightmost panels show the distribution of V_{50} for cases D and E (the cyan lines mark the input value). Though not shown, it is not possible to constrain this quantity without any kinematic information, as was seen for the longer streams. However, the technique yields very good constraints on V_{50} when a few velocity data points or the inner rotational curve are added to the spatial projection of the stream, making it possible to estimate the mass and shape of the halo for systems where such information is available.

The short stream shown in Figure 3.18 has no noticeable turning point. Consequently, the distributions of q_ρ are broad and highly degenerate even when the distance to the progenitor or line of sight velocities are provided. It is only when both the progenitor distance and line of sight velocities along the stream are provided that the distribution peaks at approximately the right input value of the flattening. When the circular velocities are also added to the fitting, then the distribution looks more Gaussian-like and a better estimate of q_ρ is obtained. One has to bear in mind that the difference in the estimated and true values of the flattening in the potential is

expected to be much less than that of the flattening in the density distribution, since the distribution of the corresponding q_ϕ is narrower as per equation 3.9. As for the mass estimates, even with a stream as short as this, the constraints on V_{50} are good when sufficient information (as in case D) is available. Such short streams are mostly observed in systems very close to us, for which the rotational velocity curve, line of sight velocities and distance to the progenitor are available or can be easily measured. Therefore, they can be used as effective probes of the shapes and masses of nearby halos.

3.6   Discussion

We have shown that stellar streams found in halos of galaxies can be used to constrain parameters of the mass distribution, even without any kinematic information. The easiest potential parameter to estimate, and perhaps one of the most interesting, is the flattening of the distribution q_ρ. This is under the simplifying assumption that the halo is axisymmetric. In a future contribution, we will test the technique with triaxial halo models. Not surprisingly, our technique cannot constrain the mass of the halo (measured by the circular velocity at 50 kpc) without any kinematic information. However, by adding the rotational velocity curve or line of sight velocities of the stream stars, it is possible to estimate the total mass as well. According to the currently-held view of hierarchical galaxy formation, large galaxies are built up by the accretion (and disruption) of smaller satellite galaxies (White and Rees, 1978). If this is the case, one can expect to find remnants of the process in many galaxies and these will certainly be revealed by future deep surveys (E-ELT, JWST). By applying this technique to a large sample of galaxies, it would be possible to obtain statistics on the shapes of halos, which is crucial in understanding dark matter and galactic evolution. The method is immediately applicable to individual streams, the results of which have several implications. For one, they would provide a better description of the environment in which other phenomena occur. The properties of the halo can be used in studies involving satellite dynamics, tidal debris, gas distributions in the

outer regions of galaxies, lensing and many other areas of interest.

The method could also provide a consistency check for galaxies where the dark matter distribution or its shape has been measured by one of the techniques mentioned in §3.1. Tidal streams may also be used in testing alternative theories of gravity. For instance, if a prolate halo is found, it could eliminate MOND as a viable theory (Read and Moore 2005). In addition to the halo parameters, the technique also recovers the progenitor orbit, giving us a coarse estimate of the distance to the progenitor, and clues to its location if it is unknown, as well as distances and velocities along the stream.

The correction mechanism employed is one of the key aspects of the technique. It enables us to sample millions of models of the stream without having to resort to N-body simulations for each case, making the problem computationally tractable. During the developmental stages of this paper, we attempted to fit the tidal tails with orbits alone and this sometimes resulted in wrong estimates or highly degenerate distributions of the flattening. Thus, the correction mechanism plays an important role in the effectiveness of the method and the accuracy of the estimates obtained. For its simplicity, it reproduces the stream for an orbit remarkably well, even recreating the bifurcations and other features seen in the stream simulations. The only drawback is that one requires the mass of the in-falling satellite to calculate the corrected points, an approximate value of which can be obtained from star counts or integrating the light along the stream.

Our correction mechanism has only been tested with spherical, non-rotating King satellites. It is unclear how well it will work for disk-like or other types of satellites, but it should be possible to obtain a correction mechanism for these based on the same principles. However, this means that the results for an observed stream would depend on the assumptions made about its progenitor. For low mass streams such as the ones discussed in this paper, it is safe to assume that the progenitor is a globular cluster or dwarf spheroidal galaxy. Nevertheless, it would be useful to check the correction mechanism with other models of the satellite to see how sensitive it is to the input satellite properties.

In light of all these assumptions, the technique in its present form is applicable to cold, low-mass streams ($M \leq 1.0 \times 10^8 \, \mathrm{M_\odot}$), for which dynamical friction can be neglected. Observationally, stellar streams fall into two major categories: the ones that are closer to us, in which the positions and velocities of individual stars can be measured and the ones that are farther away and detected in surface brightness. For the latter, the kinematics are usually not measurable. In rare cases, globular clusters associated with the stream may be observed and their velocities can be used as additional information (Mackey et al., 2010). Among the streams that are closer to us, are short structures like the Palomar 5 stream. For these, a large number of radial velocity measurements can be made, and these streams can be used to constrain the parameters of the host halo, despite having no turning points. Another plausible scenario is where two or more streams are observed in the same galaxy. Fitting them simultaneously would provide constraints on the halo, even if the individual streams are relatively short. Multiple streams in a halo provide a possible means of probing the halo shape through different cross sections of the halo, which would also enable us to check for triaxiality of the halo.

A surprising result we found, that can serve as a powerful diagnostic tool in the application of the method to real systems, is that if the streams (generated in a host potential with a double power law halo with a bulge and a disk) are fit in an axisymmetric logarithmic potential, the flattening of the potential can still be well estimated. This is encouraging as it suggests that while extending the method for triaxial models, one could use a triaxial logarithmic potential for preliminary estimates on the axial flattenings, which is much easier to use than triaxial density distributions. In addition to the logarithmic and double power law models described in this paper, we also experimented with non-parametric density models for the halo, in which the matter distribution was defined by the values of densities at different radii. Preliminary tests showed that these parameters are difficult to constrain, but this may yet be improved upon.

3.7   Conclusions

We have extended the idea of using tidal streams to estimate the shape of the dark halos they reside in. The major challenge was that for most streams, only their projected positions are available. This has been a hindrance in using these streams effectively as there may be streams with similar projections for different profiles. We overcome this difficulty by adopting a statistical approach. We sample various orbits with different orbital and potential parameters using parallel MCMC chains. The output distribution of the flattening parameter that we obtain from these peak at the right value, if the information is sufficient. We first tested the method on orbits in a logarithmic potential and then on streams made with N-body simulations in more realistic galactic potentials (sum of disk, ISM, bulge and spheroidal halo). Another major aspect by which the technique differs from earlier work is that the stream in question is not treated as an orbit, but derived as a correction to the orbit of its progenitor.

We have demonstrated that there are cases in which it is possible to get constraints on the shape of the dark halo using only the projection of a tidal stream on the sky, the accuracy of which varies from stream to stream. The method is sensitive to the number of turning points of a stream and only works when there are at least two turning points. With more turning points, the accuracy of the estimate increases. If the stream is only a parabola or turns out to be degenerate even with a few turning points, the estimate may be improved by adding more information such as the line of sight velocities or the distances along the stream if they are available. In our tests with simulated streams, we did not find cases where the fitting procedure yielded significantly incorrect estimates of the input halo flattening (though of course with insufficient information there are degenerate solutions). Exhaustive testing is required to confirm that this is always the case. In all our tests, we used low mass satellites ($M \leq 1.0 \times 10^8 \, M_\odot$). This method cannot be applied in its current form to heavy and highly disrupted streams such as the Giant Stellar stream around M31 (Ibata et al. 2001a). However, it may be possible to further extend the technique to such massive satellites by accounting for dynamical friction as an additional correction.

We find that the line of sight distance of the progenitor from the center of the host galaxy is well-estimated (at times, with a sign discrepancy) when only the projection of the stream on the sky is available. The other orbital parameters, i.e. the velocity components of the progenitor are also well-estimated, but only when kinematic information, in the form of line of sight velocities along the stream or the H I rotational curve, are provided.

We also fit the streams generated in a spheroidal density model of the halo with orbits in a logarithmic potential. We see that despite using a simpler model, we are able to get a good estimate on the flattening of the halo. In the tests with the orbits in a logarithmic potential, we see that the initial distance y_0 is also constrained very well, but not the circular velocity. This is as expected; even for a circular orbit in a Keplerian potential, it is not possible to deduce the central mass from the radius of the orbit alone. The method cannot be used to constrain the inner slope of a spheroidal halo as the considered halo streams are too distant to probe the inner mass distribution using only the projection of the stream. It is encouraging to note that with circular velocities and the projection of the stream, most of the parameters of the halo can be recovered, as such information is available or easily acquirable for several systems. This technique is readily applicable to many of the streams observed in the near universe such as the low mass streams around M31, NGC 5907, NGC 891 and the Sagittarius stream in our galaxy.

Acknowledgments

Table 3.2: Models used in simulations: The parameters of the halo except its flattening, and the baryonic components of the host galaxy in which the streams are generated, along with their units are given. $\rho_0, r_0, q_\rho, \gamma, \beta$ and r_t are the central density, scale radius, density flattening, inner power slope, outer power slope and truncation radius of the spheroidal components (the bulge and the halo). The parameters of the disk components are the central surface density Σ_d, the scalelength R_d, the scaleheight z_d and the central depression parameter R_m (which is 0 for the thin and thick disks).

Component	Parameter	Model 1 Streams A, D, G, C, F, I	Model 2 Streams B, E, H
Halo	ρ_0 ($M_\odot pc^{-3}$)	0.11013117	2.7986274
	r_0 (kpc)	5.23553	1.0
	γ	1.0	1.28
	β	3.0	2.34
	r_t (kpc)	1000	1000
Bulge	ρ_0 ($M_\odot pc^{-3}$)	0.65074246	0.3
	r_0 (kpc)	1.0	1.0
	q_ρ	0.6	0.6
	γ	1.8	1.8
	β	1.8	1.8
	r_t (kpc)	1.9	1.9
Thin Disk	Σ_d ($M_\odot pc^{-2}$)	412.0	341.0
	R_d (kpc)	3.2	3.2
	z_d (kpc)	0.18	0.18
ISM	Σ_d ($M_\odot pc^{-2}$)	69.5	57.5
	R_d (kpc)	6.4	6.4
	z_d (kpc)	0.04	0.04
	R_m (kpc)	4.0	4.0
Thick Disk	Σ_d ($M_\odot pc^{-2}$)	29.5	24.4
	R_d (kpc)	3.2	3.2
	z_d (kpc)	1.0	1.0

Table 3.3: Test Streams: Orbital Parameters, Halo Flattening and Age. x_0, y_0, z_0 are the initial positions and $v_{x_0}, v_{y_0}, v_{z_0}$ the initial velocities of the orbits of the King model satellites of masses m_{sat}, tidal radii r_t and central potential $\Phi(0)/\sigma^2$. The density flattening of the halo q_ρ in each case is given in the first column. The ages given are the time since the starting of the simulation which gives the configurations of the streams that are used in the fitting.

Stream	q_ρ	x_0 (kpc)	y_0 (kpc)	z_0 (kpc)	v_{x_0} (km s^{-1})	v_{y_0} (km s^{-1})	v_{z_0} (km s^{-1})	Age (Gyr)	m_{sat} ($\times 10^7$ M$_\odot$)	r_t (kpc)	$\Phi(0)/\sigma^2$
A	0.8	30.0	15.0	38.0	-110.0	60.0	-90.0	7.0	0.5	0.8	4.0
B	0.5	35.0	5.0	35.0	-100.0	5.0	80.0	8.0	0.5	0.8	4.0
C	1.6	35.0	20.0	30.0	-90.0	80.0	140.0	9.0	0.5	0.8	4.0
D	1.0	35.0	10.0	35.0	-120.0	30.0	100.0	10.0	5.0	1.2	4.0
E	0.3	35.0	5.0	35.0	-100.0	5.0	80.0	5.0	5.0	1.5	4.0
F	1.8	35.0	10.0	35.0	-120.0	30.0	100.0	4.0	5.0	1.2	4.0
G	1.0	25.0	20.0	20.0	-120.0	90.0	140.0	8.0	10.0	1.7	7.0
H	0.5	35.0	5.0	35.0	-100.0	5.0	80.0	8.0	10.0	1.1	2.75
I	2.0	30.0	0.0	0.0	180.0	160.0	130.0	7.0	10.0	0.9	3.0

Chapter 4

The Stellar Stream of NGC 5907

4.1 Introduction

Streams of stars that are the relics of minor merger events have been discovered around several spiral galaxies, starting with the Sagittarius stream in our very own Milky Way (Ibata et al., 2001b; Majewski et al., 2003). These kinematically cold and thin streams act as excellent tracers of the dark matter halo, as they approximately delineate the orbit of the in-falling satellite galaxy. In Chapter 3, we demonstrated how it is possible to use these streams as effective probes of the morphology of the dark matter halos of the host galaxy. In this chapter, we apply the technique developed to study the dark halo of NGC 5907. It is to be noted that due to time constraints, the results presented here are only preliminary, and the estimates are as yet not conclusive.

NGC 5907 is a thin Sc spiral galaxy at a distance of 13.4 Mpc (Tully et al., 2009), which with an inclination of $87°$, is almost edge-on. Despite the warp noticed in its disk, it was long considered to be an isolated normal galaxy. This view changed when Sackett et al. (1994a) discovered a faint low-surface brightness halo around it, the presence of which was further confirmed by others in various bands (Morrison et al., 1995; Lequeux et al., 1996; James and Casali, 1998; Rudy et al., 1996), suggesting the presence of a peculiar red "halo" stellar population. The new interest in the halo of NGC 5907 finally led to the discovery of a polar ring structure, of stellar origin, in its

halo by Shang et al. (1998). The stellar ring and faint halo were both attributed to the cannibalization of a low mass galaxy by NGC 5907. As explained by the discoverers of the ring structure, the alternative origins of the ring as Galactic cirrus, planetary nebula or supernova remnant can be ruled out by photometric considerations. These authors also observed a dwarf companion PGC 54419 at a projected distance of 36.9 kpc, which was initially suspected to be associated with the stellar ring or the warp. Independent analyses of the polar ring by Reshetnikov and Sotnikova 2000 and Johnston et al. (2001) provided some limits on the mass of the halo and age of the structure. The former used N-body simulations to reproduce a structure similar to the one observed by the disruption of a low-mass dwarf companion (both spheroidal and disk-like). They estimated a mass to light ratio in the range $\Upsilon \sim 3 - 4$ and the age of disruption to be less than 1.4 Gyr. The latter authors used geometrical considerations applied to a part of the ring (the one with the least observational uncertainties) to arrive at similar estimates, $\Upsilon \sim 3$, with the age between 0.8 and 2.4 Gyr and the mass of the progenitor as $2 \times 10^8 \, \mathrm{M_\odot}$.

More recently, a pilot survey by Martínez-Delgado et al. (2008) (hereafter MD08) showed the stellar ring to be part of an exquisite stream-like structure wrapped around NGC 5907, the image of which is shown in Figure 4.1. An independent confirmation image of the structure was also obtained by amateur astronomers Binnewies and Popsel in 2008[1]. We use the image of the stellar stream presented in MD08 in an attempt to constrain the parameters of the halo of NGC 5907. We also use the work of these authors as a guideline for our study of the stream, and to compare our results against. In Section 2, we discuss the observational data and certain problems specific to the NGC 5907 stream. It also includes a description of the baryonic models used in our fitting. The fitting routine is discussed briefly in Section 3, as some significant improvements have been made in the algorithm. Preliminary results of fitting the stream in a double spheroidal density model for the halo, as well as in a MOND scenario are presented in Section 4. We conclude with a discussion of our results and further work required to fully explore the information of the halo we can obtain from

---

[1] http://www.capella-observatory.com/ImageHTMLs/Galaxies/NGC5907Prim.htm

the stream.

4.2 The Stellar Stream

The optical image of NGC 5907 in MD08 was obtained by stacking multiple deep exposures in several bands. One of the main limitations in studies of faint surface brightness structures is the uncertainty in the background subtraction (due mainly to scattered light). To correct for this, MD08 subtracted out a locally-smooth background from their image, and it should be kept in mind that this is a somewhat subjective procedure. Clearly structures larger than the smoothing length will be erased and false detections can be created, depending on the choice of the algorithm that is used. The confirmation by Binnewies and Popsel cited above lends confidence that the main structures shown in Figure 4.1 are real. We noticed that the amateur camera employed by MD08 suffers extremely strong optical distortion; we corrected for this effect by identifying reference stars in their stacked image, and used a high-order polynomial fit to resample the data onto a tangent-point projection. The resulting corrected image is shown in Figure 4.2, where we have additionally masked out all regions containing point-source detections above a 3-sigma threshold, and applied a further mask to excise the bright disk of the galaxy as well as all regions not obviously containing the stream structure. It is this data we will use for the fitting.

The NGC 5907 stream consists primarily of two elliptical loops which intersect each other several times, making the exact path of the stellar stream highly unclear. In order to refer to the different sections of the stream, we use the marked image of MD08, shown in Figure 4.3. As can be seen, it is not clear whether the south eastern (SE) loop is contiguous with the western W1 arc or the south-western SW tail. Even though the uncertainties in the path of the stream causes significant degeneracy, it is possible to fit the stream by making the fitting routine independent of the path taken.

An important piece of information that is missing for the NGC 5907 stream is the location of its progenitor, which is either completely disrupted or obscured. MD08

Figure 4.1: From Martínez-Delgado et al. (2008): Image of NGC 5907, obtained with the BBRO 0.5-meter telescope, using multiple exposures of different filters for a total exposure time of 11.35 hours. It is to be noted that the linear feature seen in the lower left corner is spurious.
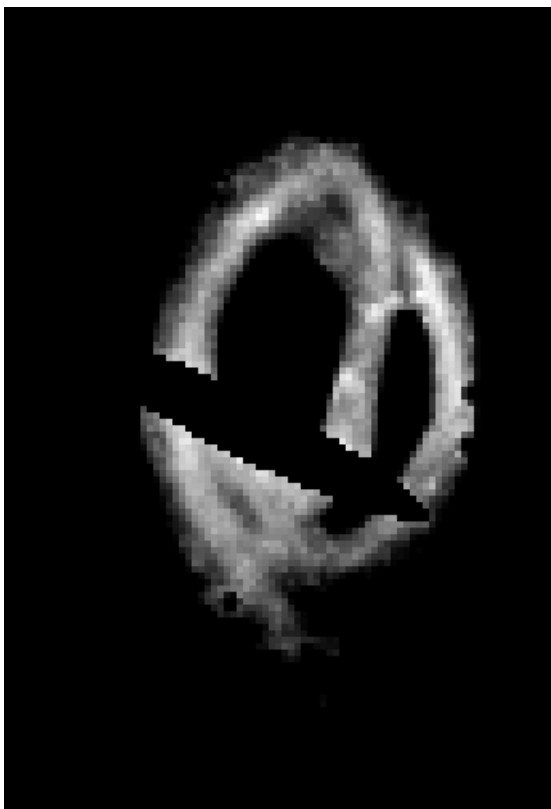
Figure 4.2: Tangent-plane resampling (1 kpc × 1 kpc pixels) image of the MD08 image of NGC 5907. We have masked out the disk of the host galaxy, as well as point sources and regions devoid of the stream structure. This is the image of the stream that is used in the maximum-likelihood fitting.

suggested that it may be hidden by the galaxy disk in its western edge, where the stream crosses it. By running a few fitting tests with different progenitor positions along the stream and by considering the symmetry of the stream, we find this suggestion to be plausible. Hence, for the preliminary tests, we have fixed the projected progenitor position at this location. However, it would be ideal in a thorough study of the stream to let this be a free parameter in the MCMC sampling. Other consequential unknown parameters are the age of the stream and the mass of the progenitor, both of which we set to be free in the fitting routine.

Several rotational velocity curves for NGC 5907 have been published (Casertano, 1983; Sancisi and van Albada, 1987; Sofue, 1996). In this Chapter, we use the HI rotation curve of Sancisi and van Albada (1987) along with the stream data to constrain the density distribution of the dark matter halo.

The parameter space explored includes only those of the dark matter distribution of the galaxy. Its baryonic component is kept fixed for the orbit intergration. The luminous component of NGC 5907 consists mainly of a disk, with a small bulge. We obtained the mass model of the disk and bulge of NGC 5907 by fitting 2MASS galaxy atlas images using "GALFIT" (Peng et al., 2002), a tool which decomposes an observed galaxy image into a sum of structural models. The disk component was thus estimated to have a central surface brightness of $15.93 \pm 0.00 \, \mathrm{mag \, arcsec^{-2}}$, disk scale height of $9.00 \pm 0.01 \, \mathrm{arcsec}$ and disk scale length of $62.50 \pm 0.11 \mathrm{arcsec}$. These structural parameters were used to construct a mass model for the galaxy, using the multipole expansion technique discussed in Chapter 3, with the constraint that the model rotation curve should fit the inner HI rotation curve of Sancisi and van Albada (1987), and give components that are similar to those of the Milky Way. The resulting model has a stellar disk, gas and bulge with masses of $4.7 \times 10^{10} \, \mathrm{M_\odot}$, $1.8 \times 10^{10} \, \mathrm{M_\odot}$, $0.9 \times 10^{10} \, \mathrm{M_\odot}$ respectively. We have yet to attempt fitting the stream with other mass models of NGC 5907 (e.g. Just et al. 2006).
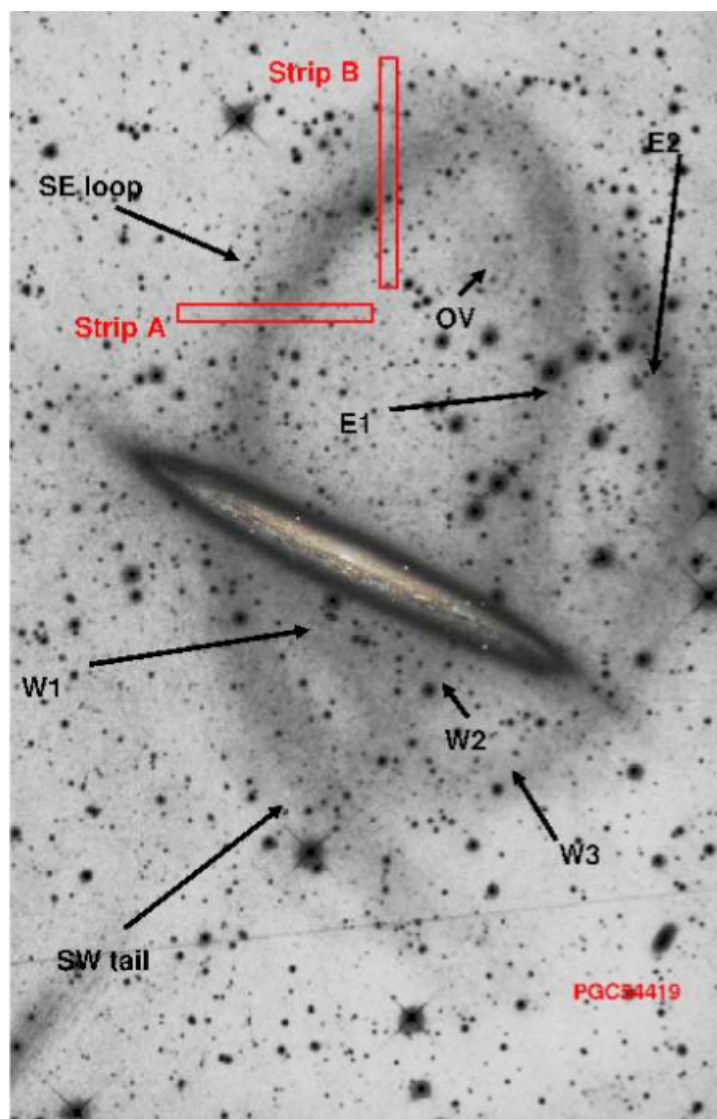
Figure 4.3: Taken from Martínez-Delgado et al. (2008): Image of NGC 5907 with the different stream features marked. A colour image of the disk has been superimposed.

4.3   Fitting the Stream

4.3.1   Modifications to the Fitting Algorithm

Later tests of the fitting algorithm described in Chapter 3 indicated that it takes a long time to reach convergence. This is mostly due to the large differences in the scales of the parameters. Therefore, the MCMC fitting was modified to have 100 sets of parallel chains to sample the parameter space instead of only one set. The interactions of the different sets of chains are such that it makes the sampling independent of the scales of the parameters. The approach is known as "affine-invariant ensemble sampling" (Goodman and Weare, 2009). For a simple understanding of the concept, let us consider the case of single Markov chains (i.e. without Parallel Tempering). In this case, the ensemble consists of 100 MCMCs, which we refer to as walkers, which start at different points of the parameter space and whose path through the parameter space are dependent on the other chains. In the fitting routine used in the previous chapter and tests with mock streams, the sizes of the proposal steps for the various parameters during the sampling were kept fixed, which rendered the sampling slow and caused the acceptance rate of proposed steps to be low. In affine-invariant sampling, the size of the proposal step is adapted according to the scatter of the population. The proposal step size for a walker at a given time is taken to be proportional to the distance between two other random walkers in the ensemble. We incorporate Parallel Tempering into this approach by introducing higher temperature chains for each of the walkers in the ensemble, as described in Chapter 3. The swaps between chains are considered and made separately for each walker. We also ensured that the sampling reached a satisfactory acceptance rate of over 25%.

4.3.2   Preliminary Results

We discuss below the preliminary results we obtained by the fitting the projection of the stream in both spheroidal and logarithmic halos, as well as in a potential produced in a Modified Newtonian framework (MOND) by the baryonic components. The likelihood of a trial stream was calculated by creating model images of the stream

and comparing these to the observations. The corrected points obtained from a trial orbit using the mechanism described in Chapter 3 are smeared out to mimic an image of a real stream, which can then be used for a pixel-by-pixel comparison with the image of the NGC 5907 stream. The total likelihood is the sum of the χ^2 provided by the image comparison and the fit to the rotational velocity data.

Since the age of the stream is unknown and an approximate value of the same is required to use the correction mechanism effectively, we adopt the following approach: For any given trial orbit, the stream resulting from it at different ages are considered, out of which the one with the highest likelihood is taken to be the trial stream corresponding to those trial parameters.

Fitting in a Double Spheroidal Halo with Baryonic Components

The results presented here are those of an initial fitting of the stream in a realistic multicomponent galaxy model with a double spheroidal halo, in addition to the fixed spheroidal bulge and exponential disk components. For this initial fit, all the parameters of the halo, including its inner slope γ, were set to be free parameters. A comparison of the best-fit stream and the observed stream is shown in Figure 4.4. The green curves show the corrected points obtained from the trial orbit. The red curves show the orbit of the progenitor. There is a remarkable coincidence of the trial stream and the data, but since the method is based on a sampling approach, it is necessary to carry out an extensive study of the parameter space in order to achieve a high confidence on estimated values. The sampling yielded a reasonable fit to the rotation curve. Figure 4.5 shows the rotational curve obtained for the best fitting model (green dots) and the input curve (red dots). The distribution of the flattening in density q_ρ is shown in the left panel of Figure 4.6, which seems to show a peak in the prolate region. The values of flattening corresponding to the maximum likelihood is in the range $q_\rho \sim 2.0 - 2.1$. The middle and right panel of Figure 4.6 show the distributions of the initial radial distance y_0 and the outer slope of the density profile β, which peak at about $26.0\,\mathrm{kpc}$ and 2.1 respectively. The distributions of the central density ρ_0, the scale radius r_0 and the inner power slope γ are plot-
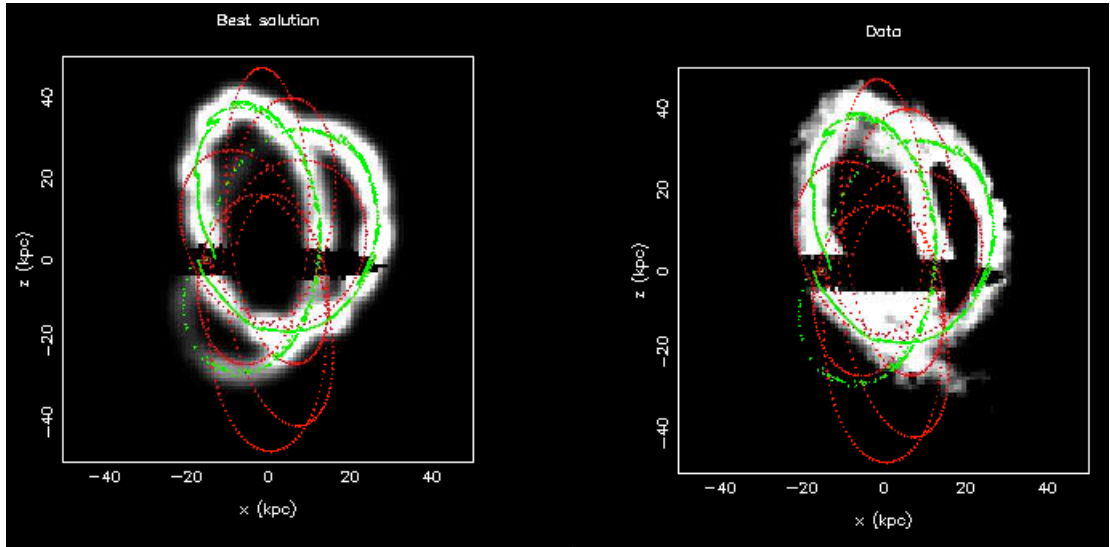
Figure 4.4: A comparison of the best fitting stream (left) and the data (right). In the left panel, the red curve shows the backward integrated orbit of the progenitor, from which the green curves that represent the corresponding stellar stream can be derived with the correction mechanism described in Chapter 3. The green curves are smeared out to obtain an expected image (in white) of the trial stream. The red and green curves in the right panel are the same as in the left, and have been overlaid on the observed stream image for comparison.
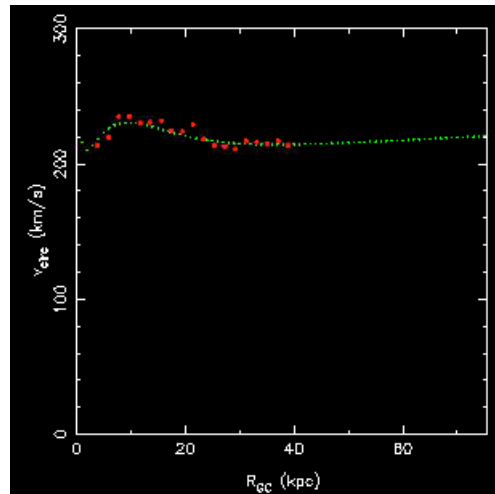
Figure 4.5: The rotational velocity curve of the best fit model. The observed HI rotational velocity data of Sancisi and van Albada (1987) is marked in red, and the rotational curve of the model in green.
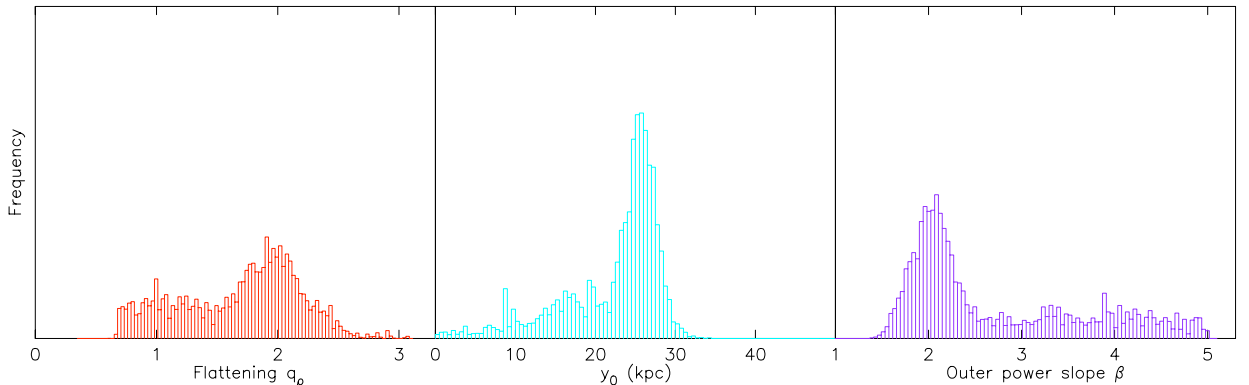
Figure 4.6: The MCMC distributions of the fitted parameters in a double spheroidal halo. From left to right: the flattening q_ρ, the progenitor line of sight depth y_0, and the halo outer power-law profile β.

ted in Figure 4.7 from left to right. The estimated values of these parameters are $\rho_0 \sim 2.0 \times 10^8 \, M_\odot/\text{pc}^3$, $r_0 \sim 2.0 \, \text{kpc}$, and $\gamma \sim 0.15$. Figure 4.8 shows the likelihood distributions of the initial orbital velocity components, whose maximum likelihood values are $v_{x_0} \sim -80.0 \, \text{km s}^{-1}$, $v_{y_0} \sim 130.0 \, \text{km s}^{-1}$, and $v_{z_0} \sim -170.0 \, \text{km s}^{-1}$. These distributions are drawn from 500,000 values of each parameter. It is encouraging to note that the distributions have distinct peaks and that they lie in physically reasonable ranges of the parameter values. However, further testing of convergence and narrow regions of the parameter space are required.

Fitting in a Spherical Halo

As a preliminary check of whether it is possible to reproduce the NGC 5907 stream in a strictly spherical halo, we fit the stream in a double spheroidal halo with a fixed flattening $q_\rho = 1$ and fixed baryonic components. The remaining parameters of the halo are set to be free. As can be seen in Figure 4.9, a close fit to the stream was found, although it is not as good as the fit found in the earlier section; in the right panel, the eastern arm of the observed stream and the trial stream (green curve) do not coincide. However, the sampling routine finds a reasonable fit to the rotational velocity curve as shown in Figure 4.10. The distributions of the various parameters of the halo and
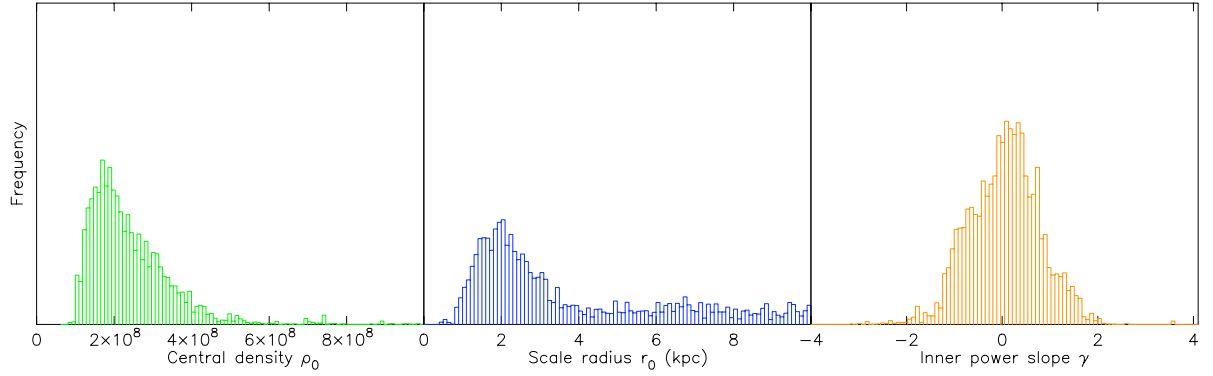
Figure 4.7: The MCMC distributions of the central density ρ_0, scale radius r_0, and inner power slope γ, obtained by fitting the stream in a double spheroidal halo.
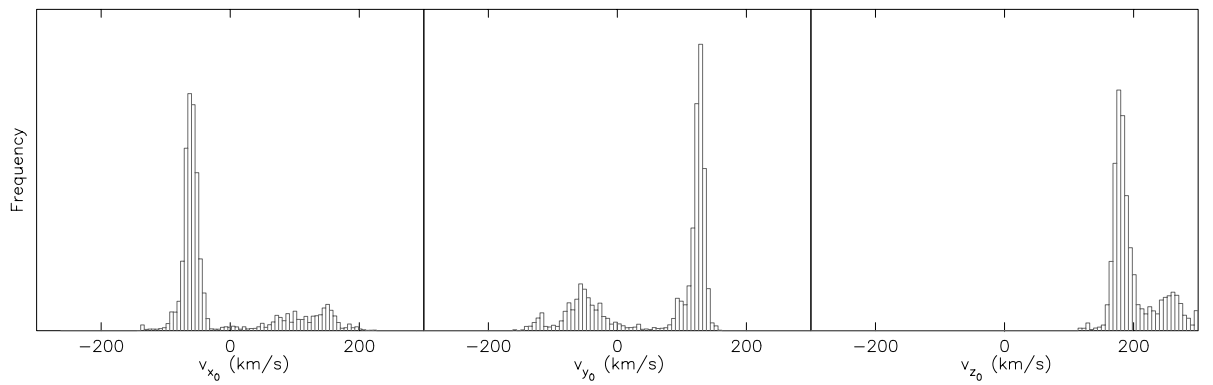
Figure 4.8: The MCMC distributions of the initial velocity components obtained by fitting the stream in a double spheroidal halo.
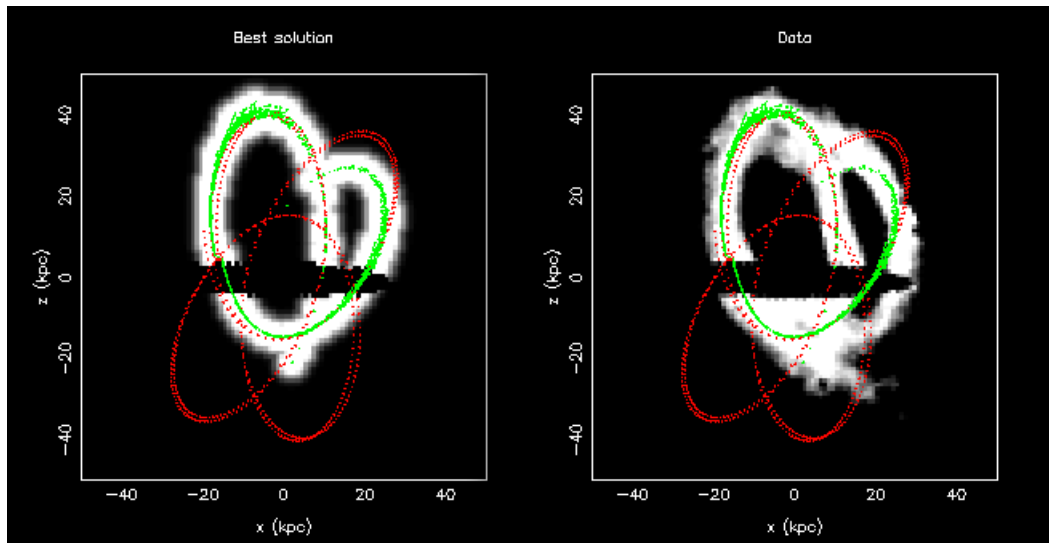
Figure 4.9: A comparison of the best fitting stream (left) and the data (right) in a spherical halo. In the left panel, the red curve shows the backward integrated orbit of the progenitor, from which the green curves that represent the corresponding stellar stream can be derived with the correction mechanism described in Chapter 3. The green curves are smeared out to obtain an expected image (in white) of the trial stream. The red and green curves in the right panel are the same as in the left, and have been overlaid on the observed stream image for comparison. As the right panel shows, the green trial stream lies along the observed stream, except at certain regions, for instance, along the eastern arm.
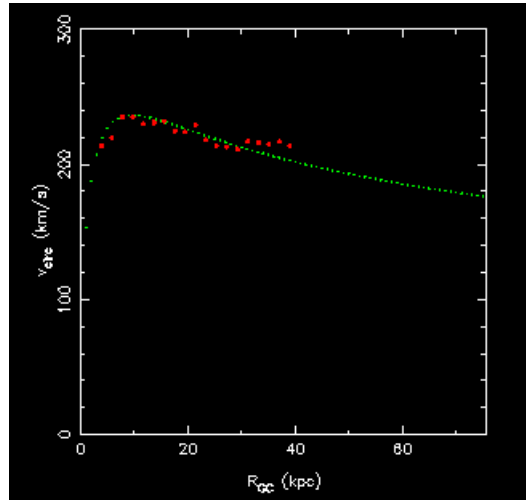
Figure 4.10: The rotational velocity curve of the best fit spherical halo model. The observed HI rotational velocity data of Sancisi and van Albada (1987) is marked in red, and the rotational curve of the model in green.
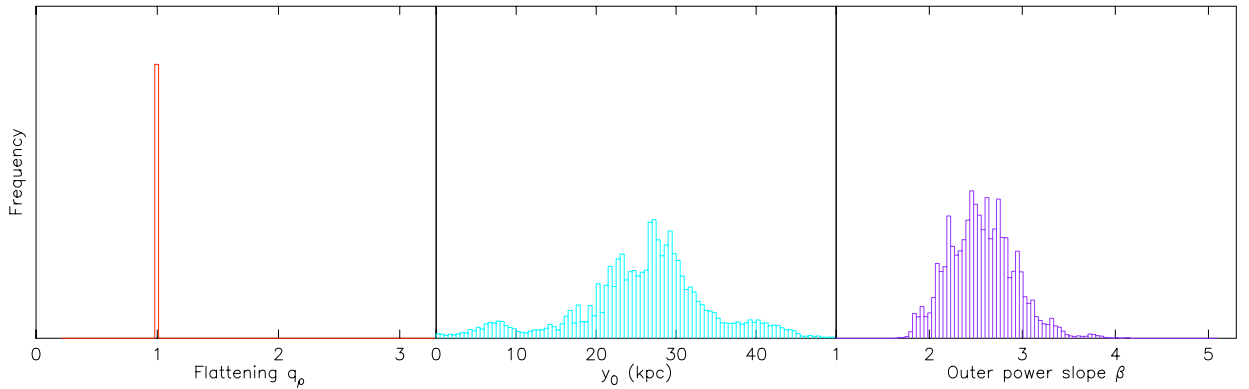
Figure 4.11: The MCMC distributions of the fitted parameters. From left to right: the flattening q_ρ, the progenitor line of sight depth y_0, and the halo outer power-law profile β, obtained by fitting the stream in a spherical halo (q_ρ was set to be fixed at 1.0).
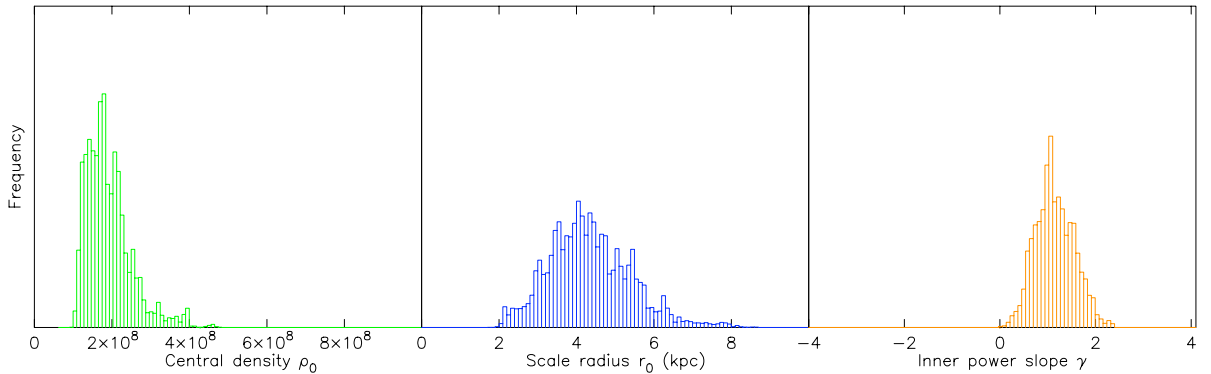
Figure 4.12: The MCMC distributions of the central density ρ_0, scale radius r_0, and inner power slope γ, obtained by fitting the stream in a spherical halo.

orbit of the progenitor are shown in Figure 4.11, 4.12, and 4.13. These distributions were drawn from 200,000 values of each parameter. Comparing with the previous fit (Figures 4.6, 4.7, and 4.8 respectively), we observe that the peaks in the distributions of y_0 in both are at $28\,\mathrm{kpc}$ approximately. The other similarity between the two fits is their distribution in central density, which also peak at roughly the same value in both. The forcing of q_ρ to stay fixed at 1 seems to be accommodated for by varying the values of β, γ, and r_0, so that a similar, albeit inexact, stream is reproduced. The best fit orbit found in this case is similar to the one in a double spheroidal halo, but they differ in their direction of motion, i.e., the estimated components of the velocity are similar in magnitude, but of opposite sign. This causes the leading and trailing arms to be the opposite of that in the previous fit, but since the distinction between the two arms in the data itself is not very clear, both these solutions can be taken to be effectively equivalent.

Fitting in a Logarithmic Halo

Following the example of Chapter 3, we fit the stream in an axisymmetric logarithmic halo as well. The contribution from the fixed baryonic components are also included in the calculation of the accelerations. All the parameters of the halo potential (the flattening, circular velocity and scale radius) were set to be free parameters. A com-
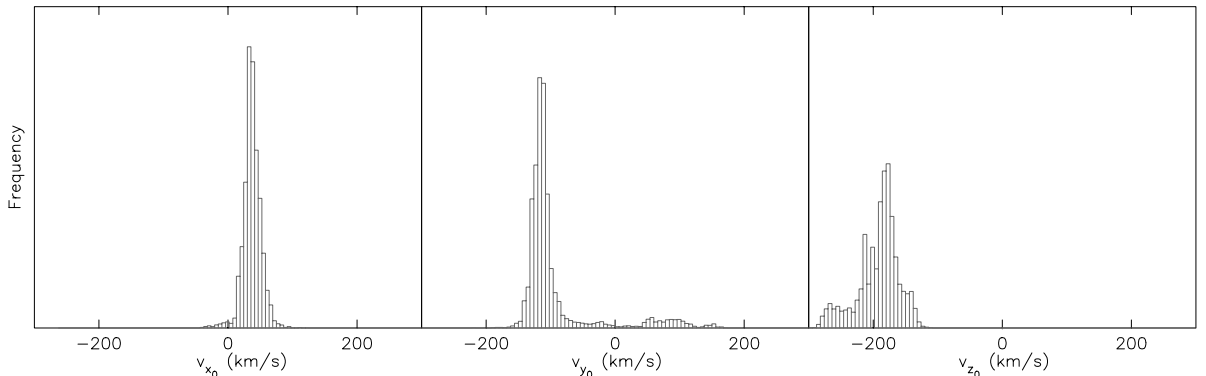
Figure 4.13: The MCMC distributions of the initial velocity components, obtained by fitting the stream in a spherical halo.

parison between the data and best fit orbit found is shown in Figure 4.14. The best fit orbit seems to be different from the previous two fitting, even though it reproduces many of the features of the stream. Figure 4.15 shows the rotational velocity curve of the best fit model. Figure 4.16 shows the distributions in q_ϕ, V_0 and R_c, and Figure 4.17 shows the distributions in the initial velocity components. Since the best fit orbit found is quite different from the one in the spheroidal and spherical fits, it is not surprising that the peak of the distribution in q_ϕ does not coincide with that of q_ρ in the earlier fits. However, the fitting routine did find orbits that are similar to the earlier fits, an example of which is shown in Figure 4.18. These have q_ϕ values that are comparable with the q_ρ estimates (using the relation $1 - q_\phi \approx \frac{1}{3}[1 - q_\rho]$). The goodness of the fit for two very distinct orbits, with vastly different values of flattening suggests that a much more thorough exploration of these parameters is required before being able to reach a conclusive understanding of the stream and halo of NGC 5907.

Fitting in MOND

As mentioned in Chapter 1, probes of dark matter are useful in testing modified Newtonian dynamics (MOND). Therefore, we attempted to fit the stream in a MOND potential derived from the baryonic components. For this purpose, the accelerations
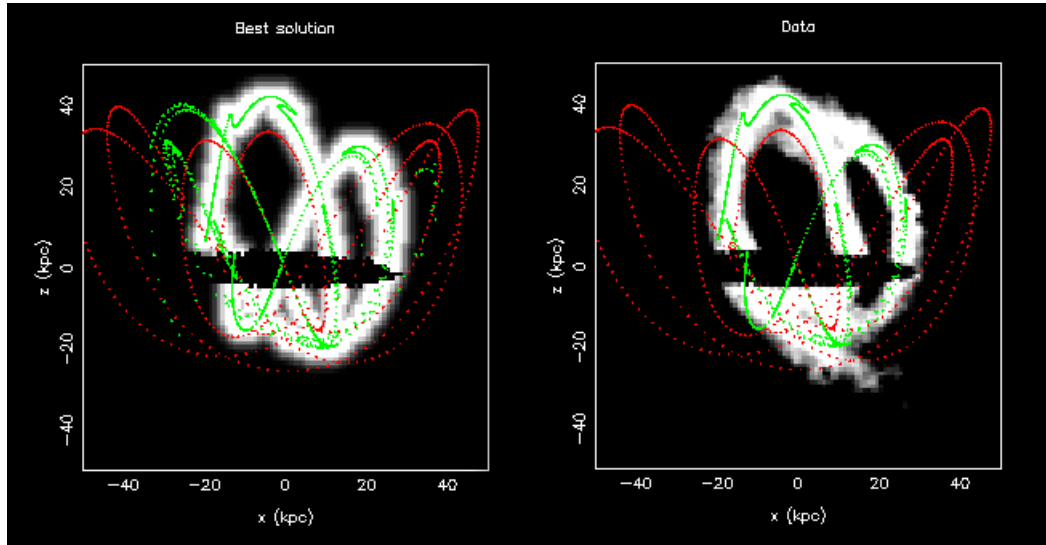
Figure 4.14: A comparison of the best fitting stream (left) and the data (right) in an axisymmetric logarithmic halo. In the left panel, the red curve shows the backward integrated orbit of the progenitor, from which the green curves that represent the corresponding stellar stream can be derived with the correction mechanism described in Chapter 3. The green curves are smeared out to obtain an expected image (in white) of the trial stream. The red and green curves in the right panel are the same as in the left, and have been overlaid on the observed stream image for comparison.
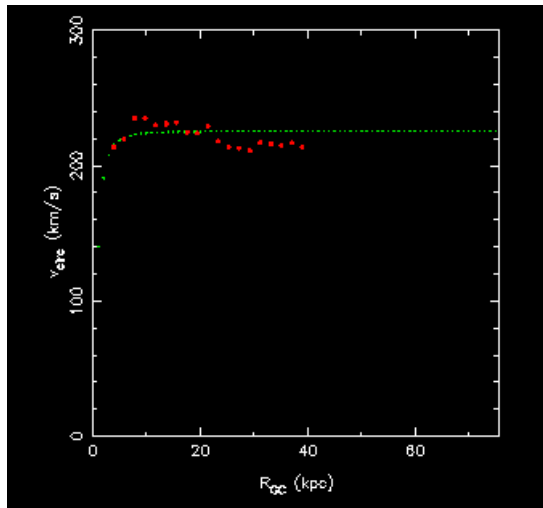
Figure 4.15: The rotational velocity curve of the best fit logarithmic model. The observed HI rotational velocity data of Sancisi and van Albada (1987) is marked in red, and the rotational curve of the model in green.
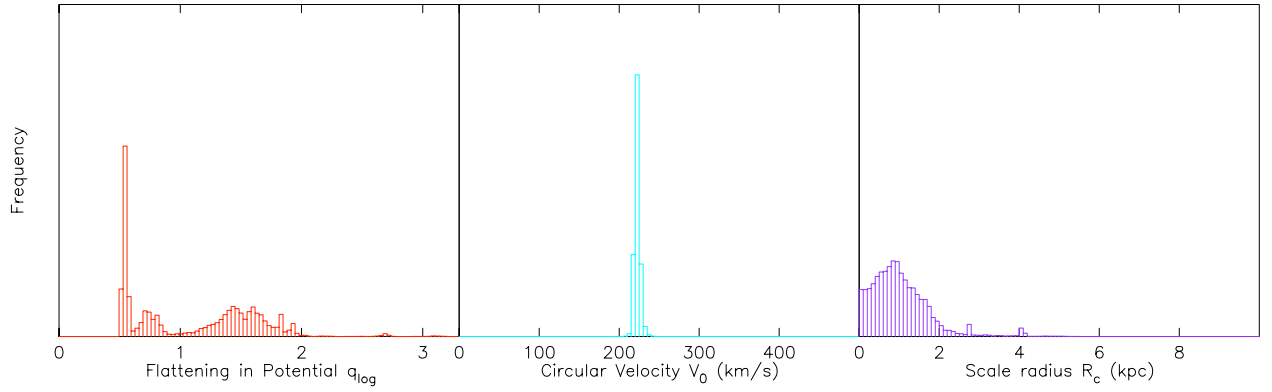
Figure 4.16: The MCMC distributions of the fitted parameters. From left to right: the flattening in logarithmic potential q_ϕ, the circular velocity V_0, and the scale radius R_c, obtained by fitting the stream in a logarithmic potential.
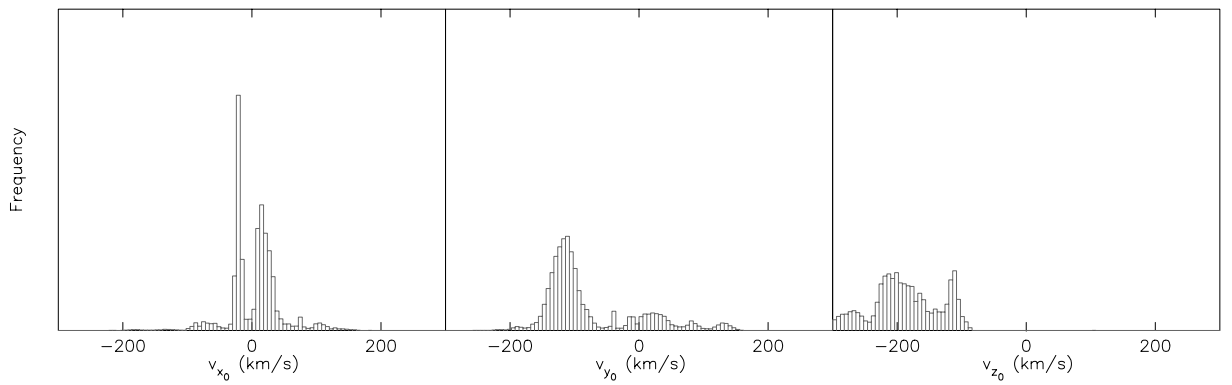
Figure 4.17: The MCMC distributions of the initial velocity components in an axymmetric logarithmic potential.
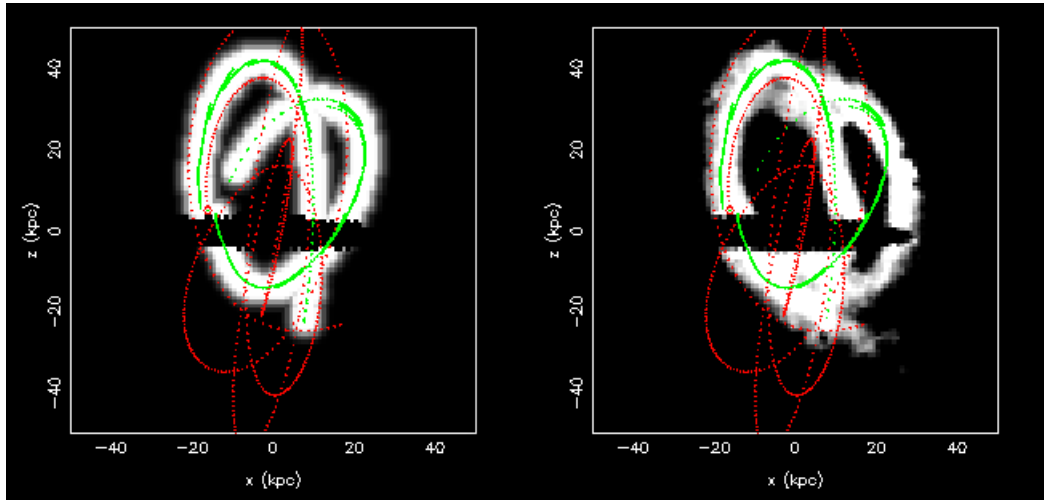
Figure 4.18: A trial stream in an axisymmetric logarithmic halo that is similar to the best-fit streams in the double spheroidal and spherical cases.

were calculated by first converting the MOND potential into an equivalent phantom dark matter halo model. This enables us to easily use the multipole expansion, as in the previous cases of the double spheroidal halo, for calculating the accelerations and integrate the orbits. In order to derive the phantom dark matter in our case, we first generate a MOND potential by solving the modified Poissonian equation, which can be approximated as:

$$\nabla \cdot (||\nabla\Phi||\nabla\Phi) = 4\pi G a_0 \rho \tag{4.1}$$

in the deep MOND regime. Once the MONDian potential is obtained, we consider it as a Newtonian potential such that

$$\nabla\Phi = 4\pi\rho_{eff} \tag{4.2}$$

where $\nabla\Phi = \vec{g}_{mond}$ is calculated from the modified Poissonian solver (see Ciotti et al. 2006; Nipoti et al. 2007; Wu et al. 2008) and ρ_{eff} is the effective equivalent density in the Newtonian framework. Subtracting the (Newtonian) contributions from the baryonic components, we obtain the phantom dark matter halo, which can then be used as a fixed component in the multicomponent model. Trial streams are generated
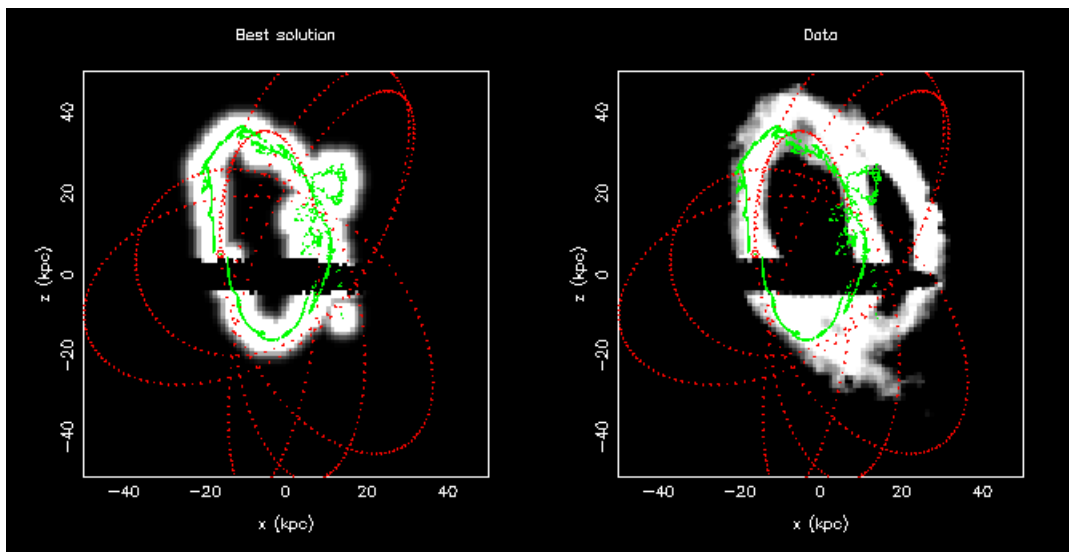
Figure 4.19: A comparison of the best fitting stream (left) and the data (right) in a MOND framework. In the left panel, the red curve shows the backward integrated orbit of the progenitor, from which the green curves that represent the corresponding stellar stream can be derived with the correction mechanism described in Chapter 3. The green curves are smeared out to obtain an expected image (in white) of the trial stream. The red and green curves in the right panel are the same as in the left, and have been overlaid on the observed stream image for comparison.

in this fixed potential with varying orbital parameters (velocity and initial radial distance) to find the best fit trial stream. The best fit we have found so far is relatively poor, as can be seen in Figure 4.19, even though the outer part of the rotational curve was reasonably well reproduced in this fixed potential (Figure 4.20). Figure 4.21 shows the distributions in the velocity components. As before, a more detailed study is required before any strong conclusions may be drawn.

4.4   Discussion

In this Chapter, we presented the preliminary tests obtained by using an improved fitting routine to fit the exquisite stream observed around NGC 5907. We illustrated a few initial fits in galactic models with axisymmetric halos, as well as a fit in a MOND framework. Martínez-Delgado et al. (2008) showed that it possible to reproduce a
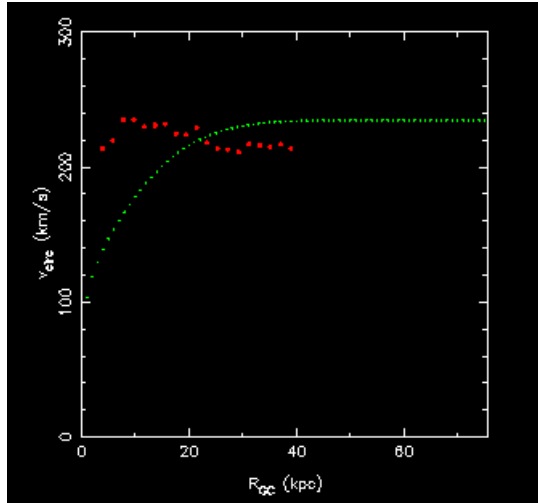
Figure 4.20: The rotational velocity curve produced in a MOND scenario. The observed HI rotational velocity data of Sancisi and van Albada (1987) is marked in red, and the rotational curve of the model in green.
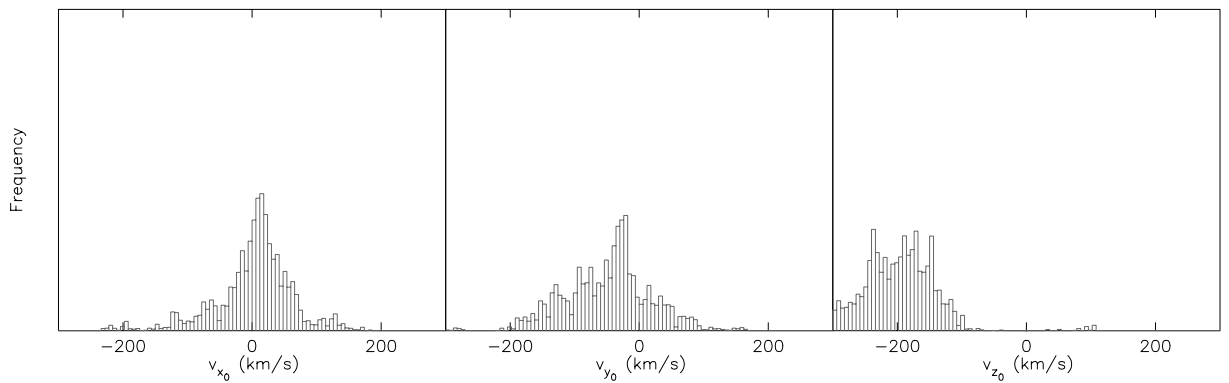
Figure 4.21: The MCMC distributions of the initial velocity components in a MOND framework.

stream similar to the observed one in a spherical halo, by obtaining N-body simulations that resembled the stream. To test the robustness of this result, we used our approach to fit the stream in a spherical halo, and found that it yields a remarkably similar best fit stream. However, a much better fit to the observed stream is obtained when the flattening parameter is set to be free, which indicates that the halo may be quite prolate. It is important to further test this possibility, as fits in a logarithmic halo show that a vastly different orbit could also produce similar structures. The ambiguity in the exact path of the stream makes it difficult to resolve this problem. Another aspect that stands out in these preliminary tests is that none of the fits were able to produce the south-western tail of the stream. In earlier fits of the NGC 5907 stream, based on Parallel Tempering rather than affine-invariant sampling with likelihood calculated as the distance of the trial stream from the observed stream instead of a pixel-to-pixel comparison, we found that a mildly triaxial logarithmic halo could produce the south western feature, along with the other parts of the stream. Due to time-constraints, this possibility could not be explored further with the modified fitting routine, and remains an urgent follow-up of the work presented in this chapter. We also find that the stream could not be fit well in a MOND framework, but this may be due to inaccuracies in the baryonic model or insufficient sampling. Nonetheless, further exploration of the stream in a MOND framework using the phantom dark matter approach could provide strong constraints on this popular alternate theory of gravity.

Chapter 5

Conclusions and Outlook

Stellar streams that form during the minor mergers of galaxies are fast becoming critical tools to study the morphology of galactic halos, which in turn can reveal the nature of dark matter and the process of galaxy formation. In this thesis, we introduced a novel approach to using stellar streams as probes of galactic halos. The usual approach in implementing these streams as potential tracers depends either on the flawed assumption that they follow exact orbits in the potential, or by the reproduction of the observed stream using N-body simulations that are too computationally expensive to enable a thorough parameter search. The method described in this thesis improves over both these techniques by combining their positive attributes. A correction mechanism was developed which can easily accurately compute a representative stream from a given orbit of the satellite, provided its mass is less than $\sim 1.0 \times 10^9$, so that a large number of N-body simulations (of the order of millions) can be avoided. An extensive search of the halo parameter space can then be carried out using MCMC sampling methods such as parallel tempering or affine invariant ensemble sampling.

With the methodology in place, we demonstrated that the parameters of the stream and of the mass distribution of the host galaxy can be constrained, depending on the type and quantity of the data available. We were especially interested in investigating whether the density profiles of galactic halos (or at least their flattening) can be constrained using only the projection of the stellar stream on the sky, which is the typical information available for external galaxies. Luckily, we find by testing the

method on pseudo streams that it is indeed possible to measure the halo flattening, if the streams have at least two turning points.

Encouraged by these results, we proceeded to apply the technique on the exquisite stream of NGC 5907, which is a near-perfect candidate for the method with its looping structures and several turning points. Unfortunately, the same looping structures create some confusion as to its exact path around the galaxy, while the absence of the progenitor causes some further ambiguity in the stream modelling. Nonetheless, we were able to obtain some preliminary fits for the stream and initial estimates of the various parameters, which indicate that the halo may be prolate. A rigorous study of the stream is still needs to be undertaken to draw strong conclusions from this system. In what follows, some of the assumptions and limitations of the technique are discussed, as well as future prospects based on the method.

A follow up work that could be immediately undertaken using the methodology in its current form is its application to several low mass, lengthy streams observed in our Galaxy such as well as external galaxies. The method may be readily applied to the Sagittarius stream, the streams of M31, M63 and several other more distant systems (see Martínez-Delgado et al. 2010 for a pilot survey). With increasingly sensitive instruments and large-scale surveys, we would be able to constrain the halo shapes and profiles of a statistically significant number of galaxies and get a sense of the distribution of halo shapes and profiles of real galaxies, which can then be compared with numerical predictions of the same. Advances in technology also promise measurements of proper motions of stars in external galaxies, which would enable much better constraints of their potentials, even with shorter streams. Future missions similar to the (unfortunately now cancelled) Space Interferometry Mission (SIM) may make this possibility a reality.

Besides observational improvements, refinements in the theoretical aspects of the technique would also greatly enhance such studies based on stellar streams. First and foremost, the work presented in this thesis can easily be extended to perform a similar analysis using triaxial halo models or non-parametric halo models, in addition to the axisymmetric models that we have used. Some efforts were made in this direction,

but could not be concluded due to time constraints. We have also made other implicit assumptions in our work, for the sake of simplicity, whose effects remain to be examined. For instance, the method rests on the assumption that stars of the in-falling satellite galaxy follow the dark matter particles which get tidally stripped. Although this is a reasonable assumption, especially for low mass halos, it is worth examining multi-component satellite galaxy models that include stars and dark matter. We have also assumed in all our testing that the halos are static over the time period of the evolution of the stellar streams. In a live halo, the expectation is that the geometry of the streams formed in it would be affected, which could have a significant impact on the estimated halo shape. A similar factor to be considered in future studies is the alignment of the dark matter halo and the stellar disk.

Another important question to be addressed regards the identification of streams formed due to multiple accretion events. The double-elliptical structure of the NGC 5907 stream, for example, may be a result of two separate accretion events. The near-constant width of the stellar structure along its path indicates that it is probably the remnant of a single accretion, but it would be helpful to develop methods that strongly distinguish between structures of different accretions.

It would be worthwhile to build on the current technique and generalize it to more massive satellites. This can be done by including dynamical friction in the correction mechanism put forward in this thesis. Since analytical expressions for the orbital decay of massive satellites are available, they may be used in the backward and forward orbit integrations of the progenitor and stars that escape the satellite. This would effectively provide a correction mechanism for massive satellites, which can then be used to perform similar statistical analyses of massive streams.

An interesting theoretical study may be the comparison, and possible combination, of the approach presented in this thesis and that described in Eyre and Binney (2009a,b), wherein action-angle variables are used to study streams and their host halos.

The technique of fitting streams can also be effectively used to fit several streams in a given potential, which would introduce more orbital parameters, but since these

are usually well-constrained, it would not increase the computational cost by much or introduce degeneracies in the estimated distributions of the derived parameters. This opens up a world of possibilities of using not just the long structures, but also small tidal features such as arcs, shells, and short streams, as probes of galactic halos.

Bibliography

Aguilar, L. A. and White, S. D. M. (1985). Tidal interactions between spherical galaxies. *Astrophysical Journal*, 295:374.

Allgood, B., Flores, R. A., Primack, J. R., Kravtsov, A. V., Wechsler, R. H., Faltenbacher, A., and Bullock, J. S. (2006). The shape of dark matter haloes: dependence on mass, redshift, radius and formation. *MNRAS*, 367:1781.

Angus, G. W., Famaey, B., and Zhao, H. S. (2006). Can mond take a bullet? analytical comparisons of three versions of mond beyond spherical symmetry. *Monthly Notices of the Royal Astronomical Society*, 371:138.

Babcock, H. W. (1939). The rotation of the andromeda nebula. *Lick Observatory bulletin ; no. 498; Lick Observatory bulletins ; no. 498.*, 19:41.

Bahcall, J. N. and Sarazin, C. L. (1977). Parameters and predictions for the x-ray emitting gas of coma, perseus, and virgo. *Astrophysical Journal*, 213:L99. A&AA ID. AAA019.161.003.

Bailin, J. and Steinmetz, M. (2005). Internal and external alignment of the shapes and angular momenta of Œõcdm halos. *ApJ*, 627:647.

Barnes, J. and Efstathiou, G. (1987). Angular momentum from tidal torques. *Astrophysical Journal*, 319:575.

Barnes, J. and Hut, P. (1986). A hierarchical o(n log n) force-calculation algorithm. *Nature (ISSN 0028-0836)*, 324:446.

Becquerel, A. (1896). On the invisible rays emitted by phosphorescent bodies. *Comptes Rendus*, 122:501–503.

Bekenstein, J. D. (2004). Relativistic gravitation theory for the modified newtonian dynamics paradigm. *Physical Review D*, 70:83509.

Belokurov, V. et al. (2007). An orphan in the "field of streams". *ApJ*, 658:337.

Bergström, L. (2009). Dark matter candidates. *New Journal of Physics*, 11:5006.

Bernstein, G. M. and Jarvis, M. (2002). Shapes and shears, stars and smears: Optimal measurements for weak lensing. *The Astronomical Journal*, 123:583.

Bett, P., Eke, V., Frenk, C. S., Jenkins, A., Helly, J., and Navarro, J. (2007). The spin and shape of dark matter haloes in the millennium simulation of a Œõ cold dark matter universe. *MNRAS*, 376:215.

Binney, J. and Tremaine, S. (2008). Galactic dynamics: Second edition. *Galactic Dynamics: Second Edition.*

Bosma, A. (1978). The distribution and kinematics of neutral hydrogen in spiral galaxies of various morphological types. *PhD Thesis*, page 195.

Bullock, J. S. (2002). Shapes of dark matter halos. *The Shapes of Galaxies and their Dark Halos. Proceedings of the Yale Cosmology Workshop. Held 28-30 May 2001 in New Haven*, page 109.

Buote, D. A. and Canizares, C. R. (1997). The nature of the x-ray emission and the mass distributions in two early-type galaxies. *Astrophysical Journal v.474*, 474:650.

Buote, D. A. and Canizares, C. R. (1998a). The shapes and sizes of elliptical galaxy halos from x-ray observations. *Galactic Halos: A UC Santa Cruz Workshop*, 136:289.

Buote, D. A. and Canizares, C. R. (1998b). X-ray isophote shapes and the mass of ngc 3923. *Monthly Notices of the Royal Astronomical Society*, 298:811.

Buote, D. A., Jeltema, T. E., Canizares, C. R., and Garmire, G. P. (2002). Chandra evidence of a flattened, triaxial dark matter halo in the elliptical galaxy ngc 720. *The Astrophysical Journal*, 577:183.

Carlberg, R. G. et al. (2011). Density variations in the nw star stream of m31. *ApJ*, 731:124.

Casertano, S. (1983). Rotation curve of the edge-on spiral galaxy ngc 5907: disc and halo masses. *Royal Astronomical Society*, 203:735.

Chandrasekhar, S. (1943). Dynamical friction. i. general considerations: the coefficient of dynamical friction. *Astrophysical Journal*, 97:255.

Ciotti, L., Londrillo, P., and Nipoti, C. (2006). Axisymmetric and triaxial mond density-potential pairs. *The Astrophysical Journal*, 640:741.

Clowe, D., Bradač, M., Gonzalez, A. H., Markevitch, M., Randall, S. W., Jones, C., and Zaritsky, D. (2006). A direct empirical proof of the existence of dark matter. *The Astrophysical Journal*, 648:L109.

Clowe, D., Gonzalez, A., and Markevitch, M. (2004). Weak-lensing mass reconstruction of the interacting cluster 1e 0657-558: Direct evidence for the existence of dark matter. *The Astrophysical Journal*, 604:596.

Combes, F. (2006). Polar ring galaxies and warps. *EAS Publications Series*, 20:97. ISBN: 2868839177.

Conn, B. C. et al. (2007). The aat/wfi survey of the monoceros ring and canis major dwarf galaxy - i. from l = (193-276)°. *MNRAS*, 376:939.

Conn, B. C., Lane, R. R., Lewis, G. F., Irwin, M. J., Ibata, R. A., Martin, N. F., Bellazzini, M., and Tuntsov, A. V. (2008). The anglo-australian telescope/wide field imager survey of the monoceros ring and canis major dwarf galaxy - ii. from l = (280-025)°. *MNRAS*, 390:1388.

Conn, B. C., Lewis, G. F., Irwin, M. J., Ibata, R. A., Ferguson, A. M. N., Tanvir, N., and Irwin, J. M. (2005). The isaac newton telescope wide field camera survey of the monoceros ring: accretion origin or galactic anomaly? *MNRAS*, 362:475.

Cowan, C. L., Reines, F., Harrison, F. B., Anderson, E. C., and Hayes, F. N. (1953). Large liquid scintillation detectors. *Physical Review*, 90:493.

de Blok, W. J. G. (2010). The core-cusp problem. *Advances in Astronomy*, 2010:5.

Debattista, V. P., Moore, B., Quinn, T., Kazantzidis, S., Maas, R., Mayer, L., Read, J., and Stadel, J. (2008). The causes of halo shape changes induced by cooling baryons: Disks versus substructures. *ApJ*, 681:1076.

Dehnen, W. (2000). A very fast and momentum-conserving tree code. *ApJ*, 536:L39.

Dehnen, W. (2001). Towards optimal softening in three-dimensional n-body codes - i. minimizing the force error. *Monthly Notices of the Royal Astronomical Society*, 324:273.

Dehnen, W. (2002). A hierarchical ¡e10¿o¡/e10¿(n) force calculation algorithm. *Journal of Computational Physics*, 179:27.

Dehnen, W. and Binney, J. (1998). Mass models of the milky way. *MNRAS*, 294:429.

Dubinski, J. (1994). The effect of dissipation on the shapes of dark halos. *ApJ*, 431:617.

Dubinski, J. and Carlberg, R. G. (1991). The structure of cold dark matter halos. *ApJ*, 378:496.

Dubinski, J., Mihos, J. C., and Hernquist, L. (1996). Using tidal tails to probe dark matter halos. *Astrophysical Journal v.462*, 462:576.

Dubinski, J., Mihos, J. C., and Hernquist, L. (1999). Constraining dark halo potentials with tidal tails. *ApJ*, 526:607.

Eggen, O. J., Lynden-Bell, D., and Sandage, A. R. (1962). Evidence from the motions of old stars that the galaxy collapsed. *Astrophysical Journal*, 136:748.

Ellis, J., Hagelin, J. S., Nanopoulos, D. V., Olive, K., and Srednicki, M. (1984). Supersymmetric relics from the big bang. *Nuclear Physics B*, 238:453.

Eyre, A. and Binney, J. (2009a). Fitting orbits to tidal streams with proper motions. *MNRAS*, 399:L160.

Eyre, A. and Binney, J. (2009b). Locating the orbits delineated by tidal streams. *MNRAS*, 400:548.

Famaey, B., Angus, G. W., Gentile, G., Shan, H. Y., and Zhao, H. S. (2008). The wedding of modified dynamics and non-exotic dark matter in galaxy clusters. *DARK MATTER IN ASTROPARTICLE AND PARTICLE PHYSICS. Proceedings of the 6th International Heidelberg Conference. Held 24-28 September 2007 in University of Sydney*, page 393.

Feng, J. L. (2004). Dark matter detection in space. *Nuclear Physics B Proceedings Supplements*, 134:95.

Feng, J. L. (2010). Non-wimp candidates. *Particle Dark Matter : Observations*, page 190.

Feng, J. L., Rajaraman, A., and Takayama, F. (2003a). Graviton cosmology in universal extra dimensions. *Physical Review D*, 68:85018.

Feng, J. L., Rajaraman, A., and Takayama, F. (2003b). Superweakly interacting massive particle dark matter signals from the early universe. *Physical Review D*, 68:63504.

Feng, J. L., Rajaraman, A., and Takayama, F. (2003c). Superweakly interacting massive particles. *Physical Review Letters*, 91:11302.

Forman, W. and Jones, C. (1982). X-ray-imaging observations of clusters of galaxies. *In: Annual review of astronomy and astrophysics. Volume 20. (A83-12176 02-90) Palo Alto*, 20:547. A&AA ID. AAA032.160.043.

Freeman, K. and Bland-Hawthorn, J. (2002). The new galaxy: Signatures of its formation. *Annual Review of Astronomy and Astrophysics*, 40:487.

Frenk, C. S., White, S. D. M., Davis, M., and Efstathiou, G. (1988). The formation of dark halos in a universe dominated by cold dark matter. *ApJ*, 327:507.

Fukushige, T. and Heggie, D. C. (2000). The time-scale of escape from star clusters. *Monthly Notices of the Royal Astronomical Society*, 318:753.

Glashow, S. (1961). Partial-symmetries of weak interactions. *Nuclear Physics*, 22:579.

Goodman, J. and Weare, J. (2009). Ensemble samplers with affine invariance. *cims.nyu.edu*.

Gregory, P. C. (2005). Bayesian logical data analysis for the physical sciences: A comparative approach with 'mathematica' support. *Bayesian Logical Data Analysis for the Physical Sciences: A Comparative Approach with 'Mathematica' Support. Edited by P. C. Gregory. ISBN 0 521 84150 X (hardback); QA279.5.G74 2005 519.5'42 – dc22; 200445930. Published by Cambridge University Press*. ISBN: 0-521-84150-X.

Grillmair, C. J. (2006). Detection of a $60\,°$-long dwarf galaxy debris stream. *ApJ*, 645:L37.

Grillmair, C. J. and Dionatos, O. (2006). Detection of a $63\,°$ cold stellar stream in the sloan digital sky survey. *ApJ*, 643:L17.

Helmi, A. (2004). Is the dark halo of our galaxy spherical? *MNRAS*, 351:643.

Hertzberg, M. P., Tegmark, M., and Wilczek, F. (2008). Axion cosmology and the energy scale of inflation. *Physical Review D*, 78:83507.

Hoekstra, H., Yee, H. K. C., and Gladders, M. D. (2004). Properties of galaxy dark matter halos from weak lensing. *ApJ*, 606:67.

Humphrey, P. J. and Buote, D. A. (2010). The slope of the mass profile and the tilt of the fundamental plane in early-type galaxies. *Monthly Notices of the Royal Astronomical Society*, 403:2143.

Humphrey, P. J., Buote, D. A., Gastaldello, F., Zappacosta, L., Bullock, J. S., Brighenti, F., and Mathews, W. G. (2006). A chandra view of dark matter in early-type galaxies. *The Astrophysical Journal*, 646:899.

Ibata, R., Chapman, S., Ferguson, A. M. N., Irwin, M., Lewis, G., and McConnachie, A. (2004). Taking measure of the andromeda halo: a kinematic analysis of the giant stream surrounding m31. *MNRAS*, 351:117.

Ibata, R., Irwin, M., Lewis, G., Ferguson, A. M. N., and Tanvir, N. (2001a). A giant stream of metal-rich stars in the halo of the galaxy m31. *Nat*, 412:49.

Ibata, R., Lewis, G. F., Irwin, M., Totten, E., and Quinn, T. (2001b). Great circle tidal streams: Evidence for a nearly spherical massive dark halo around the milky way. *ApJ*, 551:294.

Iodice, E., Arnaboldi, M., Bournaud, F., Combes, F., Sparke, L. S., van Driel, W., and Capaccioli, M. (2003). Polar ring galaxies and the tully-fisher relation: Implications for the dark halo shape. *ApJ*, 585:730.

James, P. A. and Casali, M. M. (1998). Confirmation of a faint red halo around ngc 5907. *Monthly Notices of the Royal Astronomical Society*, 301:280.

Jeans, J. H. (1922). The motions of stars in a kapteyn universe. *Monthly Notices of the Royal Astronomical Society*, 82:122.

Jing, Y. P. and Suto, Y. (2002). Triaxial modeling of halo density profiles with high-resolution n-body simulations. *ApJ*, 574:538.

Johnston, K. V., Hernquist, L., and Bolte, M. (1996). Fossil signatures of ancient accretion events in the halo. *Astrophysical Journal v.465*, 465:278.

Johnston, K. V., Sackett, P. D., and Bullock, J. S. (2001). Interpreting debris from satellite disruption in external galaxies. *The Astrophysical Journal*, 557:137.

Johnston, K. V., Sigurdsson, S., and Hernquist, L. (1999). Measuring mass-loss rates from galactic satellites. *Monthly Notices of the Royal Astronomical Society*, 302:771.

Just, A., Möllenhoff, C., and Borch, A. (2006). An evolutionary disc model of the edge-on galaxy ngc 5907. *Astronomy and Astrophysics*, 459:703.

Kahn, F. D. and Woltjer, L. (1959). Intergalactic matter and the galaxy. *Astrophysical Journal*, 130:705.

Kapteyn, J. C. (1922). First attempt at a theory of the arrangement and motion of the sidereal system. *Astrophysical Journal*, 55:302.

Kazantzidis, S., Abadi, M. G., and Navarro, J. F. (2010). The sphericalization of dark matter halos by galaxy disks. *ApJ*, 720:L62.

Koposov, S. E., Rix, H.-W., and Hogg, D. W. (2010). Constraining the milky way potential with a six-dimensional phase-space map of the gd-1 stellar stream. *ApJ*, 712:260.

Kuijken, K. and Gilmore, G. (1989). The mass distribution in the galactic disc - ii - determination of the surface mass density of the galactic disc near the sun. *MNRAS*, 239:605.

Law, D. R. and Majewski, S. R. (2010). The sagittarius dwarf galaxy: A model for evolution in a triaxial milky way halo. *ApJ*, 714:229.

Law, D. R., Majewski, S. R., and Johnston, K. V. (2009). Evidence for a triaxial milky way dark matter halo from the sagittarius stellar tidal stream. *ApJ*, 703:L67.

Lequeux, J., Fort, B., Dantel-Fort, M., Cuillandre, J.-C., and Mellier, Y. (1996). V- and i-band observations of the halo of ngc 5907. *Astronomy and Astrophysics*, 312:L1.

Lux, H. (2010). The dynamics of galactic satellites: links to galaxy formation. *Thesis (PHD). University of Zurich.*

Mackey, A. D. et al. (2010). Evidence for an accretion origin for the outer halo globular cluster system of m31. *ApJ*, 717:L11.

Majewski, S. R., Skrutskie, M. F., Weinberg, M. D., and Ostheimer, J. C. (2003). A two micron all sky survey view of the sagittarius dwarf galaxy. i. morphology of the sagittarius core and tidal arms. *ApJ*, 599:1082.

Mandelbaum, R., Hirata, C. M., Broderick, T., Seljak, U., and Brinkmann, J. (2006). Ellipticity of dark matter haloes with galaxy-galaxy weak lensing. *MNRAS*, 370:1008.

Martínez-Delgado, D., Gabany, R. J., Crawford, K., Zibetti, S., Majewski, S. R., Rix, H.-W., Fliri, J., Carballo-Bello, J. A., Bardalez-Gagliuffi, D. C., Peñarrubia, J., Chonis, T. S., Madore, B., Trujillo, I., Schirmer, M., and McDavid, D. A. (2010). Stellar tidal streams in spiral galaxies of the local volume: A pilot survey with modest aperture telescopes. *AJ*, 140:962.

Martínez-Delgado, D., Gómez-Flechoso, M. A., and Aparicio, A. (2002). Tracing out the northern stream of the sagittarius dwarf galaxy with color-magnitude diagram techniques. *Observed HR Diagrams and Stellar Evolution*, 274:468. ISBN: 1-58381-116-8.

Martínez-Delgado, D., Peñarrubia, J., Gabany, R. J., Trujillo, I., Majewski, S. R., and Pohlen, M. (2008). The ghost of a dwarf galaxy: Fossils of the hierarchical formation of the nearby spiral galaxy ngc 5907. *ApJ*, 689:184.

Mayer, L., Moore, B., Quinn, T., Governato, F., and Stadel, J. (2002). Tidal debris of dwarf spheroidals as a probe of structure formation models. *MNRAS*, 336:119.

McConnachie, A. W., Irwin, M. J., Ferguson, A. M. N., Ibata, R. A., Lewis, G. F., and Tanvir, N. (2004). Determining the location of the tip of the red giant branch in old stellar populations: M33, andromeda i and ii. *MNRAS*, 350:243.

Merrifield, M. R. (2004). The galactic halo and cdm. *International Astronomical Union Symposium no. 220*, 220:431.

Milgrom, M. (1983a). A modification of the newtonian dynamics - implications for galaxies. *Astrophysical Journal*, 270:371.

Milgrom, M. (1983b). A modification of the newtonian dynamics as a possible alternative to the hidden mass hypothesis. *Astrophysical Journal*, 270:365.

Morrison, H., Sackett, P., Harding, P., and Boroson, T. (1995). A faint luminous halo that may trace the dark matter around spiral galaxy ngc 5907. *Dark matter. AIP Conference Proceedings*, 336:157.

Mouhcine, M., Ibata, R., and Rejkuba, M. (2010). A panoramic view of the milky way analog ngc 891. *ApJ*, 714:L12.

Navarro, J. F., Frenk, C. S., and White, S. D. M. (1996). The structure of cold dark matter halos. *ApJ*, 462:563.

Newberg, H. J. et al. (2002). The ghost of sagittarius and lumps in the halo of the milky way. *ApJ*, 569:245.

Nipoti, C., Londrillo, P., Zhao, H., and Ciotti, L. (2007). Vertical dynamics of disc galaxies in modified newtonian dynamics. *Monthly Notices of the Royal Astronomical Society*, 379:597.

O'Brien, J. C., Freeman, K. C., and van der Kruit, P. C. (2010a). The dark matter halo shape of edge-on disk galaxies . iii. modelling the hi observations: results. *A&A*, 515:62.

O'Brien, J. C., Freeman, K. C., and van der Kruit, P. C. (2010b). The dark matter halo shape of edge-on disk galaxies. ii. modelling the hi observations: methods. *A&A*, 515:61.

O'Brien, J. C., Freeman, K. C., and van der Kruit, P. C. (2010c). The dark matter halo shape of edge-on disk galaxies. iv. ugc 7321. *A&A*, 515:63.

O'Brien, J. C., Freeman, K. C., van der Kruit, P. C., and Bosma, A. (2010d). The dark matter halo shape of edge-on disk galaxies . i. hi observations. *A&A*, 515:60.

Odenkirchen, M. et al. (2001). Detection of massive tidal tails around the globular cluster palomar 5 with sloan digital sky survey commissioning data. *ApJ*, 548:L165.

Odenkirchen, M. et al. (2003). The extended tails of palomar 5: A $10°$ arc of globular cluster tidal debris. *AJ*, 126:2385.

Olling, R. P. and Merrifield, M. R. (2000). Two measures of the shape of the dark halo of the milky way. *MNRAS*, 311:361.

Peng, C. Y., Ho, L. C., Impey, C. D., and Rix, H.-W. (2002). Detailed structural decomposition of galaxy images. *The Astronomical Journal*, 124:266.

Pfenniger, D., Combes, F., and Martinet, L. (1994). Is dark matter in spiral galaxies cold gas? i. observational constraints and dynamical clues about galaxy evolution. *A&A*, 285:79.

Press, W. H., Teukolsky, S. A., Vetterling, W. T., and Flannery, B. P. (1992). Numerical recipes in fortran. the art of scientific computing. *Cambridge: University Press*.

Read, J. I. and Moore, B. (2005). Tidal streams in a mond potential: constraints from sagittarius. *MNRAS*, 361:971.

Reines, F. and Cowan, C. L. (1953). Detection of the free neutrino. *Physical Review*, 92:830.

Reshetnikov, V. P. and Sotnikova, N. Y. (2000). The polar stellar ring and dark halo of ngc5907. *Astronomy Letters*, 26:277.

Roberts, M. S. and Whitehurst, R. N. (1975). The rotation curve and geometry of m31 at large galactocentric distances. *Astrophys. J.*, 201:327. A&AA ID. AAA014.158.127.

Rosati, P., Borgani, S., and Norman, C. (2002). The evolution of x-ray clusters of galaxies. *Annual Review of Astronomy and Astrophysics*, 40:539.

Ross, D. J., Mennim, A., and Heggie, D. C. (1997). Escape from a tidally limited star cluster. *Monthly Notices of the Royal Astronomical Society*, 284:811.

Rubbia, C. (1985). Experimental observation of the intermediate vector bosons wˆ{+}, wˆ{-}, and zˆ{0}. *Reviews of Modern Physics*, 57(3):699.

Rubin, V. C. and Ford, W. K. (1970). Rotation of the andromeda nebula from a spectroscopic survey of emission regions. *Astrophysical Journal*, 159:379. A&AA ID. AAA003.158.026.

Rubin, V. C., Ford, W. K. J., and Thonnard, N. . (1980). Rotational properties of 21 sc galaxies with a large range of luminosities and radii, from ngc 4605 /r = 4kpc/ to ugc 2885 /r = 122 kpc/. *Astrophysical Journal*, 238:471. A&AA ID. AAA027.158.318.

Rudy, R. J., Woodward, C. E., Hodge, T., Fairfield, S. W., and Harker, D. E. (1996). Infrared emission from the halo of ngc 5907. *American Astronomical Society*, 187:757.

Sackett, P. D. (1999). The shape of dark matter halos. *Galaxy Dynamics*, 182:393.

Sackett, P. D., Morrisoni, H. L., Harding, P., and Boroson, T. A. (1994a). A faint luminous halo that may trace the dark matter around spiral galaxy ngc5907. *Nat*, 370:441.

Sackett, P. D., Rix, H.-W., Jarvis, B. J., and Freeman, K. C. (1994b). The flattened dark halo of polar ring galaxy ngc 4650a: A conspiracy of shapes? *ApJ*, 436:629.

Salam, A. (1968). Elementary particle theory. *Ed. N. Svartholm, Stockholm,\ Almquist and Wiksell*, 367.

Sancisi, R. and van Albada, T. S. (1987). H i rotation curves of galaxies. *IN: Dark matter in the universe; Proceedings of the IAU Symposium*, 117:67.

Schramm, D. N. and Turner, M. S. (1998). Big-bang nucleosynthesis enters the precision era. *Reviews of Modern Physics*, 70:303.

Searle, L. and Zinn, R. (1978). Compositions of halo clusters and the formation of the galactic halo. *Astrophysical Journal*, 225:357. A&AA ID. AAA022.154.018.

Shang, Z., Zheng, Z., Brinks, E., Chen, J., Burstein, D., Su, H., Byun, Y.-I., Deng, L., Deng, Z., Fan, X., Jiang, Z., Li, Y., Lin, W., Ma, F., Sun, W.-H., Wills, B., Windhorst, R. A., Wu, H., Xia, X., Xu, W., Xue, S., Yan, H., Zhou, X., Zhu, J., and Zou, Z. (1998). Ring structure and warp of ngc 5907: Interaction with dwarf galaxies. *Astrophysical Journal Letters v.504*, 504:L23.

Smith, D. R., Bernstein, G. M., Fischer, P., and Jarvis, M. (2001). Weak-lensing determination of the mass in galaxy halos. *The Astrophysical Journal*, 551:643.

Smith, S. (1936). The mass of the virgo cluster. *Astrophysical Journal*, 83:23.

Sofue, Y. (1996). The most completely sampled rotation curves for galaxies. *Astrophysical Journal v.458*, 458:120.

Springel, V. and White, S. D. M. (1999). Tidal tails in cold dark matter cosmologies. *MNRAS*, 307:162.

Springel, V., White, S. D. M., and Hernquist, L. (2004). The shapes of simulated dark matter halos. *International Astronomical Union Symposium no. 220*, 220:421.

Steigman, G. (2010). Primordial nucleosynthesis: predicted and observed abundances. *Proceedings of the 11th Symposium on Nuclei in the Cosmos. 19-23 July 2010. Heidelberg*, page 1.

Szebehely, V. (1967). Theory of orbits. the restricted problem of three bodies. *New York: Academic Press.*

Teuben, P. (1995). The stellar dynamics toolbox nemo. *Astronomical Data Analysis Software and Systems IV*, 77:398.

Thonnard, N., Rubin, V. C., Ford, W. K., and Roberts, M. S. (1978). Radial velocities of spiral galaxies determined from 21-cm neutral hydrogen observations. *Astronomical Journal*, 83:1564. A&AA ID. AAA022.158.147.

Tully, R. B., Rizzi, L., Shaya, E. J., Courtois, H. M., Makarov, D. I., and Jacobs, B. A. (2009). The extragalactic distance database. *The Astronomical Journal*, 138:323.

van de Hulst, H. C., Raimond, E., and van Woerden, H. (1957). Rotation and density distribution of the andromeda nebula derived from observations of the 21-cm line. *Bulletin of the Astronomical Institutes of the Netherlands*, 14:1.

van der Meer, S. (1981). Stochastic cooling in the cern antiproton accumulator. *Proceedings of the 9th IEEE Particle Accelerator Conference. 11-13 Mar 1981*, 28:1994.

Varghese, A., Ibata, R., and Lewis, G. F. (2011). Stellar streams as probes of dark halo mass and morphology: a bayesian reconstruction. *Monthly Notices of the Royal Astronomical Society*, 417:198.

Warren, M. S., Zurek, W. H., Quinn, P. J., and Salmon, J. K. (1991). The shape of the invisible halo: N-body simulations on parallel supercomputers. *After the first three minutes. AIP Conference Proceedings*, 222:216.

Weinberg, S. (1967). A model of leptons. *Physical Review Letters*, 19:1264.

Weinberg, S. (1978). A new light boson? *Physical Review Letters*, 40:223.

White, M. (1999). Anisotropies in the cmb. *Proceedings of DPF99*.

White, S. and Rees, M. (1978). Core condensation in heavy halos-a two-stage theory for galaxy formation and clustering. *MNRAS*.

Wilczek, F. (1978). Problem of strong p and t invariance in the presence of instantons. *Physical Review Letters*, 40:279.

Wu, X., Famaey, B., Gentile, G., Perets, H., and Zhao, H. (2008). Milky way potentials in cold dark matter and modified newtonian dynamics. is the large magellanic cloud on a bound orbit? *Monthly Notices of the Royal Astronomical Society*, 386:2199.

Zwicky, F. (1933). Die rotverschiebung von extragalaktischen nebeln. *Helvetica Physica Acta*, 6:110.

Zwicky, F. (1937). On the masses of nebulae and of clusters of nebulae. *Astrophysical Journal*, 86:217.